UNIVERSITA' DEGLI STUDI DI MILANO-BICOCCA

Corso di Dottorato in Scienza dei Materiali
XXIII Ciclo

Development of advanced GaAs nanostructures by Droplet Epitaxy

Claudio Somaschini
Mat. 040828

Supervisor: Stefano Sanguinetti

do what you believe...

Index

Introduction

In the field of nanotechnology, a wide area of research is devoted to the studies about the self-assembly of semiconductor quantum nanostructures. Upon special conditions, semiconductor crystals spontaneously aggregate in nanometre sized clusters, which show unusual electronic and optical properties, thanks to their reduced dimension. Understanding the physical processes governing the formation of these structures has a major relevance in view of their application.

In this picture III-V semiconductor nanostructures have been intensively investigated because of their excellent optical quality, that allowed their use in optoelectronics. Amongst the various methods for the fabrication of nanostructures, the molecular beam epitaxy (MBE) growth is certainly one of the most important. Materials with superior quality can be grown with this technique, which also represents the best environment for the fundamental studies of surface science, due to the relative simplicity of the deposition.

Our work has been dedicated to the study of the fabrication of GaAs nanostructures by the Droplet Epitaxy (DE) technique. This MBE method constitutes an alternative path for the formation of III-V nanocrystals with excellent optical properties. Indeed in contrast with the standard layer-plus-islands growth mode, this technique is based on the spontaneous formation of nanometric droplets at the substrate surface. Although this method was firstly proposed by Koguchi twenty years ago, many aspects regarding the DE fabrication remained undisclosed. In order to clarify some of these open questions, we investigated the atomic processes occurring during the formation of GaAs nanostructures by DE, being the GaAs/AlGaAs the most studied system accessible through this technique. In particular the two main steps of the growth method, the nucleation of Ga droplets and the arsenic induced transformation of droplets into GaAs crystals, have been studied, combining the MBE growth with *in-situ* and *ex-situ*

characterization techniques. The gained knowledge permitted the full control over the size and shape of the GaAs nanostructures, which are of the greatest importance for a quantum system. Moreover the fabrication of original quantum nanostructures with complex and designable shapes was possible, by governing the physical processes occurring on the nanoscale, based on a pure bottom-up approach.

This Thesis is organized as follows: Chapter 1 contains an introduction on MBE, crystal growth and GaAs material; in Chapter 2 we reviewed the main developments of DE from the original proposal to the latest results; Chapter 3 reports the experimental equipments that have been used in our work; in Chapter 4 we described the results on the formation of Ga droplets on GaAs (001) surfaces; Chapter 5 is devoted to the analysis of the processes occurring during the creation of GaAs nanocrystals and in Chapter 6 we presented the fabrication of the original structures and some of their main optical and electronic properties.

Chapter 1

"if I could find you now things would get better
we could leave this town and run forever
I know somewhere, somehow we'll be together
let your waves crash down on me and take me away"

(from "Ocean Avenue" by Yellowcard)

Fundamentals of MBE and GaAs

In this chapter we will introduce the basics of the Molecular Beam Epitaxy (MBE) technique and some of the key concepts in crystal growth. The fundamental atomic processes involved in MBE and in thin films growth will be firstly discussed. Then we will describe the main aspects which determine the morphology of the deposited material and the most important growth modes. Later on we will focus on the system that was studied in this work, GaAs/AlGaAs, presenting its structural and electronic properties. Finally we will give a detailed analysis of GaAs (001) surface reconstructions, since this aspect played a very important role in our research.

1.1 Basics of MBE growth

MBE is a versatile technique for growing thin epitaxial structures made of semiconductors, metals or insulators. In this technique, thin films crystallize via reactions between molecular or atomic beams of the constituent elements and a substrate surface, which is maintained at an elevated temperature in ultrahigh vacuum (UHV). The composition of the grown epilayer and its dopants, which in turn depend on the evaporation rates of the appropriate sources, can be finely controlled. The growth rate of typically 1 μm/h (1 ML/s) is low enough that surface migration of the impinging species on the growing surface is ensured. Consequently the surface of the grown film can be atomically smooth. Simple mechanical shutters in front of the beam sources are used to start and stop the beam fluxes, so that changes in composition and doping can be abrupt on the atomic scale. What distinguishes MBE from previous vacuum deposition techniques is indeed its very precise control of the beam fluxes and growth conditions. Moreover, taking place in an UHV environment, the MBE growth can be followed *in-situ* by surface diagnostic methods, enabling the real-time observation of the phenomena occurring during growth. This led to a deep understanding of the crystal growth during MBE, allowing the fabrication of sophisticated device structures, using this technique.

The vacuum conditions for MBE are therefore very important to achieve the level of purity required by the modern semiconductor science and technology[1]. Two parameters, closely related to pressure, are important for the characterization of the vacuum: the mean free path and the concentration (number of molecules per unit volume) of the gas molecules. The mean free path is defined as the average distance traversed by the molecules between successive collisions. In standard MBE growth chambers the molecular beams, generated in effusion cells, cover a distance approximately equal to 20 cm between the gas sources and the substrate surface. During this path the beam

molecules may encounter residual gas species if the pressure in the chamber is not low enough, thus scattering processes may take place, degrading the beam nature. Thus the mean free path of the gas molecules coming from the cells must be larger then the distance between the sources and the substrate, to avoid undesirable scattering events. Although this first condition is fulfilled also in high vacuum environment, MBE needs UHV chambers to ensure the purity of the materials. Indeed a second condition requires the time for the formation of one monolayer by the molecular beam flux to be 10^5 times faster than the time for the formation of one monolayer caused by the adsorption of the residual gas molecules. For typical values of MBE growth rates (one second for the growth of one monolayer), we obtain that the deposition rate, caused by the residual gas pressure has to be about one monolayer in 28 hours. By considering the impinging rate J_i of the gas species i, with a partial pressure p_i and a molar weight (m_i) at a temperature T, striking the substrate surface per unit area in a unit time, we obtain:

$$J_i = \frac{p_i}{\sqrt{2\pi k_B m_i T}}$$

where k_B is the Boltzmann constant. From this formula we can calculate that the background pressure of the residual gas in the MBE chamber, in order to ensure the purity of the film, has to be less than 10^{-9} Torr, therefore in the UHV regime.

MBE is conceptually very simple: the constituent elements are heated in the effusion cells until they evaporate and impinge on the substrate surface, after the shutter opening; there they diffuse on the surface and finally bond to lattice sites. In the case of semiconductors epitaxy the substrate has to be heated up to several hundreds of degree centigrades to prevent the formation of an amorphous layer, due to a too low adatoms mobility. Despite the simplicity of this picture, there are many processes going on at the substrate surface during the epitaxial growth[2], as shown in Fig. 1.1. Atoms from the molecular beam arrive at the surface of the crystalline substrate (a) and may diffuse over the surface when the activation energy for diffusion is overcome (b). When two or more atoms meet (c), they

form the nucleus of an island, which can either grow to a stable two-dimensional island by attachment of further diffusing adatoms (d) or decay by detachment of atoms (e). The nucleus for which the probabilities to grow or decay are equal is called critical nucleus. Nuclei which are larger than the critical nucleus are called stable two-dimensional islands. Nuclei smaller than the critical nucleus are called sub-critical nuclei or embryos. Other possible processes are the direct impingement on two-dimensional islands (f), the attachment at a step (g) and the desorption of the atoms from the terrace (h).

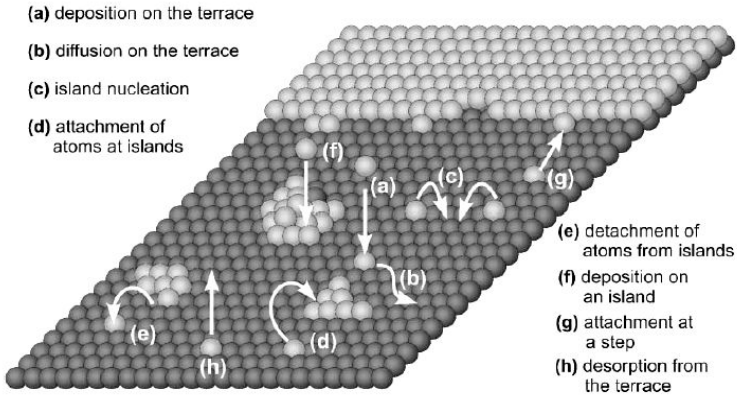

Fig. 1.1 : Schematic representation of the processes occurring during epitaxial growth. From Ref. [2].

In thermodynamic equilibrium all processes proceed in opposite directions at equal rates, as required by consideration of detailed balance. Thus, for example, in equilibrium adsorption, surface processes such as condensation and re-evaporation, decay and binding of 2D clusters must be in detailed balance. There is thus no net growth and the system can be described by unchanging macroscopic variables, while microscopically the system is continuously changing via these various surface processes. By contrast, crystal growth is a non-equilibrium kinetic process and the final macroscopic state of the system depends on the route taken through the various reaction paths indicated in Fig. 1.1. The state which is obtained is not necessarily the most stable, but is kinetically determined. In general, certain parts of

the overall process may be kinetically forbidden, others may be in local thermodynamic equilibrium, and some will be kinetically rate-limiting[3]. The type of growth is largely determined by the ratio between the adatoms diffusion rate *D* and deposition flux *F*. As depicted in Fig. 1.2, the thermodynamic regime is characterized by high *D/F* ratio, while the kinetic regime can be found at low *D/F* ratios. Semiconductor nanostructures are usually grown at intermediate *D/F* and their morphology is determined by the complex interplay between kinetics and thermodynamics[4].

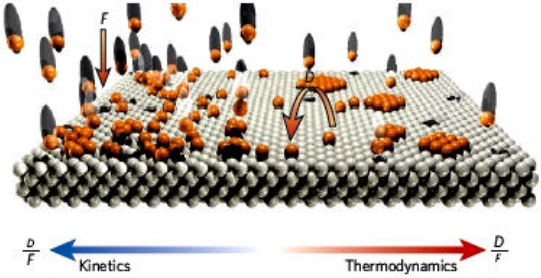

Fig. 1.2 : Atomic-scale view of growth processes at surfaces. From Ref. [4].

According to Venables[3,5], the maximum, or saturation, stable islands density n_x can be expressed as a function of the experimental variables *F* and *T*, by:

$$n_x \propto \left(\frac{F}{\nu}\right)^p \exp\left(\frac{E}{k_B T}\right)$$

where ν is the atomic vibration frequency and *E* an energy term containing the above mentioned atomic processes. Values for *p* and *E* are reported in Table 1 for 2D and 3D clusters. Different energies are considered: E_i the energy of the critical nucleus, E_d the activation energy for surface diffusion and E_a the adsorption energy. Depending on the growth conditions, one (or more) of the phenomenon occurring during the growth will dominate and is possible to recognize different regimes. In the extremely incomplete condensation regime, growth by direct impingement is most important, while in the complete condensation, re-evaporation is negligible. In between there

is the initially incomplete regime, where most cluster growth occurs by diffusive capture, at least initially.

Regime	3D islands	2D islands
Extremely incomplete	$p = 2i/3$ $E = (2/3)[E_i+(i+1)E_a-E_d]$	$p = i$ $E = [E_i+(i+1)E_a-E_d]$
Initially incomplete	$p = 2i/5$ $E = (2/5)[E_i+iE_a]$	$p = i/2$ $E = [E_i+iE_a]$
Complete	$p = i/(i+2.5)$ $E = [E_i+iE_d]/(i+2.5)$	$p = i/(i+2)$ $E = [E_i+iE_d]/(i+2)$

Table 1 : Parameter dependencies of the maximum cluster density in various regimes of condensation.

This treatment is very important since it predicts a defined relationship between the density of stable cluster on the surface and the growth parameters that we can actually control: the molecular beam flux and the substrate temperature. The stable cluster density is expected to depend with a power law on the flux and exponentially on the substrate temperature.

1.2 Epitaxial growth modes

The term "epitaxy" comes from the combination of the Greek words "ἐπὶ" which means "on" and "τάσσω", which means "arrangement". Therefore the growing epitaxial layer has a precise structural relationship with the substrate. Both the film and the substrate are crystalline and if their crystal structures are not the same, several different epitaxial relationship may exist. A simple and famous model for describing the most important modes in crystal growth was firstly proposed by Bauer[6] in 1958, by considering the surface energy of a material A growing on a substrate B in a vacuum reactor. As shown in Fig. 1.3, we can define three surface energies: γ_A as the surface tension of material A exposed to the vacuum;

γ_B as the surface tension of material B exposed to the vacuum and γ_{AB} as the surface tension of the two materials in contact. When the interaction between the two materials is energetically favourable, the system will try to maximize the surface of contact between them and this will lead to the growth a film which completely wets the substrate. In terms of surface energies this is corresponding to the situation in the left hand side of the figure below, where: $\gamma_{AB} \leqslant \gamma_B - \gamma_A$. On the contrary when the interaction between A and

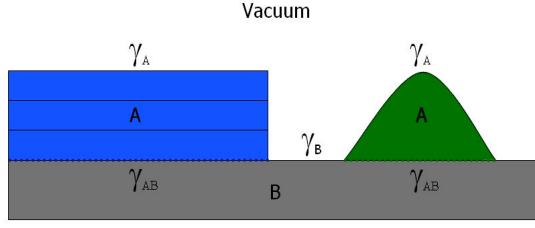

Fig. 1. 3 : Schematic representation of the growth of a material A on a substrate B in vacuum. The limit cases of complete wetting (a) and islands formation (b) are shown in the left and right hand side, respectively.

B is not stabilizing the system, a reduction of the contact area will be observed. In this case the growth of A will proceed directly with the formation of 3D islands. The surface energy balance in this condition will give: $\gamma_{AB} > \gamma_B - \gamma_A$, as seen in the right hand side of Fig. 1.3. This arguments, based on simple considerations about the surface energy of the A/B/Vacuum system, can indeed explain the variety of growth modes observed in heteroepitaxial crystal growth. We recognize three different modes, which are named: Frank-Van der Merwe (F-VdM) or layer-by-layer, Volmer-Weber (V-W) or island growth and Stranski-Krastanov (S-K) or layer plus island. The first two growth modes correspond to the above mentioned conditions of very high (low) affinity between the A and B materials, resulting in the F-VdM (V-W) growth. However an intermediate case is often found in semiconductor epitaxy, when the interfacial energy increases with the thickness of the layer. In such case, the thermodynamic condition for the layer-by-layer growth is fulfilled only below a certain thickness, called critical thickness. Further growth of the layers will now result in the formation of islands on the top of the 2D film,

which is named wetting layer (WL). This growth mode (S-K) is quite common and very studied since two technologically important systems, InAs on GaAs and Ge on Si, follow the S-K growth. In Fig. 1.4 we report a schematic representation of the three growth modes. It is worth remembering that in the F-VdM mode, no deposition occurs on the top layer until the growth of the bottom layer is completed and that in the V-W mode no WL is formed, between the islands. Moreover we observe the layer-by-layer growth, in systems which possess a very similar structure and chemical affinity (AlGaAs/GaAs), while the island growth is typical when strong differences are present between A and B (GaAs/Si). There are many elements to take into account in order to predict which one of the modes will occur in the growth of a material on a substrate, but strain and the surface chemistry are often the key factors. Indeed in highly strained systems

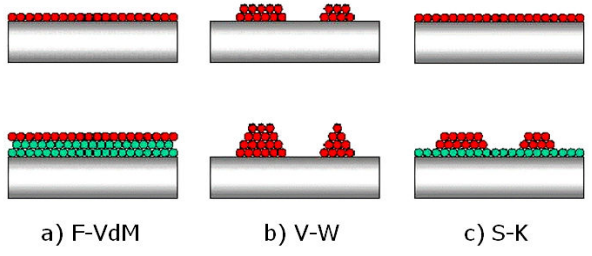

Fig. 1.4 : Schematic representation of the three modes in epitaxial growth: layer-by-layer or F-VdM, island growth or V-W, layer-plus-island or S-K.

an island growth might be favourable, while when no strain is present a layer-by-layer growth might occur. At intermediate case (small strain) a S-K growth can be observed. The chemistry of the surface has a strong influence on the growth, because for instance the matching between a polar and a non-polar surface, might introduce a lot of defects in the film, like dislocations, even if A and B are nearly lattice-matched (GaAs/Ge). In the S-K growth mode the islands formation is due to the relief of the strain induced in the epilayer by the presence of a certain lattice mismatch. Obviously if no strain is present between A and B, the S-K growth cannot take place. However the island nucleation is not the only mechanism for the reduction of

the elastic energy within the thin film. Indeed the introduction of a dislocation might also act efficiently in this sense, thus the islands formation and the introduction of dislocations are competitive phenomena.

In our case we have fabricated GaAs nanostructures by following the Droplet Epitaxy (DE) growth technique, which is an alternative method for the formation of 3D islands on both lattice-matched and lattice-mismatched materials. However the concepts introduced here are of universal application and therefore very useful for a general analysis on crystal growth.

1.3 Properties of the GaAs/AlGaAs system

In this work, we focused our research on the GaAs/AlGaAs materials and we will therefore describe the main structural and electronic properties of this system[7]. These materials possess nearly the same lattice constant, being a_{GaAs} = 5.65325 Å and a_{AlAs} = 5.65330 Å at 300 K and the same crystal structure, the zincblende, which is shown in Fig. 1.5. Each atom is linked by partially covalent bonds to

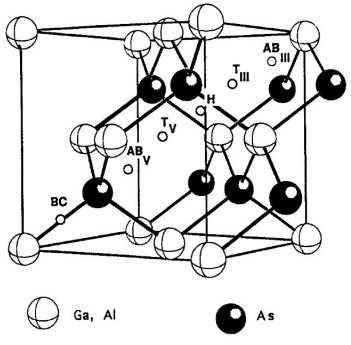

Fig. 1.5 : The cubic unit cell for the zincblende structure. White and shaded balls represent group III and group V atoms, respectively. High symmetry interstitial sites are also shown. BC is the bond centre site, T the tetrahedral site, AB the anti-bonding site, and H the hexagonal site. The subscripts III and V indicate the first nearest neighbour atom. From Ref. [7].

four atoms of the other type; the next nearest neighbour distance for the two compounds is about 0.245 nm. Usually the Vegard's law is assumed for $Al_xGa_{1-x}As$, which yields a linear dependence of the measured lattice constant on the alloy composition[8]. The $Al_xGa_{1-x}As$ alloy covers the whole composition range from 0% to 100%, with Al cations substituting Ga cations, moving from the pure GaAs to the pure AlAs. These features make the growth of GaAs/AlGaAs thin films a prototypic example of the F-VdM growth mode. High quality 2D layers of GaAs/AlGaAs can be grown by MBE, exploiting the structural and chemical affinity of the two materials.

The radiative recombination process in semiconductors is mainly determined by transitions involving band extrema or bound states (excitons, impurities, and defects) where the structure and the shape of the lowest conduction bands and of the highest valence bands are of utmost importance. Therefore, only the extrema of the conduction and valence bands will be discussed in the following. The calculated electronic band structure[9] of GaAs (left panel) and AlAs (right panel) are shown in Fig. 1.6. The top of the valence band for the two compounds is at the Γ point of the Brillouin zone (BZ) and has the shape characteristic of zincblende type semiconductors. It is

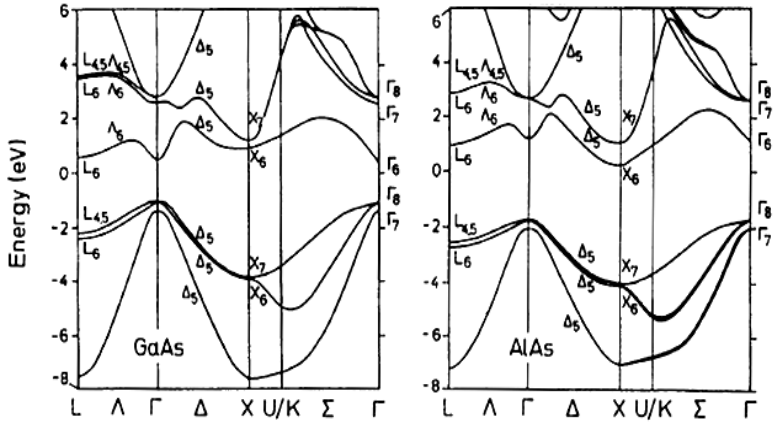

Fig. 1.6 : Calculated electronic band structure for GaAs (left panel) and AlAs (right panel). From Ref. [9].

sixfold degenerate and is split by the spin-orbit interaction into an upper fourfold degenerate Γ_8 level and a lower twofold degenerate Γ_7 level. The main properties of the conduction and valence band extrema are[10]: (i) the conduction band minimum at Γ has a cubic symmetry, it is practically isotropic and slightly non-parabolic; (ii) the four conduction band minima at the L points and the three at the X points have axial symmetry; (iii) at X the conduction band may have a "camel's back" structure, that means the minima might not occur at X but away in the A direction of the BZ; (iv) the two upper valence bands (the heavy hole and the light hole bands) are degenerate at the centre of the BZ and the effective masses of the two bands are essentially different only in the close neighbourhood of Γ; (v) the lower band, or split-off band, has its maximum a few tenths of eV below that of the upper valence band, it is isotropic, but not parabolic. The difference in the energy gaps of GaAs (lower) and AlGaAs (higher) makes them attractive from the application point of view, since by burying a thin layer of GaAs in an AlGaAs matrix it is possible to exploit the quantum confinement effects. In $Al_xGa_{1-x}As$ alloys, the energy gap moves towards higher energy as x increases, following the relationships: $E_g^{\Gamma} = 1.5194 + 1.36\,x + 0.22\,x^2$ and $E_g^{X} = 1.988 + 0.207\,x + 0.055\,x^2$ for the energy gaps at the Γ and X points of the BZ, at low temperatures[7]. As it is clearly visible in Fig.

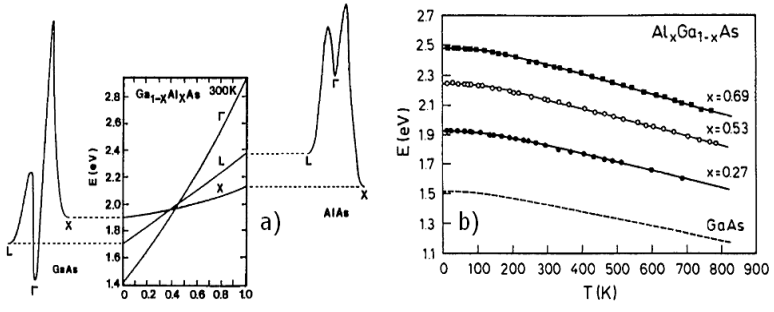

Fig. 1.7 : The schematic variation of the Γ, L, and X minima in $Al_xGa_{1-x}As$ alloys as a function of x. On the x = 0 and on the x = 1 side, the conduction band for GaAs and for AlAs is shown (a). The temperature dependence of the direct gap energy (E_g^{Γ}) of $Al_xGa_{1-x}As$ for some values of x. The dashed line gives the temperature dependence of E_g^{Γ} for GaAs. Modified from Ref. [11].

1.7 (a), by increasing the Al content a cross-over is observed, around x = 0.45, where the minimum of the conduction band is no more at Γ, but at X. From this composition to the pure AlAs, the nature of the band gap in $Al_xGa_{1-x}As$ changes from direct to indirect[11]. In Fig. 1.7 (b) the temperature dependence of the E_g^{Γ}, which follows the Varshni's semi-empirical relation, is shown for different Al compositions and for pure GaAs[9].

An important part of this work was devoted to the fabrication of GaAs quantum nanostructures embedded in $Al_{0.3}Ga_{0.7}As$, for the optical investigations. The band alignment of such a system is very important for the interpretation of the data on its optical activity. We therefore report in Fig. 1.8 the energy levels of electrons and holes confined in a GaAs/$Al_{0.3}Ga_{0.7}As$ quantum dot (QD), studied using photoluminescence (PL) measurements under high pressure, as well as micro-PL investigations on a single QD[12]. From the high-pressure experiment, the band alignment of the GaAs QDs was determined. The GaAs QD valence band heavy hole ground state and the excited

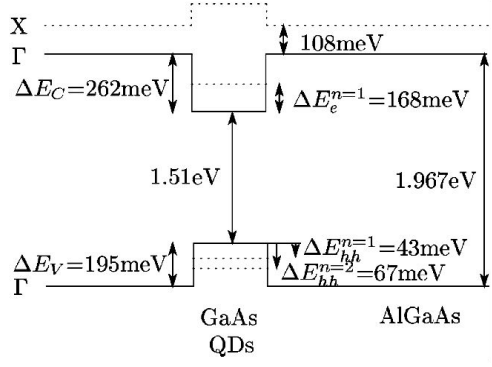

Fig. 1.8 : Reconstructed band alignment of the GaAs/$Al_{0.3}Ga_{0.7}As$ QDs. From Ref. [12].

state energy difference was 24 meV. From the micro-PL experiment, the GaAs QD conduction band electron ground state and the first excited state energy difference was found to be 96 meV.

Very similar band structure is therefore expected also in the case of the quantum nanostructures grown in our work.

1.4 Surface reconstructions of GaAs (001)

Semiconductor surfaces are said to be reconstructed if their symmetry parallel to the surface is lower than that of the bulk solid. Even if the symmetry of the surface unit cell is the same as that for the bulk, the atoms in the surface region typically move to large distances (e.g. tenths of angstroms) relative to the positions which they would have occupied in a truncated bulk lattice. Such surfaces are said to be relaxed (as opposed to reconstructed). The term "reconstructed", in the generic sense, does not take into account whether the surface symmetry is lowered or not. Two basic concepts are required to understand why semiconductor surfaces reconstruct: chemical bonding and charge neutrality. When a surface is formed, some of the atomic bonds will be broken, leading to associated surface charge densities, which contain only one unpaired electron. Such dangling bonds are unstable and therefore extremely reactive. Hence, the atoms in the surface region relax from their bulk positions in order to reduce the surface free energy, by forming new bonds. Reaching a structure which exhibits a local minimum in the surface free energy implies that the chemical valencies of the surface species are satisfied in the reconstructed geometry. The requirement of the charge neutrality leads to the prediction of certain specific allowed stoichiometries for the surface compounds. Most importantly, which composition actually occurs depends on the conditions under which the surface was prepared. In order to describe the phenomena ruling the process of surface reconstruction of clean low-index faces of tetrahedrally coordinated elemental and compound semiconductors, Duke[13] proposed an explicit set of five principles:

Principle 1: Reconstructions tend either to saturate surface dangling bonds via rehybridization or to convert them into non-bonding electronic states.

Principle 2: In many cases (and in all quasi-one dimensional ones) surfaces can lower their energies by atomic relaxations leading to

semiconducting (as opposed to metallic) surface state eigenvalue spectra.

Principle 3: The surface structure observed will be the lowest free-energy structure kinetically accessible under the preparation conditions

Principle 4: Surfaces tend to be autocompensated.

Principle 5: For a given surface stoichiometry, the surface atomic geometry is determined primarily by a rehybridization-induced lowering of the surface state bands associated with either surface bonds or (filled) anion dangling bond states.

For the surface reconstructions of compound semiconductors, the last three principles are required to describe their construction. A surface structure satisfies Principle 4 if it is possible to have all the dangling bonds on the electronegative element (As) occupied and all the dangling bonds on the electropositive element (Ga) empty, given the number of available electrons. If this condition is fulfilled, the surface will be semiconducting, whereas partially filled dangling bonds may lead to a metallic surface. Charge transfer from cation (Ga) to anion (As) transforms the As dangling bond into an s-type occupied state and the Ga dangling bond into a p-type empty state. As a result, the surface Ga atoms are in a sp^2-type bonding configuration, almost planar with their nearest neighbour As atoms, while surface As atoms are in a sp^3- type bonding configuration with nearest neighbours. For given surface composition, structures satisfying Principles 4 and 5 correspond to local (but not necessarily global) minima in the surface free energies. On the other hand, surface structures observed on a semiconductor surface, in general, will depend on the process used to prepare the surface. Thus the observed structure corresponds to the lowest free-energy minimum which can be reached kinetically by the process conditions used to prepare the surface, as stated by Principle 3.

In the following we will describe the surface reconstruction of

GaAs (001) surface[14], with a special attention on the three most important cases of the (2x4), c(4x4) and (4x6) reconstructions, being them crucial, not only for general purposes, but also for the themes treated in this work. In the first two cases, the surface is As-rich, being c(4x4) the most As-rich phase, while the third case is the most Ga-rich reconstruction.

As-rich (2x4): this reconstruction has been most extensively studied, because the surface during the MBE growth usually shows the (2x4) reconstruction. Although from early investigations the (2x4) surface have been interpreted in terms of another model[15], later observations, including STM, X-ray diffraction, RHEED and first-principles calculations, supported the $\beta 2(2x4)$ model, shown in Fig. 1.9. Careful studies based on RHEED analysis permitted the classification of the (2x4) surfaces into three phases[16]: the α the β and the γ, where the α and the γ phases emerge under less and more As-rich MBE conditions, respectively. In the range of 550-510 °C, where the surface shows sharp (2x4) RHEED patterns, the reconstruction is characteristic of the β phase. While the (2x4) reconstruction is observed in the range of 480-600 °C, significant broadening of the (2×4) RHEED pattern was observed at the lower (below 500 °C) and higher (above 580 °C) ends of the temperature region of the (2×4) phase. Finally, the (2x4) RHEED pattern begins to give way to the diffuse (1x1) features above 600 °C. On the other hand, when the

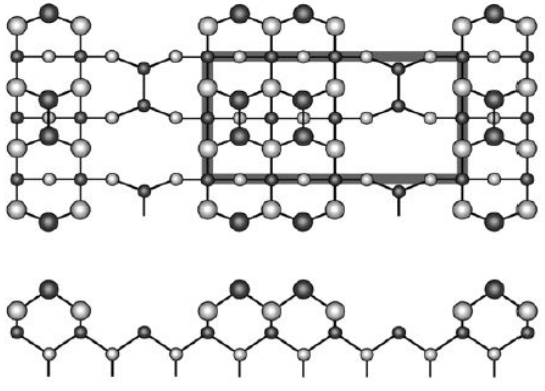

Fig. 1.9 : Structure models for As-rich GaAs(001)-β2(2×4) surface reconstructions. Filled (open) circles denote As (Ga) atoms. From Ref. [14].

c(4x4) surface is heated without As fluxes, sharp (2x4) RHEED pattern have never been observed. This means that the ordered (2×4) surface is kinetically accessible only under As-beam irradiation. In the range of 510-550 °C, the surface reconstruction is stable against a slight change in the temperature, and, therefore, can be regarded as equilibrium phase. In this conditions, the β2(2x4) is the structural model which correctly represents the atomic arrangement at the surface. On the contrary, the (2×4) surface changes its structure with substrate temperature below 500 °C to the γ phase and above 550 °C to the α phase. Fig. 1.10 (a) and (b) show typical RHEED patterns observed along the [1-10] and [110] directions for the GaAs(001)-(2x4) surface under the As_4 flux at 540 °C, respectively (β phase). During the standard homoepitaxy of GaAs, this kind of RHEED pattern is commonly observed. On one hand, sharp spots lying on a semicircle, the zeroth-order Laue zone, are clearly observed in the [1-10] direction (a), which are what would be expected for a well-ordered surface. On the other hand, in the [110] direction (b), spots are observed for integer order reflections, but not for half-order ones. Instead, extended streaks are observed in the half-order positions, which is ascribed to the presence of one dimensional disorder on the (2×4) surface.

Summarizing, the GaAs(001)-(2x4) surface consists of the well-ordered β2 structures in a relatively wide range of substrate temperature under As fluxes. At the higher end of the temperature region of the (2x4) phase, the surface contains a high density of defects with a local atomic geometry, compatible with the appearance of the α phase. On the other hand, the β2(2x4) structure coexists with

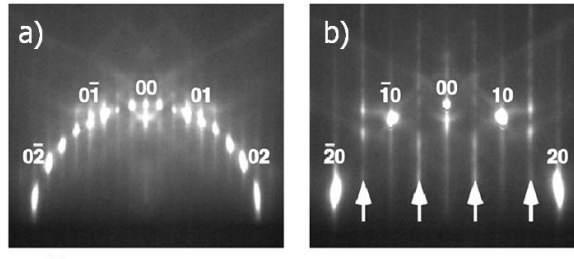

Fig. 1.10 : Typical RHEED patterns taken along the [1-10] (a) and [110] (b) directions of the GaAs(001)-(2×4) surface under the As_4 flux at 540 °C. From Ref. [14].

c(4x4) domains at the lower end of the temperature region, giving rise to the γ phase.

As-rich c(4x4): this reconstruction of the GaAs (001) surface is usually observed under extremely As-rich MBE conditions, and, therefore, has been believed to be the most As-rich phase. Its surface structure can be composed by either As-As dimer or Ga-As dimer structures by changing the incident As molecular species, as shown in Fig. 1.11 . Indeed two types of atomic structures for the c(4x4) were found[17,18] and this could explain the reported wide range of As coverage for this configuration. As-rich c(4x4) phases can be prepared by cooling the (2x4) under As irradiation, since the sticking probability of arsenic molecules increases with decreasing substrate temperature. Upon cooling, the transition from the (2x4) to the c(4x4) starts at around 500 °C and is completed at around 480 °C. The two types of c(4x4) reconstructions are easily observed when the As_2 molecular beam is used, due to the high sticking probability of that arsenic molecule which can promote the change from the c(4x4)α (Ga–As dimer structure) to the c(4x4)β (As–As dimer structure) phase. Indeed the As coverages on the As-rich reconstructions are: 0.75 ML, 1.0 ML and 1.75 ML for the (2x4), c(4x4)α and c(4x4)β, respectively. It was observed that the structure change between c(4x4) and (2x4) is reversible under As fluxes, while

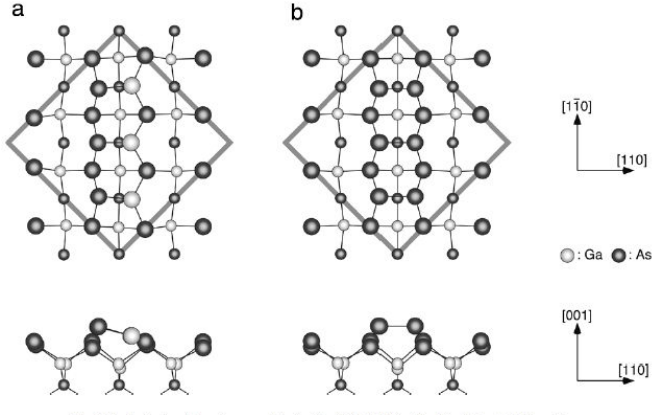

Fig. 1.11 : Optimized structure models for the GaAs(001)-c(4×4) surface: Ga-As dimer model (a) and As-As dimer model (b). From Ref. [14].

when the c(4×4) surface is heated without As fluxes the formation of ordered c(4×4)α and β2(2x4) phases are kinetically limited. Carefully observing the RHEED patterns, it was found that the relative intensities are different between the two phases. For example, a noticeable difference is observed in the 10 and -10 intensities (arrows in Fig. 1.12), however, since the relative intensities in RHEED patterns strongly depend on the glancing angle and energy of incident electrons, it is rather difficult to distinguish the two phases using RHEED patterns.

It has been reported[19] that that the (2x4) and c(4x4)β structures are more stable than the c(4x4)α structure under Ga- and As-rich conditions, respectively. However, the formation of the c(4x4)β phase is not easily observed, caused by the high activation barrier for the direct structure change from the β2(2x4) to the c(4x4). Indeed Ga atoms (0.75 ML) at the second layer of β2(2x4) structure have to be completely removed in order to perform this transformation. On the other hand, the removal of fewer Ga atoms (0.375 ML) is required for the structure change from β2(2x4) to c(4x4)α. Therefore the c(4x4)α structure has a lower barrier for its formation and plays a key role in the structure change from (2x4) to c(4x4)β. It is also possible that the two types of atomic structures are coexisting and this phenomenon would explain the reported wide

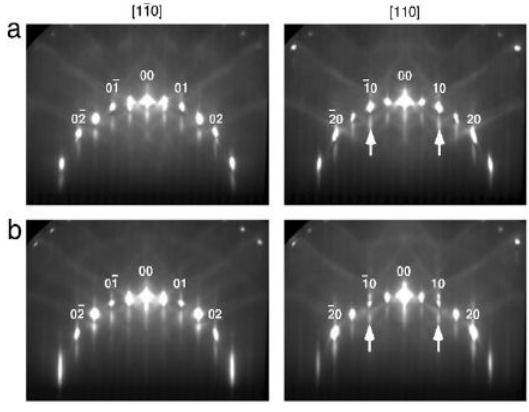

Fig. 1.12 : RHEED patterns taken from the c(4×4)α (a) and c(4×4)β (b) phases at room temperature from [1-10] (left panels) and [110] (right panels). From Ref. [14].

range of As coverage on the c(4x4) surface, since the As coverage of the Ga-As dimer model is 1.0 ML, while in the case of As-As dimer model is 1.75 ML.

The difference in the experimental results between the use of As_4 and As_2 can be ascribed to the higher sticking probability of As_2 molecules. Indeed As_2 molecules easily react with both (2x4) and c(4×4)α surfaces, while the sticking probability of As_4 on c(4×4)α is much lower than that on (2x4). The reaction of As_4 molecules with GaAs (001) is very complex and involves the dissociation into As_2 precursors, before being incorporated into the lattice sites. For this to happen, pairs of As_4 molecules are required to interact on adjacent Ga sites in advance[20], but while there exist three-coordinated Ga atoms (0.5 ML) at the second layer on the β2(2x4) surface, fewer Ga sites are available on the c(4×4)α structure, which might make difficult the reaction with As_4 molecules with the α phase to form the β phase. However it is very important to mention that the c(4x4)β phase can be formed under very high As_4 fluxes at low temperatures, as reported by Nagashima et al.[21].

In conclusion the c(4x4) surface has being shown to have two types of atomic structures, the c(4×4)α (Ga-As dimer structure) and the (4×4)β (As-As dimer structure), depending on the preparation conditions. Both structures do not have any unsaturated Ga and As dangling bonds, thereby satisfying Principles 4 and 5 mentioned before. The incident As molecular species play an important role in the formation of these phases. The c(4x4)β structure, which is the most stable structure in the extremely As-rich condition, is easily formed under As_2 molecular beams or under very high As_4 beams at low temperature.

Ga-rich (4x6): Ga-rich reconstructions are usually obtained by heating the As-rich c(4x4) and (2x4), without As fluxes. A huge variety of this type of reconstructions has been reported: (3x1), (1x6), (2x6), (3x6), (4x6), (6x6) and c(8x2). However we will mainly focus on the (4x6), since it represents the most Ga-rich phase and it is the reconstruction which appears before the nucleation of droplets during Ga supply to an As-rich surface, as commonly observed in our growth experiments. When the GaAs (2x4) surface is heated above 450 °C in

a good UHV condition the surface has the (6x6) structure and as the temperature is increased above 580 °C the reflections associated with a c(8×2) reconstruction start to emerge and the (6×6) reflections disappear at 600 °C. The c(8×2) structure is stable in the range of 600–680 °C, beyond which the surface begins to roughen. Only when the sample with the c(8x2) symmetry is rapidly cooled from 600 °C, the c(8x2) phase could be preserved at lower temperatures, meaning that this transition is kinetically limited. Instead, as shown in the phase diagram of Fig. 1.13, the intrinsic (4x6) reconstruction can be obtained by depositing a submonolayer coverage of 0.15-0.30 ML of Ga on the (6x6) surface at 300°-500 °C. At these coverages, a distinct (4x6) periodicity is observed in RHEED patterns. Further Ga deposition do not change the (4x6) RHEED patterns, which presumably results in the formation of Ga droplets.

On the basis of STM observations, the structure model shown in Fig. 1.14 has been proposed[22], characterized by two Ga-As dimers,

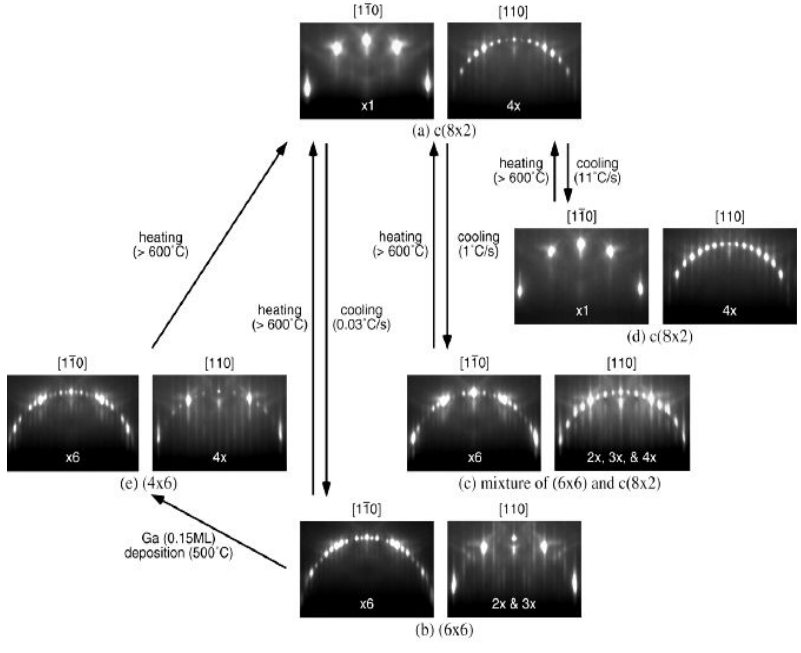

Fig. 1.13 : . RHEED patterns observed on the Ga-rich surface reconstructions. From Ref. [14].

four surface As atoms at faulted positions, and two subsurface Ga-Ga dimers per (4x6) unit cell. The As coverage of the structure model is 1/12 ML, which is smaller than that for c(8×2) (1/4 ML): the proposed (4×6) model is more Ga-rich than the c(8x2) model, as confirmed by XPS measurements.

In summary, the (4x6) surface has been found as the most Ga-rich phase amongst the GaAs (001) reconstructions. This is more stable than the c(8x2) structure and energetically favourable at the Ga-rich limit, even though both of them satisfy Principles 4 and 5: charge transfer from Ga to As transforms the Ga dangling bonds into p-type empty states and As dangling bonds into s-type occupied states.

In conclusion MBE-grown GaAs (001) shows As-rich c(4×4)α,

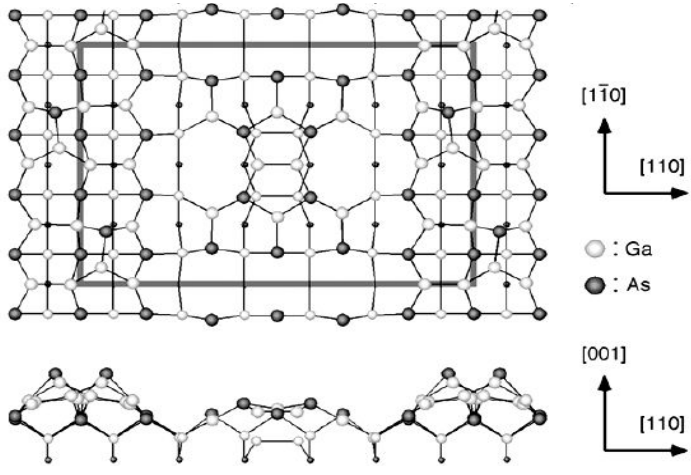

Fig. 1.14 : The structure model for the GaAs (001)-(4×6) surface. From Ref. [14].

c(4×4)β and (2×4) reconstructions, whose As coverages are 1.0 ML, 1.75 ML and 0.75 ML, respectively. While the (2x4), in its three phases (α, β and γ), is the reconstruction appearing during the standard growth of GaAs, the two phases of the c(4x4) are observed at lower temperatures, due to the higher sticking of As in these

conditions. The existence of two types of c(4×4) structures, of Ga-As dimer structure and As-As dimer structure, provides an explanation for the wide range of As coverages reported in the literature. Different types of Ga-rich reconstructions are formed, depending on the preparation conditions. The (4x6) structure, consisting of surface Ga-As dimers and subsurface Ga-Ga dimers is energetically stable at the extremely Ga-rich condition, with an As coverage is 1/12 ML and is most Ga-rich phase of GaAs (001) surface.

As will be clear in the following sections, the investigations on the surface reconstructions during our growth experiments represents a very important part of our work. We therefore presented the state-of-the-art understanding of the GaAs (001) surface reconstructions, stressing the most important concepts, in view of the presentation of our results. For a deeper analysis on these topics, we recommend a recent review by Ohtake[14].

Chapter 2

"inspired me truly you did from the start
to not be afraid and to follow my heart
there's a piece of you with me they can't tear apart,
forever"

(from "Forever" by Dropkick Murphy's)

Droplet Epitaxy

This Chapter is dedicated to the description of the Droplet Epitaxy (DE) technique, the method we studied and used for the fabrication of GaAs nanostructures in the present work. We will introduce the background of the invention first and then describe the proposal of this method as an efficient technique to obtain semiconductor quantum nanostructures. Later sections will be devoted to a quick overview on the development of the growth method from the early Nineties until more recent evolutions, including structural and optical properties, towards the fabrication of devices based on DE-grown nanostructures.

2.1 Background of the invention

One predominant topic in the physics of the last 30 years is the study of quantum confinement effects in semiconductor nanostructures, especially in Quantum Dots (QD). Because of their electronic structure, these systems can be regarded as artificial atoms, showing a discrete spectrum of energy levels. Since the beginning of the Eighties the scientific community recognized the potential of zero-dimensional quantum nanostructures as active elements for a new generation of electronic devices. In their pioneeristic paper[23], Arakawa and Sakaki suggested a significant improvement on the performances of semiconductor lasers exploiting three-dimensionally confined nanostructures. However, as clearly reported in their publication, on that time *"...the fabrication of such structures at present is still technically difficult even with the most advanced device technology..."*. Therefore the research on this field and the technological applications were hindered by the lack of production methods for these special type of materials. In fact one of the main research topics of that period was the fabrication of very sharp and high quality heterostructures. Thin film growth, driven by the technological interest for Quantum Well (QW) based solid state devices, was indeed attracting lot of attention and efforts. This picture can explain why during the Eighties, obtaining an heteroepitaxial three-dimensional growth of islands in a lattice-mismatched system was considered as a problem, more than an advantage. However lot of studies were performed in that period on the role of strain and composition on the critical thickness and on the formation of misfit dislocations in both Ge/Si[24-26] and InAs/GaAs[27] systems, including the discovery by Eaglesham and Cerullo of the dislocation-free growth of Ge islands by the Stranski-Krastanow mode on Si (100)[28]. Few years later, at the beginning of the Nineties, the application of the S-K growth mode to semiconductor heteroepitaxy was recognized as a promising method for the fabrication of QDs[29] and this drove an enormous interest for

both the fundamental and practical studies. It was in this scene that Droplet Epitaxy was firstly proposed; a period when these new breakthroughs opened the route for the application of zero-dimensional nanostructures to semiconductor science and technology.

As already mentioned, a lot of attention was devoted to the realization of perfectly sharp interfaces and atomically smooth two-dimensional layers. One of the suggested problems to overcome was the formation of oval defects during the high temperature MBE growth of GaAs with a low V/III ratio, which was indicated as the origin of surface roughness[30]. Investigations on this topic lead to the discovery of the formation of III-column element droplets in these conditions and their subsequent annihilation caused by the As supply[31-34]. In a paper by Isu et al.[34], the scanning microprobe RHEED[35] (μ-RHEED) system was used to directly image the GaAs (001) surface during alternated supply of Ga and As. As we report in Fig. 2.1 (a)-(f) Ga droplets were formed under Ga irradiation on GaAs surface at 610°C and supplied for totally 1 ML. Just after Ga cell opening, dark spots were detected, that progressively enlarged, without changing their number. These dark spots are believed to correspond to Ga droplets, formed by the excess amount of Ga atoms at the surface, without bonds to As. In panels (g)-(l) the scanning

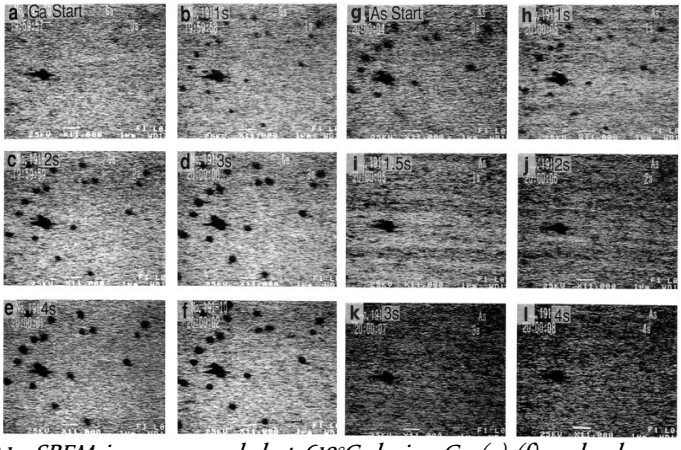

Fig. 2.1 : SREM images recorded at 610°C during Ga (a)-(f) and subsequent As (g)-(l) supply on GaAs (001) surface. Ga droplets appeared as dark spots that shrank and disappeared after As irradiation. From Ref. [34].

reflection electron microscope (SREM) images are recorded, during the subsequent supply of arsenic to the same surface area of the sample. Dark spots (Ga droplets) shrank and then disappeared after a sufficient amount of As was supplied. It is worth mentioning that bright regions around the droplets were observed before they disappeared. Since the Ga-rich surface was brighter than the As-stabilized surface under their conditions of RHEED, the bright region seemed to be Ga-rich regions. The authors suggested that Ga atoms diffuse from the droplets and form a monolayer of GaAs during the As supply.

In a second paper by Inoue[33], a similar experiment was performed, following with an *in-situ* molecular beam epitaxy/scanning reflection electron microscope/scanning electron microscope (MBE-SREM-SEM) hybrid system the nucleation of Ga droplet and their annihilation at 610°C. Again it was found that Ga droplets are formed on a Ga-stabilized surface as soon as Ga atoms are supplied, as shown in Fig. 2.2 a), clarifying that Ga on a Ga layer cannot form a

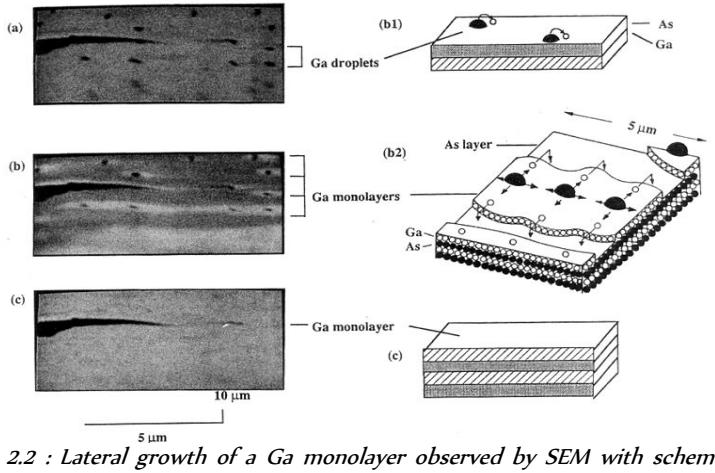

Fig. 2.2 : Lateral growth of a Ga monolayer observed by SEM with schematic illustrations. (a) Ga droplets (dark dots) on Ga top layer. Dark horizontal band in the left side is a marker for focusing. (b) 0 s (top) to 5 s (bottom) after As supply. Dark areas are As top layer and the bright areas around the droplets are laterally growing Ga monolayers. The size increase toward bottom reproduces the growth history of monolayer islands. (c) 15 s (top) to 20 s (bottom) after. Complete coverage by Ga monolayer leaving tiny droplets. From Ref. [33].

continuous film. When As was supplied to the already formed Ga droplets, GaAs mounds were formed, supporting the previous suggestion that droplets caused roughening of the grown layer. Investigating the dynamics of the formation of the GaAs thin film developed caused by droplets annihilation, it was found that Ga layers evolved laterally from the droplets over the As top layer and covered by As again. A growth model was presented and shown in the right hand side of Fig. 2.2. When the surface is covered by As, it is possible for Ga atoms in the droplets to find stable As sites. They come off the droplets and attach themselves to the nearest As atoms. The Ga atoms that follow migrate over the new Ga overlayer until they reach the As layer. This process continues until the surface is completely covered by Ga. Finally the authors suggested this new growth technique as being promising for atomic layer controlled growth of heterostructures.

Almost simultaneously to this publications Droplet Epitaxy was proposed for the first time at the 6th Conference on Molecular Beam Epitaxy held in La Jolla, California on 27-31 August 1990.

2.2 Proposal by Koguchi

Initially presented at the 6th Conference on Molecular Beam Epitaxy, the DE concept was published for the first time by Koguchi et al. in a paper[36] entitled: *"New MBE growth method for InSb quantum well boxes"*, published in 1991. The authors were researching on the nearly lattice-matched InSb/CdTe system and proposed a new growth protocol based on the splitting of the III-column and V-column elements supply, which allowed for the fabrication of InSb nanostructures on CdTe. They also recognized this method as promising for the realization of *"a quantum well box system by covering the InSb microcrystals by a CdTe epitaxial overlayer"*. The concept of DE is therefore very simple: in order to form a III-V

nanostructure, the two constituent elements are individually supplied, exploiting the property of elements such as In, Ga, Al to self-aggregate in nanometric droplets, due to their high surface tension. These III-column element reservoirs are then transformed into a III-V semiconductor nanostructure by irradiation of a V-column element. Following this procedure it is thus possible to fabricate 3D nanometre-sized crystals (originally named "quantum well boxes" and later commonly called QDs) that can be buried into a higher bandgap matrix, in order to exploit the quantum confinement. In the original publication, the two steps of the DE growth were followed by means of RHEED and High Resolution Scanning Electron Microscopy (HRSEM), as reproduced in Fig. 2.3. After the deposition of pure In on CdTe surface at 200°C, the RHEED pattern showed the halo feature (panel a), typical of liquid materials and the formation of In droplets was further confirmed by the HRSEM image in (c). During the subsequent Sb molecular beam flux, supplied at the same substrate temperature, the RHEED pattern turned to spotty (b), indicating the formation of InSb 3D crystals, also observed in (d). A speculated growth mechanism was also proposed: dissolved Sb atoms inside In droplets diffused to the interface between In and CdTe, where InSb

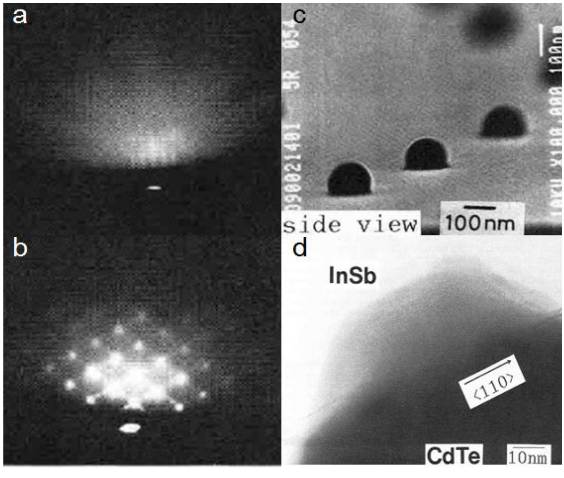

Fig. 2.3 : RHEED (left panels) and HRSEM (right panels) images of InSb growth by DE, just after the deposition of In (panels a,c) and after the irradiation with Sb (panels b,d). From Ref. [36].

was crystallized epitaxially. It is worth mentioning that these two materials nearly have the same lattice constant and therefore the application of the S-K growth mode for the fabrication of 3D nanocrystals would be impossible. This is a key feature of the DE method, that, not relying on strain, allows for the fabrication of 3D nanocrystals on both lattice-matched and lattice-mismatched systems.

Even though in the first publication about DE, an In-containing composite semiconductor was grown, the method can be also applied to other systems, as demonstrated around two years later, in a second publication[37]. In this case, Koguchi and Ishige fabricated GaAs nanostructures on S-terminated GaAs substrate by DE, exploiting the formation of Ga droplets. Importantly, variations in the RHEED intensities were followed during Ga and As supply at 200°C for the formation and crystallization of droplets, respectively. S-terminated was chosen in order to avoid the lateral growth of GaAs on GaAs and to favour the 3D development of the GaAs nanocrystal. Preventing such kind of lateral diffusion from the droplets towards the

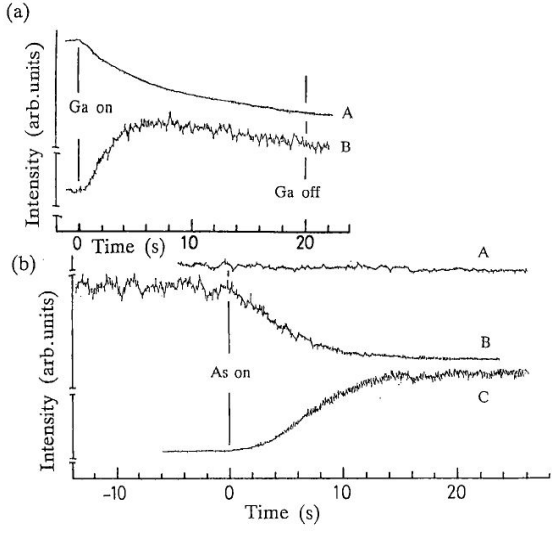

Fig. 2.4 : The variations in the RHEED intensities during Ga deposition (a) and As molecular beam irradiation (b) on S-terminated GaAs substrate at 200°C. Specular beam (A), halo (B) and (004) transmission spot (C) were traced. From Ref. [37].

substrate is another key point in DE, as will be discussed later. In Fig. 2.4 we show the results of the RHEED intensity investigations for specular beam (line A), halo (line B) and (004) transmission spot (line C). The halo signal increased just after Ga shutter opening, meaning that Ga droplets were immediately formed, and slightly decreased its intensity caused by the absorption of the electron beam by the enlarging droplets. Furthermore as soon as As was supplied, the signal from (004) transmission spot increased and simultaneously the halo decreased, which is a clear evidence for the transformation of Ga droplets into GaAs nanocrystals.

These two papers, published in the early Nineties, contain the concept and the potential of DE, as a method for the fabrication of III-V quantum confined systems. Since that time, continuous improvements brought this technique to occupy a relevant place amongst the semiconductor nanostructures fabrication methods. In the next sections we will briefly review some of the key papers for the development of DE until 2010.

2.3 Development of DE: morphology

One of the main advantages of DE respect to other fabrication techniques is the possibility to realize quantum nanostructures with different shapes. In the most standard application of the S-K growth mode for the formation of self-assembled nanocrystals, the normally obtained shape is pyramidal-like, with a faceting which depends on the materials and on the growth conditions[38]. On the contrary, in DE, very different nanostructure morphologies are accessible through simple changes in the growth parameters. Apart from the interest in the fundamental studies, this also has important practical consequences, since for quantum confined systems the shape is a fundamental parameter, because it determines the actual electronic properties of a nanostructure[39]. For instance, electrons and holes behave in different ways if they are confined in a

pyramidal-like or in a ring-like geometry. An example of the freedom in the shape design given by DE, which also clarifies, in a qualitative way, the effect of the growth conditions on the obtained nanostructures is shown in Fig. 2.5, taken from a paper by Watanabe et al.[40]. The authors present a systematic study on the formation of GaAs/AlGaAs quantum nanostructures, grown by DE. In this set of samples, Ga droplets were always formed in identical conditions at 200°C (sample a) and then the crystallization was achieved, following four different procedures: $4x10^{-7}$ Torr at 200°C (sample b), $4x10^{-5}$ Torr at 200°C (sample c), $4x10^{-5}$ Torr at 150°C (sample d) and $4x10^{-7}$ Torr at 150°C (sample e). In column (a) of Fig. 2.5, RHEED pattern (halo) and HRSEM image of the sample surface just after the Ga deposition demonstrated the formation of numerous, nanometre-sized, nearly hemispherical droplets. As clearly shown in columns (b-e), the conditions for the crystallization induced by the As supply are crucial for the realization of the GaAs quantum nanostructures. Indeed, in the case of lower As flux (b and e), it was not possible to obtain any 3D

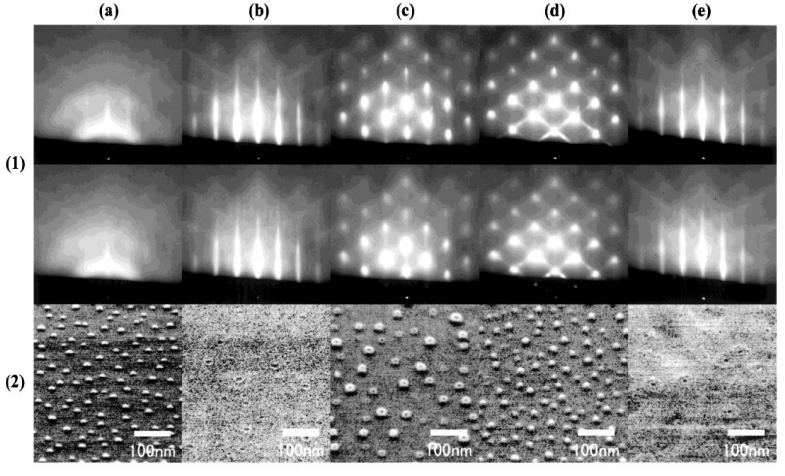

Fig. 2.5 : RHEED patterns (1) and HRSEM images (2) of the presented samples. In the upper row the electron beam was along [110] and in the lower row was along [1-10]. Column (a): after the Ga deposition; Column (b), (c), (d) and (e) : after As_4 irradiation with $4x10^{-7}$ Torr at 200°C, $4x10^{-5}$ Torr at 200°C, $4x10^{-5}$ Torr at 150°C and $4x10^{-7}$ Torr at 150°C, respectively. From Ref. [40].

growth, caused by the annihilation of droplets, similar to the cases at higher temperatures, as already mentioned in section 2.1. RHEED pattern turned to streaky, meaning that the growth predominantly proceeded in two-dimensions. On the contrary, three-dimensional growth was observed by irradiation with a higher As flux (c and d), as a result of a direct incorporation of arsenic atoms inside the Ga droplet. Under these conditions the 2D growth was restrained due to this increased consumption of Ga atoms in the droplets. RHEED pattern became spotty during the crystallization process, because of the diffraction from 3D crystals. Furthermore, the HRSEM investigations, clearly showed that for higher As flux and higher temperature (column c) the obtained GaAs nanocrystals were ring shaped (Quantum Rings), while for lower temperature they were pyramidal shaped (Quantum Dots). In the first case, the lateral migration of Ga atoms was therefore not completely suppressed and in these conditions a holed nanostructure with good rotational symmetry could be successfully fabricated. Taking into account these experimental results, as the authors stated: *"not only the As diffusion in the droplets, but also the Ga migration from the droplets are important for the shape derivation"*.

With the DE is therefore possible to achieve the fabrication of 3D nanostructures with different shapes and, exploring the growth conditions space, Mano et al. reported, for the first time, on the self-assembly of GaAs/AlGaAs Concentric Quantum Double Rings (CQDRs)[41]. The fabrication of this new type of semiconductor quantum nanostructure represents a peculiarity for the DE method. Indeed the MBE based formation of single quantum rings has also been achieved based on the standard S-K growth mode[42,43]. In this case, firstly InAs/GaAs QDs are formed and then, through a partial capping and annealing procedure, the central part of the dot is efficiently removed, thanks to the high intermixing between In and Ga. This method leaves a holed structure, which shows the typical features of quantum ring systems[44-46]. As already mentioned, DE offers more freedom for the nanostructure shape design compared to S-K and the fabrication of CQDRs is a clear example of this concept.

So far, the self-assembly of these kind of multiple concentric nanostructures has never been obtained based on the S-K growth mode. The realization of CQDRs, which showed a good rotational symmetry, with a small degree of anisotropy, was obtained by simply lowering the As flux used for the crystallization, compared to the case of single rings. Fig. 2.6 shows the line profile and the magnified AFM image of a Ga droplet (a), a single ring (b) and CQDR (c). The morphological analysis demonstrated that the diameters of the original droplets, single rings and inner ring of CQDR were nearly the same, while the outer ring in the latter structure had a larger diameter. These findings suggested that a very efficient crystallization occurred at the droplet boundaries and that the migration of Ga atoms away from the droplet played an important role in determining the shape of the GaAs nanocrystal. This interpretation is supported by the fact that the outer ring diameter increased with decreasing As flux intensity,

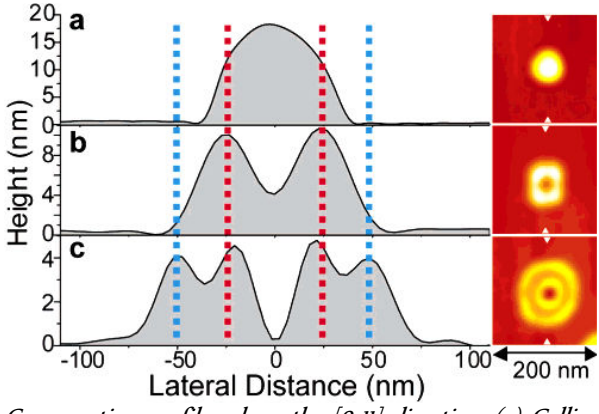

Fig. 2.6 : Cross-section profiles along the [0-11] direction. (a) Gallium droplet, formed using a supply of a 3.75 ML of Ga to the surface of $Al_{0.3}Ga_{0.7}As$ barrier layer at 350°C. (b) GaAs single ring, obtained using a supply of As flux with intensity of $8x10^{-6}$ Torr to the Ga droplets at 200°C. (c) GaAs concentric double rings, formed using a supply of As flux with intensity of $2x10^{-6}$ Torr at 200°C. From Ref. [41].

whereas that of the inner ring remained almost unchanged.

As demonstrated in a paper by Yamagiwa et. al.[47], another important GaAs/AlGaAs system can be fabricated by DE: a quantum dot molecule. Exploiting the anisotropic surface diffusion of Ga atoms

on GaAs (001) surface, the authors could obtain a double divided quantum dot, which can be considered as a molecule. This kind of system is very promising for investigating the interaction between wave functions localized in different dots, that are self-assembled in close spatial proximity and for the field of quantum computing[48]. Even if the MBE fabrication of quantum dot molecules is not a peculiarity for DE, since it has been obtained, for example, exploiting the strain-driven vertical alignment of InAs/GaAs quantum dots[49,50], it is worth mentioning that in this case, the two quantum dots are horizontally aligned, since they lie on the same plane. Later on another group applied the DE technique in order to form a similar GaAs/AlGaAs nanostructure[51], where the GaAs quantum dot molecule is sitting on a GaAs plate. In the latter case the high temperature

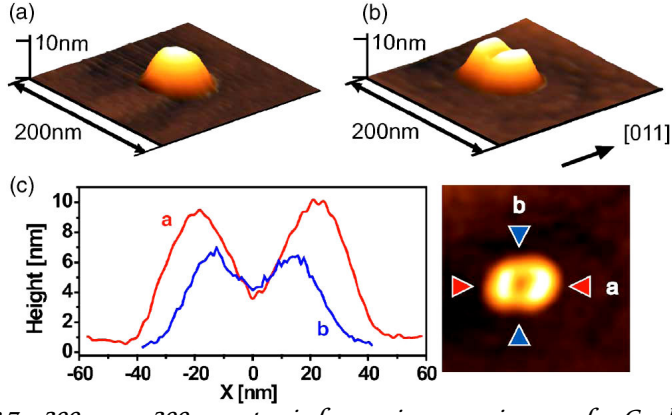

Fig. 2.7 : 200 nm x 200 nm atomic force microscope images of a Ga droplet (a) and of a GaAs quantum dot molecule (b). The line profile taken along the [0-11] and [011] directions are labelled by a and b, respectively are shown in (c). From Ref. [47].

(around 550°C) promoted the migration of Ga from the droplet and might increase the crystal quality of the grown structures.

More recently Wang et al. proposed the use of DE-grown nanostructures, in particular, homoepitaxial GaAs nanomounds[52] and nanoholes[53], as self-organized nanotemplates. In the first case GaAs large mounds were fabricated at high temperature (Ga deposition was carried out at 500°C) and, after achieving the crystallization at 150°C,

InAs depositions of different amounts was performed again at 500°C. Fig. 2.8 (a-i) shows the morphological evolution of the samples, by increasing the InAs coverage from 0 ML to 2.4 ML. GaAs mounds were transformed into bi-QD molecules, to hexa-QD molecules, and finally into the elongated nanostructures. The original GaAs mound was nearly rounded in shape, while, due to surface anisotropy of the GaAs (100) surface, the deposited InAs tended to mix with GaAs along the [01-1] and [0-11] directions. This process led to the emergence of the shoulders in (b) and the formation of a bi-QDM along [01-1], as seen in (c). With additional InAs deposition, the InGaAs QDs in the bi-QD molecules increased in size and in surface strain. Finally, one QD in the bi-QD molecule split into two, forming tri-QD molecule, as seen in (d) and when both QDs molecule split, a quad-QD molecule was observed, as in (e). Some additional InAs deposition built up as shoulders along [011] and [0-1-1] in the quad-molecule, as shown (e). When one shoulder developed into a QD, the quad-QD molecule became a penta-QD molecule, as in (f) and if both shoulders

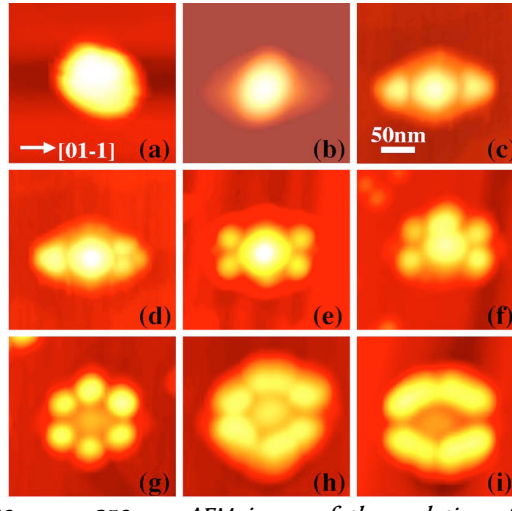

Fig. 2.8 : 250 nm x 250 nm AFM image of the evolution of the InAs QD molecules grown on the GaAs mounds: (a) GaAs mound, (b) InAs shoulder, (c) bi-, (d) tri-, (e) quad-, (f) penta-, (g) hexa-molecules, and (h) a large hexa-QDM, and (i) a molecule with elongated nanostructures. InAs monolayer coverages associated with the acquisition of sample figures were as follows: (a) 0 ML, (b) 0.8 ML, (c) 1.4 ML, (d) and (e) 1.6 ML, (f) and (g) 2.0 ML, and (h) and (i) 2.4 ML. From Ref. [52].

developed into QDs, the hexa-QD molecule was formed, as in (g). Continued InAs deposition encouraged the QDs in the hexa-molecule to further increase in size, as shown in (h), until, finally, they formed the elongated nanostructures, as in (i). A certain degree of intermixing for the strain reduction was expected in the QDs and indeed confirmed by PL investigations. Similar results were also obtained in a later publication[54].

In the case of the nanoholes, large Ga droplets were fabricated supplying 20 MLs at 500°C and subsequently annealed under As flux at the same deposition temperature. This procedure promoted the formation of nanoholes with a depth of few nanometres, as well as the growth of GaAs lobes which surrounded the nanoholes, probably coming from the crystallization of the droplet edges. The authors proposed this technology as an easy and flexible method to fabricate nanoholes template on GaAs (100) surface, with a huge potential for controlling the formation site of QDs and QDs molecules.

Indeed, after this proposal, other groups followed this idea and obtained the localized growth of both InAs and GaAs QDs inside the nanoholes. A previous paper by Kim and Koguchi[55] had already introduced the concept of nanohole as a template for the growth of InAs QDs, but on that case the nanoholes were formed *ex-situ* by AFM tip-induced nano-oxidation, followed by the DE growth of InAs. In a more recent paper by Alonso-Gonzalez et al.[56], nanoholes were formed in the same conditions as described above and then 1.4 MLs of InAs were deposited at 510°C, in order to form QDs. Figure 2.9 shows AFM images of the uncapped sample surface, at the end of the experiment. A profile along the nanostructure long axis revealed two different kinds of QDs labelled as A and B in the same figure. The differences are better observed on Figs. 2.9 (b) and (c), where typical images, obtained on a smaller area and the corresponding [1–10] profiles respectively of type-A and type-B nanostructures are depicted. In order to obtain the real dimensions of the InAs QDs, the profiles were compared with those obtained by averaging a large number of nanoholes from the reference sample, drawn as grey profiles in (b) and (c). Type-A QDs were h_1 = 9.0±1.8 nm high before capping, as

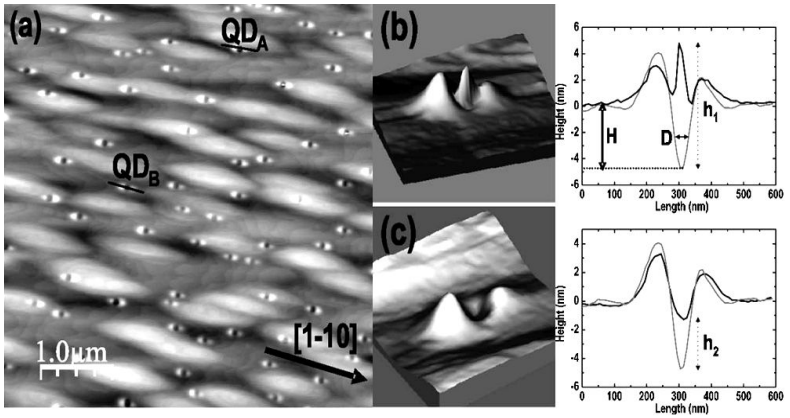

Fig. 2.9 : AFM micrographs obtained in different areas of the sample are shown in (a) 5 μm x 5 μm and (b), (c) 600 nm x 600 nm. At the right, together with the typical QD profiles, a grey line has been drawn corresponding to the average profile of the GaAs nanoholes before InAs deposition. From Ref. [56].

measured from the bottom of the seeding nanohole. They were less frequent in the ensemble and appeared with a density of $1x10^7$ cm^{-2}. On the other hand, type-B QDs did not present the same topography as they did not protrude from its nanohole. Following the same procedure, their height was estimated to be h_2 = 3.3±0.8 nm. In this case, the density obtained for type-B QDs was $2.4x10^8$ cm^{-2}. The authors pointed out that there were no QDs in the regions in between the nanoholes, meaning that the employed growth conditions were optimal for the selective formation of InAs QDs on patterned substrates.

The creation of nanoholes on AlGaAs and AlAs layers was also demonstrated[57,58] and this findings opened the route for the fabrication of another type of QD system based on the use of nanoholes as templates. Indeed, after the formation of nanoholes on AlGaAs or AlAs substrates, materials that will act as barriers for carriers, GaAs deposition can be carried out in order to fill the centre of the nanoholes with this lower band-gap material. In this way high quality GaAs/Al(Ga)As QDs were fabricated, as recently demonstrated by Heyn et al.[59,60]. A sort of mixture of the nanoholes and

nanomounds approaches, where InAs QDs were firstly formed at the centre of nanoholes, then buried with GaAs, originating nanomounds, on the top of which, InAs QDs were finally grown and localized, was also reported in a recent publication[61].

For the sake of completeness it should be mentioned that many other works have been published on the fabrication of InAs quantum nanostructures by DE, by directly forming In droplets on GaAs (001) substrate[62-65] and that recently the DE method is gaining a lot of attention by many research groups all over the world. Some publication, where DE was employed in different systems, compared to the more typical GaAs/AlGaAs and InAs/GaAs, already appeared in the latest years and, recently, this method was also used in Metalorganic Vapour Phase Epitaxy (MOVPE) growth, confirming that DE can also have a future for the large scale industrial implementation. In addition to the already cited freedom in the nanostructures shape design and to the possibility of fabricating semiconductor quantum systems in both lattice-matched and lattice-mismatched materials, DE-grown structures showed excellent optical properties, which makes them good candidates for the new generation of optoelectronic devices and for quantum information technology. We will now quickly present some of these important properties, focusing on the GaAs/AlGaAs system, that was studied in this work.

2.4 Development of DE: optical properties

In this section we will present some of the most important optical features of the DE grown nanostructures, as investigated by means of photoluminescence (PL). For the application of these systems in the fields of optoelectronics, a high quality of the material is fundamental, in order to have an optimum interaction between the light and the photogenerated carriers (light harvesting) and between the optically or electrically injected carriers and their recombination (light emission). Intrinsic or extrinsic defects in the material will both

strongly reduce its optical quality, raising the effect of non-radiative recombination channels, which have a detrimental impact on the device performances.

In DE, the MBE fabrication of GaAs nanostructures is performed at much lower temperatures compared to the standard thin film growth (500°C-600°C). A consequence of this low temperature crystallization of III-column element droplets into III-V nanostructures is the normally poor quality of the material, especially in the case of quantum dots. Indeed for the fabrication of this 3D confined systems, the temperature involved in the process of arsenization is around 200°C or lower. In order to recover the crystalline quality of the QD samples, a post-growth annealing procedure has been proposed[66]. In Fig. 2.10 the dependence of the PL intensity at 20 K on the annealing temperature of a GaAs/$Al_{0.3}Ga_{0.7}As$ QD sample is shown. The post-growth treatment was performed in the MBE chamber under As irradiation, for the same time duration of one hour, in every sample. The intensity after the annealing was drastically improved and was enhanced by around two orders of magnitude after the anneling at 760°C. This observation represented a clear evidence of the improvement of the crystal quality of the material, after a high temperature treatment. The peak position was found to shift towards higher energies, as the annealing temperature was increased and this effect was explained in terms of a reduction in the actual QD size, caused by Ga-Al interdiffusion at high

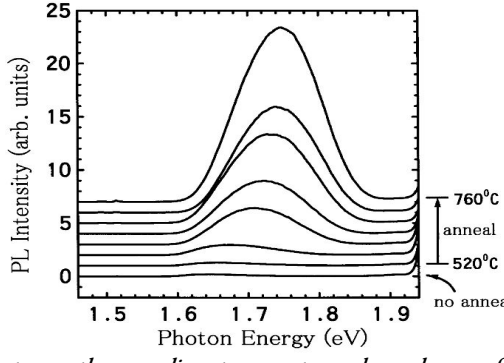

Fig. 2.10 : Post-growth annealing temperature dependence of PL spectra in GaAs/AlGaAs QDs, measured at 20 K. From Ref. [66].

temperature[67]. In fact, the high concentration of defects in the original material, together with the high annealing temperature might promote an interdiffusion of III-column elements, up to around 2 nm[68], that lowered the dimensions of the QDs, which in turn will emit at higher energies. Post-growth annealing can also be performed outside of the MBE chamber, where the high temperatures involved might affect the machine lifetime, by using a rapid thermal annealing (RTA). In this case, the samples are loaded in a small furnace with a controlled, inert atmosphere (nitrogen) and heated rapidly, with a typical rate of 200°C/min[69]. The effects of the RTA were found to be very similar to the former annealing procedure, leading to an increase of the PL yield, saturating after 750°C, as well as a shift in the PL peak.

An important parameter for the fundamental and practical studies involving QDs is the Fine Structure Splitting (FSS), a degeneracy lift of the bright excitonic states, induced by asymmetries in the confining potential[70]. In absence of FSS, the radiative decay from biexciton, to exciton and to the ground state should lead to the emission of polarization-entangled photon pairs, promising in the field of quantum information[71]. Typically of the order of tenth of μeV, FSS values are very different, depending on the system and growth method. A variety of phenomena contribute to the asymmetry in the confinement potential, such as crystal symmetry, strain, composition, shape, piezoelectricity and it is normally difficult to distinguish between different effects. However, the GaAs/AlGaAs QDs system, grown by DE, has a lot of advantages, due to the lack of strain and intermixing. FSS has been investigated by means of high resolution, polarization-dependent PL on single QDs[72]. A typical μ-PL spectrum of a single GaAs QD is shown in Fig. 2.11 (a). At 1.5 mW two lines labeled X and T were observed. With increasing power to 15 mW, another line labelled XX emerged on the lower-energy side. The power dependence of lines X, T, and XX is presented in Fig. 2.11 (b); for each line the intensity increased with power, until it reached maximum and then started to quench. A fit of the experimental data to a power law indicated a superlinear behaviour for both T and XX; it is worth

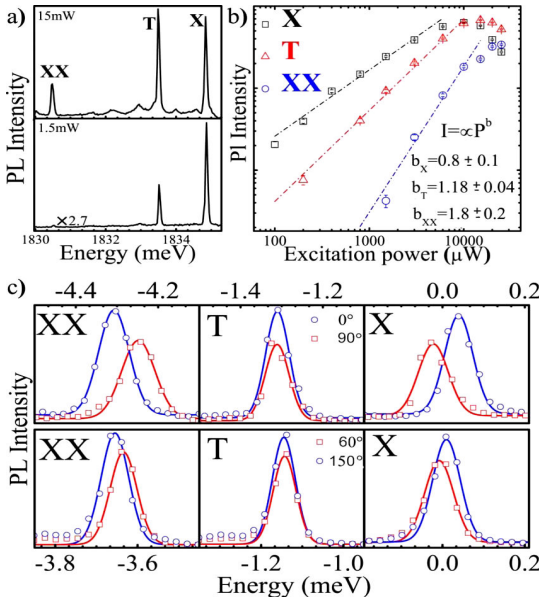

Fig. 2.11 : PL spectrum of a single GaAs/AlGaAs QD at two excitation powers. The three lines X, T, and XX are interpreted as neutral exciton, trion, and biexciton emissions (a). Power dependence of lines X, T, and XX (b). Dashed lines show fits of the data to a power law, I ~ P ^{b}. Polarized PL spectra of two different QDs (c). The top panel refers to the QD of (a). Blue circlesand red squares indicate the spectra of two orthogonal polarizations of which relative angle is shown in the legend. Lines are Gaussian fits. The horizontal axis is shifted by the energy of X (1834.9 and 1875.7 meV for top and bottom panels, respectively). From Ref. [72].

noting that XX increased almost quadratically with respect to X. These emission lines X, T, and XX were interpreted as the neutral exciton, trion, and biexciton radiative recombinations, respectively. The linewidths were found to vary between tens to hundreds of microelectronvolts, reflecting spectral diffusion due to the presence of charged defects in the QD environment. In Fig. 2.11 (c) the orthogonally polarized PL spectra of two different QDs is reported. A mirror-symmetric fine structure was evidenced for X and XX, while no splitting is observed for T, being consistent with the attribution of these lines. The measured FSS Δ, defined as the maximum splitting of

two orthogonally polarized lines were Δ_X = 62 meV and Δ_{XX} = 60 meV (top panel), and Δ_X = 18 meV and Δ_{XX} = 20 meV (bottom panel) with an error of ±5 meV. As could be expected, it was found that $\Delta_X = \Delta_{XX}$, within the experimental error. FSSs obtained from measurement on several QDs are plotted as a function of the emission energy in Fig. 2.12 (c). Spanning an interval of around 200 μeV, the FSS Δ was found to clearly monotonically decrease, by increasing the X energy. When the X line was at low energy, the FSS value was approximately 90 μeV, while for smaller QDs corresponding to emission at 1.89 eV the FSS reached around 18 μeV. Even though similar values and behaviour were found in S-K InAs/GaAs QDs[73], in this case, the absence of strain, permitted to attribute the reduction of FSS at higher emission energies to the geometry of QDs. As shown in the top panel of Fig. 2.12, smaller dots had a lower degree of anisotropy, compared to the bigger ones, which were elongated along [1-10] direction. Therefore, the small dots, emitting at higher energies possessed a lower FSS. The possibility of reducing the FSS simply governing the QD shape, which

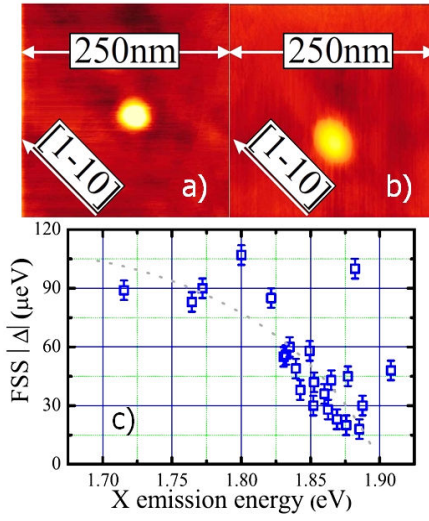

Fig. 2.12 : AFM images of a small QD with h = 3.9 nm (a) and large QD h = 11.8 nm (b). Fine structure splitting of QDs emitting at different energy. The reported values are the average value of FSS for X and XX .The dotted line is a guide to eye. Modified from Ref. [72].

is a relatively easy task in DE, makes these nanostructures promising for the application in the field of quantum computing, as recently investigated also for the InGaAs/GaAs system[74].

A second crucial issue in QDs optical studies is the generation of single photons. Obtaining a controlled emission of a single photon from a nanostructure is another important step in view of the development of a quantum information technology. Photon correlation and cross-correlation measurement have been performed on GaAs/AlGaAs QDs grown by DE with a Hanbury–Brown–Twiss setup at 6 K[75]. The results are shown in Fig. 2.13. In (a) time-integrated PL spectra for various excitation intensities of the single QD are shown. At low excitation, below 10 W/cm^2, a single line, referred to as X, appeared at 667 nm (1.861 eV). This line was assigned by recombination of neutral excitons. Its linewidth is 0.45 meV in full width at half maximum (FWHM), being limited by instrumental resolution. With increasing excitation intensity, several spectral components manifested themselves on the lower energy side of line X, in particular, two bright lines referred to as A and B. The energy split between X and A was 1.1 meV, and that between X and B was 3.4 meV. Excitation density dependence of the emission peaks are plotted in (b). All peaks increased with excitation density until they reached their saturation levels at around 15 W/cm^2. The dependence of peak X could fit to a power law with the exponent of 1.7, much larger than unity. Such a nonlinear dependence may reflect a high density of trapping centers present in the barrier layer of the sample. The exponents of a power-law for lines A and B were evaluated as 3.4 and 3.6, respectively, thus nearly twice of X, suggesting that the formation of a biexciton should appear in the emission of A and/or B. A second-order autocorrelation function for the X emission is shown in (c), where the number of coincidence events, measured at 10 W/cm^2, are summarized in the histogram. The periodic peaks appearing at regular intervals indicated that photons were emitted synchronously with pulsed excitation. The lack of a peak at zero time delay indicates that there was almost no probability of finding two or more photons inside each emitted pulse. The results of cross-correlation measurement between

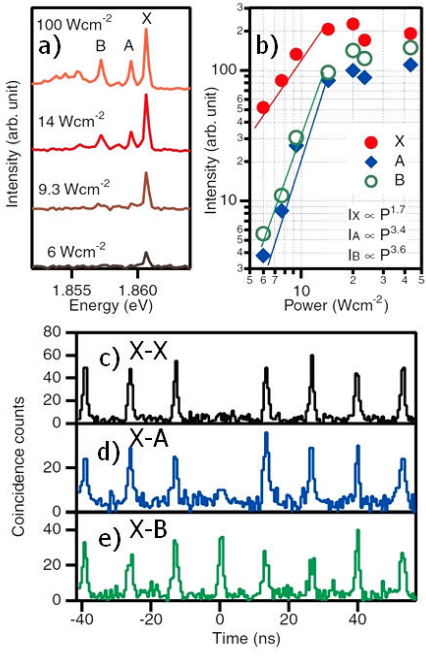

Fig. 2.13 : PL spectra of a single GaAs quantum dot at various excitation density (a). Time integrated intensity as a function of excitation power for the three lines identified by X, A, and B (b). Second-order correlation functions of light emitted from a single GaAs QD with pulsed excitation of 76.0 MHz repetition for peak X is shown in (c), and those of the cross-correlation between X and A, and between X and B, are shown in (d) and (e), respectively. Modified from Ref. [75].

peaks X and A are presented in (d), and those between peaks X and B are shown in (e). The excitation power in these measurements was increased to 50 W/cm², in order to obtain high counting rates for peaks A and B. The X–A correlation showed a lack of the zero-time peak, similar to the X–X autocorrelation, while the X–B correlation showed the emergence of a zerotime peak. The observation of an antibunching feature in the X–A correlation demonstrated that the A and X photons were not emitted simultaneously. This may be attributable to line A having originated from a recombination of charged excitons and line X from neutral excitons. As a result, either the X photon or the A photon was generated during a single emission cycle, leading to the observation of the antibunching dip. On the

contrary the emergence of the zero-time peak in the X–B correlation suggested that line B was originated from biexcitons. Indeed when a biexciton is inside a QD, the first photon is emitted at the biexciton energy, then the second photon is emitted at the single exciton energy. From these measurements it was therefore possible to confirm GaAs/AlGaAs QDs grown by DE, as good single photon emitters. Additional investigations on the magneto-PL[76] and on the nature of the line broadening[77] in these type of system have also been performed.

Quantum rings have also been extensively studied because of their special topology. The quantum interference effects[78-82] which might arise in these systems attracted a lot of attention in the scientific community. By the use of the DE technique, the fabrication of single and double quantum rings in the GaAs/AlGaAs system has been shown, opening the possibility for optical investigations on these systems characterized by rotational symmetry. Single rings and concentric quantum rings (CQR) have been studied by means of broad area and micro-PL[83]. More interestingly, the case of CQR was subject of deeper investigations; we report some of the main results in Fig. 2.14. In (a) the AFM image and cross sectional height profile, fitted with Gaussians, of a typical CQR is shown, with a diameter of 40 nm and 90 nm for inner ring (IR) and outer ring (OR), respectively. In (b) the micro-PL emission of a single CQR at increasing excitation power is reported, showing a double peak, which can be attributed to the emission from OR (lower energy) and IR (higher energy), on the basis of theoretical calculations[83]. The OR emission at high excitation power showed multiple peaks (L1, L2), indicating the recombination of multiexcitonic complexes from its ground state, similarly to what found in QDs. Additionally, time resolved PL of the same system confirmed the completely uncoupled dynamics of carrier recombinations inside the two rings, despite their close spatial proximity[84]. This lack of resonance between carriers localized on different rings can be caused by the strong suppression of charge tunnelling between states of different angular momentum, due to the selection rules.

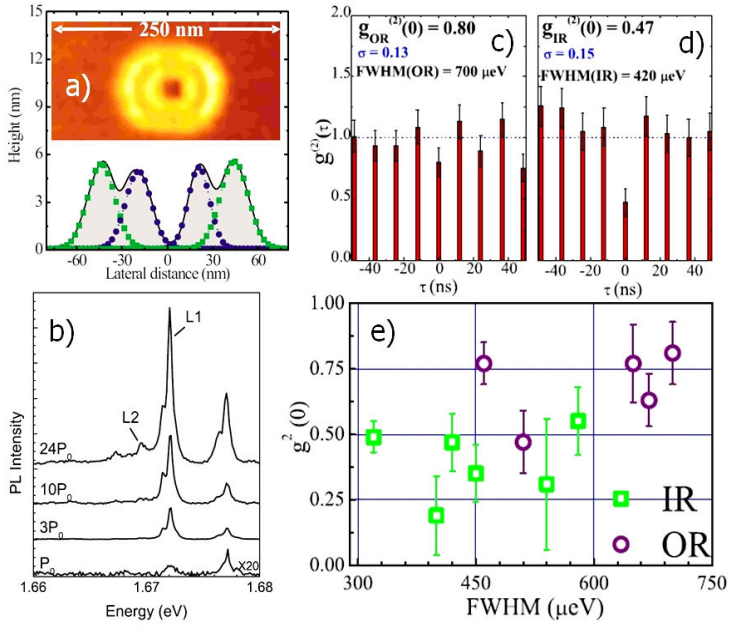

Fig. 2.14 : Typical AFM image of a GaAs CQR (top panel) and cross section height profile (bottom panel) (a). The squares and the circles represent the Gaussian fit to the section profiles of the outer and inner rings, respectively. Time integrated spectra of CQR at different excitation power densities at T = 10 K and P_0 = 3 W/cm² (b). Pulsed excitation measurement of $g^{(2)}$ for OR (c) and IR (d). The error bar associated to each peak is the coincidence count square root normalized to the average value of the peaks intensity. σ is the standard deviation of the average value of the peak intensity except for the zero-delay. Summary of all the measured $g^{(2)}(0)$ for IR (squares) and OR (circles); the error bars are the measured standard deviation. Modified from Ref. [84] and [85].

Second-order correlation measurements have also been performed, to investigate weather the emission from OR and IR satisfy the requirement of a single photon source[85]. In Fig. 2.14 (c-e) the results of these experiments are shown, demonstrating that IR exhibited antibunching features and was found to generate single photons. On the contrary, OR was not capable of the same type of emission. The differences were explained in terms of the dimensions of the rings, where the OR, being larger than the IR, could be more influenced by structural disorder, around the nanostructure. The

results obtained also in the case of quantum rings grown by DE demonstrated that, in general, these systems can be considered as promising for a wide range of fundamental and practical investigations.

As already mentioned before, the crystal quality of the as-grown quantum nanostructures might be quite poor, due to the low temperatures involved in DE. Performing an high temperature annealing, without capping the GaAs structures, would result in a not desirable change of their shape, therefore a low temperature capping is inevitable to protect the nanocrystals. However, the low temperature growth of AlGaAs might again introduces a lot of defects inside the barrier, even if performed by the Migration Enhanced Epitaxy (MEE) method[86,87]. This structural disorder in the barrier might affect the emission from the nanostructures, creating charge defects in their close proximity. Recently, Mano et al.[88] proposed a modification to the standard capping procedure in order to improve the quality of the material. In this case the MBE growth of the barrier was started after performing an annealing at 400°C without capping, in order to remove the excess amount of As on the surface. This annealing only slightly modified the structural properties of the DE GaAs QDs. With this procedure, very sharp peaks appeared in the single structure PL spectra, with an excitonic emission of around 30 μeV. Similar linewidths have also been obtained, by filling of nanoholes, fabricated by DE[60], demonstrating once again the high optical quality of these nanostructures.

2.5 DE application to devices

Due to the excellent properties of the DE-grown nanostructures, in the past few years, the realization of some device has been proposed, based on these systems. GaAs single quantum rings, have been employed as active elements in a lasing structure[89]. In this case, three stacks of GaAs/AlGaAs quantum rings have been

fabricated and optically pumped for the lasing experiments. The most important characteristic of the laser are reported in Fig. 2.15. In (a) the emission spectra taken from the cleaved edge of the laser structure for various excitation powers at 77 K are shown. At low excitation, below 8 mW, the spectrum is dominated by a smooth and broad curve, corresponding to spontaneous emissions from the QD ensemble. When the excitation power was increased to 12 mW, the spectra changed into an ensemble of sharp, resolution limited lines, reflecting multimodal stimulated emissions of QDs. Since the centre energy of the line ensemble is 747 nm, which agreed with that of spontaneous emissions, it was suggested that that stimulated emissions originated from the ground state of the rings. The inset demonstrates an expanded view of the multimodal laser spectrum. A plot of the dependence of emission intensity on excitation power is shown in (b). The intensity was evaluated by the spectral integration of emission signals. A clear threshold that means the onset of lasing could be clearly detected. The temperature dependence of the lasing

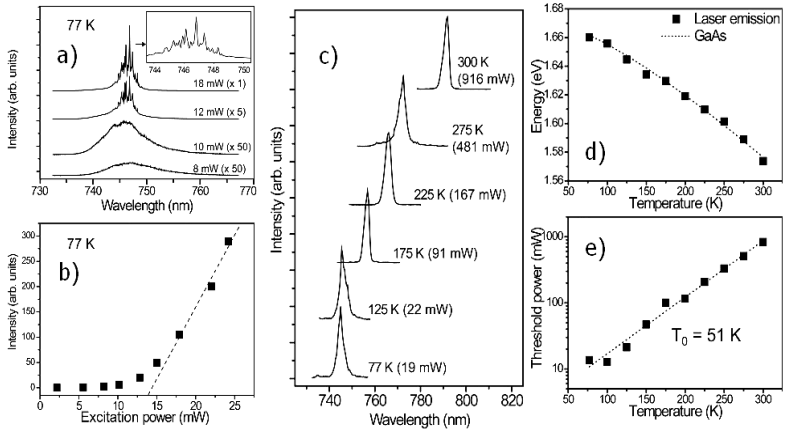

Fig. 2.15 : Emission spectra taken at various excitation powers 8, 10, 12, and 18 mW at 77 K. The inset shows a magnified spectrum at 18 mW (a). Integrated emission intensities at 77 K as a function of the excitation power (b). Lasing spectra at 77, 125, 175, 225, 275, and 300 K (c). Centre energy (d) and threshold power (e) of the lasing as a function of temperature. The dotted line in (d) shows the temperature dependence of the GaAs band gap energy. The dotted line in (e) shows the fit according to the characteristic temperature of 51 K. Modified from Ref. [89].

properties was also investigated to check the quality of the device. The laser emission spectra at various temperatures is plotted in (c). The spectra of laser emissions shifted to lower energy with increasing temperature. The temperature dependence of the centre energy of laser emissions, which showed a monotonic decrease with temperature is displayed in (d). It followed the GaAs band gap energy, as shown by the dotted line, thus the authors concluded that the electronic level relevant to the lasing is the ground state of the rings, irrespective of temperature, up to room temperature. Temperature dependence of threshold power is also shown in (e). Although the threshold power increased with temperature, laser action was confirmed up to room temperature, indicating the good quality of the device. Through the fit, the characteristic temperature was estimated to be T_0 = 51 K. Therefore the photopumped lasing from ring-shaped GaAs QDs grown by DE was demonstrated. The laser structure exhibited multimode laser emission from the ground state of the QDs, with a clear threshold from 77 K to room temperature.

More recently, based on DE-grown GaAs/AlGaAs nanostructures, the fabrication of multicolor photodetector[90] has been proposed. A device prototype has been realized by using CQR-like GaAs nanostructures and standard processing techniques, consisting of photolithography and chemical wet etching. In Fig. 2.16 (a) the AFM image of the uncapped sample is reported. The device photoresponse in the visible-near-infrared spectral region was measured at 77 K for different bias voltages, as shown in (b). Two broad bands appeared peaking at 0.83 and 0.65 μm. The 0.83 μm band was due to the direct interband transitions (Γ-point) in the GaAs quantum rings. This band contained a sharp peak at 0.824 μm (1.500 eV), which was due to the interband transition from the heavy hole ground state in the valence band to the electron ground state in the conduction band. The broad band observed around 0.645 μm (1.922 eV) was explained in terms of the conduction band L-minimum indirect interband transitions in the GaAs quantum rings, in good agreement with the calculated L-minimum band gap. This broad band was ruled out as being due to interband transitions within the

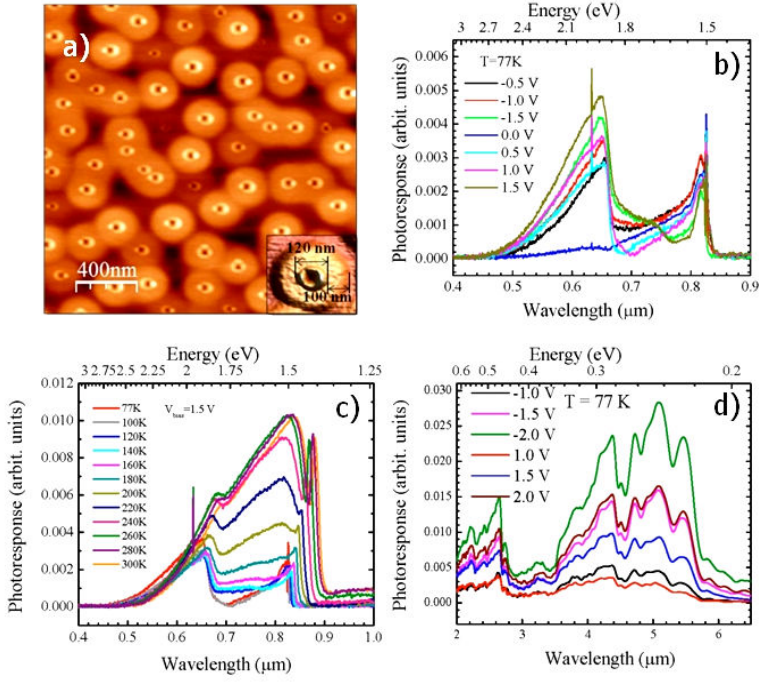

Fig. 2.16 : AFM image from an uncapped GaAs quantum ring sample. The inset is an enlargement, showing a single nanostructure (a). Several photoresponse spectra obtained for GaAs/AlGaAs quantum rings device and measured at 77 K for different bias voltages. The spectra were due to interband transitions (b). Photoresponse spectra of the device measured at different temperatures for a bias voltage of 1.5 V. The spectra were due to interband transitions (c). Midinfrared photoresponse spectra measured at 77 K for different bias voltages. These spectra were due to intersubband transitions. Modified from Ref. [90].

$Al_{0.3}Ga_{0.7}As$ barrier mainly because the band gap of this barrier with 30% Al mole fraction is on the order of 0.693 μm (1.79 eV). The sharp peak at 0.632 μm was due to the HeNe laser line used for the dynamic alignment of the spectrometer. The devices exhibited a small photovoltaic effect, as a photoresponse has been observed at zero bias voltage. Several photoresponse spectra were measured at temperatures ranging between 77 and 300 K, as shown in (c), demonstrating an increase of the photoresponse with the temperature. This behaviour was attributed to the thermally assisted direct and indirect interband

transitions. In addition to the observation of the photoresponse due to the interband transitions in the visible-near-infrared spectral region, a midinfrared photoresponse band was detected in the spectral region of 2.0–6.0 μm, as shown in (d). The spectra were measured at 77 K for different bias voltages. This band was attributed to the intersubband transitions within the conduction band of $GaAs/Al_{0.3}Ga_{0.7}As$ multiple quantum rings. The spectra contained several peaks, which were attributed to the variation in the quantum ring height. Indeed fluctuations in the quantum ring height can produce different energy separations between the quantized energy levels, leading to the several intersubband transitions with different peak positions. A photovoltaic effect was not observed in this midinfared photoresponse band. Furthermore, the photoresponse spectra were depleted when the temperature was raised above 80 K. Based on similar quantum nanostructures, the same group recently fabricated an intermediate-band solar cell[91] and another intersublevel infrared photodetector, where the active elements were quantum dot pairs, also grown by DE[92].

Summarizing, we have shown the main features of DE-grown GaAs/AlGaAs nanostructures, as investigated by means of PL spectroscopy and reported the recent fabrication of optoelectronic devices based of these system. Because of their excellent optical quality, these quantum structures can be considered as promising candidates for future developments in optoelectronics and quantum information technology.

2.6 Main features of DE

A schematic summary of the main features of the DE method, as resulted from around 20 years of investigations is presented in the following.

Structural properties:

- ✗ *Surface density* : by changing the deposition conditions, the number of nanostructures per unit area can be varied over a wide range[93].
- ✗ *Lattice-matched growth* : not relying on strain, the growth of 3D nanocrystals is possible for both lattice-(mis)matched materials.
- ✗ *Wetting layer* : the presence and even the thickness of a wetting layer underneath the nanostructures can be engineered on demand[94,95].
- ✗ *Shape control* : structures with different shapes can be fabricated ranging from dots, to single rings, concentric double rings and dot molecules.

Optical properties:

- ✗ *Annealing* : a post-growth annealing treatment is normally necessary to improve the optical quality of the samples.
- ✗ *Fine structure splitting* : a reduction to suitable values for the emission of polarization entangled photons is observed, in highly symmetrical dots.
- ✗ *Sharp emissions* : with optimized annealing and capping procedures ultra-narrow emission can be obtained.
- ✗ *Single photon emission* : QDs and inner rings in concentric double rings structures are able to emit a single photon.

Most of these features have been treated more in detail in the previous sections and some other will be extensively discussed in later chapters, including our contribution to the subject. Deeper investigations on these subjects can be found in the literature.

Chapter 3

"I've never told a lie and that makes me a liar
I've never made a bet but we gamble with desire
I've never lit a match with the intent to start a fire
but recently the flames are getting out of control"

(from "Jasey Rae" by All time low)

Experimental methods

In this section we will describe the equipments that have been used in this work. Firstly we will present the scheme of our molecular beam epitaxy system, a GEN II model by EPI and a quick overview about Reflection High Energy Electron Diffraction (RHEED) and about how to interpret the RHEED patterns. Then we will introduce the Atomic Force Microscope (AFM) instrument by which the morphological analysis was carried out and the PL setup used to optically characterized the capped samples. Finally we will briefly discuss the chemical etching procedure which allowed us to selectively remove metallic Ga, without damage for the GaAs structures.

3.1 MBE system

Every growth experiment presented in this work has been carried out in a conventional GEN II MBE system originally constructed by EPI and nowadays handled by Veeco. This apparatus is composed by three connected UHV chambers: an introduction chamber, a buffer chamber and a growth chamber, separated by gate valves. In Fig. 3.1 the plane view of our MBE system is reported.

The introduction chamber is used for the communication between the standard atmosphere and the UHV environment and is therefore the only part of the machine that is vented whenever a sample has to be inserted or extracted. This chamber is pumped by a turbomolecular pump and, after the insertion of new samples, is heated by means of quartz lamps up to 200°C in order to remove any

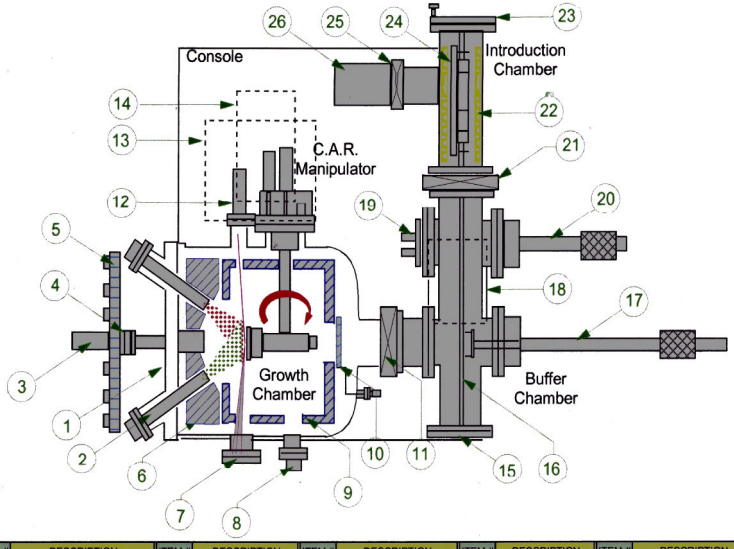

ITEM #	DESCRIPTION	ITEM #	DESCRIPTION	ITEM #	DESCRIPTION	ITEM #	DESCRIPTION	ITEM #	DESCRIPTION
1	Source Flange	6	Source Cryo-panel	11	Growth/Buff Gate Valve	16	Trolley Rail	21	Intro/Buffer Gate Valve
2	Effusion Furnaces	7	RHEED Screen	12	RHEED Source	17	CAR Transfer Arm	22	Outgas Lamps
3	Pyrometer	8	Quad Mass Analyzer	13	Ion Pump (sump)	18	Buffer Ion Pump	23	Quick-hatch Door
4	Heated Pyrometer Viewport	9	Growth Cryo-panel	14	Cryo-pump (sump)	19	Heated Station (HS)	24	Multiple-sample Trolley
5	Removable Shutter Solenoids	10	Master Shutter	15	Buffer End Viewport	20	HS Transfer Arm	25	Intro Pump Gate Valve
								26	Intro Pump (Turbo/Cryo)

Fig. 3.1 : Plane view of the EPI GEN II MBE system used in this work.

contaminants coming from the normal atmosphere. After this procedure the vacuum level inside this part of the machine reaches the 10^{-9} Torr level.

The buffer chamber is at intermediate position between the introduction and the growth chambers and contains a degas station where the wafers can be heated up to around 600°C to completely ensure the purity of the samples prior to the growth. In this area an ion pump is installed which allows the vacuum degree to be on the order of 10^{-11} Torr. The sample holders can be moved across all the length of introduction and buffer chambers thanks to the movement of a magnetic trolley. After degassing in the buffer chamber for a suitable time, the samples can be loaded to the growth chamber by a transfer rod.

The growth chamber is the most complicated and important part of an MBE machine since its features and degree of purity determine the quality of the production. In Fig 3.2 the scheme of the growth chamber is displayed, describing the key features of this part of the system. Our growth chamber is equipped with 6 effusion cells containing ultra pure materials: Al, Ga, In, Si, Be and As. For the arsenic element, a valved cracker cell is used in order to have a precise control over the molecular beam flux during growth. In our case the cracking zone temperature has always been maintained at 600°C, thus providing As_4 molecules during every experiment. The sample holders are mounted on the substrate manipulator where they can be heated up to around 1000°C and kept under rotation during the growth. On the other side of the manipulator, an ionization gauge for the beam flux measurement is installed and when the manipulator is rotated so that the gauge is exposed to the cells, an estimation of the molecular beam flux coming from the effusion cells can be obtained. A second ionization gauge and a mass spectrometer for the residual gas analysis (RGA) are mounted on the chamber for the vacuum degree level and quality monitoring. In front of the substrate holder an optical pyrometer for the substrate temperature reading is present; in this way we have a second method for determining precisely the substrate temperature, alternative to the thermocouple under the substrate

holder. Around the manipulator and around the effusion cells two cryo-shrouds are completely filled with liquid nitrogen for all the duration of the growth experiment. The vacuum degree is the most important point in MBE technology to ensure the purity of the grown materials and satisfy the condition of a mean free path for the gas molecules larger than the substrate-cells distance. During growth the substrate and the cells areas are strongly heated to reach the operating temperatures (around 600°C for the substrate and around 1000°C for the Ga cell in a standard deposition of GaAs) and this heating promotes the thermal desorption of gas molecules adsorbed onto the chamber walls. This would in turn degrade the vacuum degree in the growth chamber by several orders of magnitude. To avoid this effect, liquid nitrogen is used to bring to cryogenic temperatures the shrouds around substrate and cells, therefore creating an adsorption area for the gas molecules. In this way the UHV environment can be preserved even at the operating temperatures used for the growths. In our growth chamber are installed: an ion pump, a cryo pump and a titanium sublimation

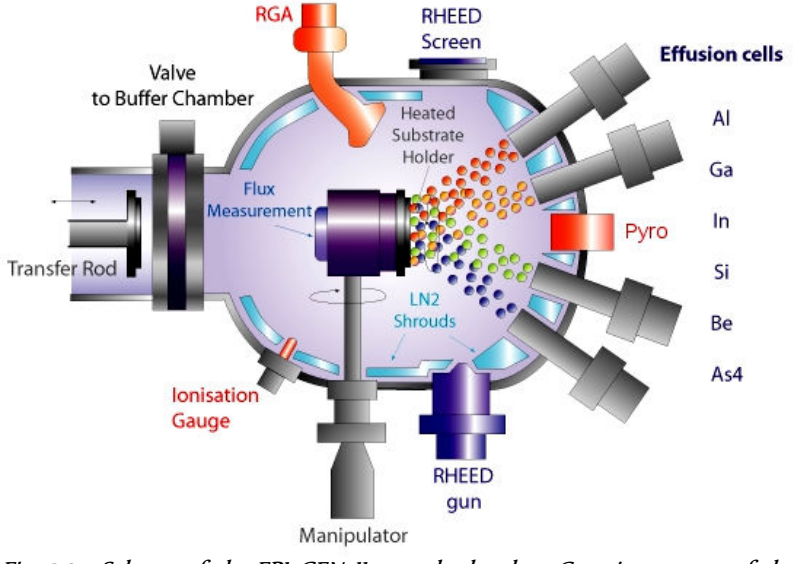

Fig. 3.2 : Scheme of the EPI GEN II growth chamber. Constituent part of the system are indicated on the picture.

pump. Thanks to the pumping and gettering effect of both vacuum pumps and liquid nitrogen, an excellent degree of 10^{-11} Torr can be obtained, which ensures the quality of the materials that can be grown with our MBE system. Finally for the *in-situ* monitoring of the surface phenomena occurring during the experiments a RHEED system is installed, composed by an electron gun and a fluorescence screen. A commercially available webcam is mounted in front of the RHEED screen in order to have the possibility of recording the pattern changes and to take advantage of the digitalization of the images. Due to its importance in MBE growth and in our work, a more detailed description of the RHEED apparatus and signal will be given in the next section.

3.2 Reflection High Energy Electron Diffraction

Reflection High-Energy Electron Diffraction (RHEED) is a versatile analytical tool for characterizing thin films during growth by molecular beam epitaxy, since it is very sensitive to surface structure and morphology. RHEED is particularly suited to this application as it does not block the direction vertical to the surface of the crystal which is observed, and is particularly sensitive to surface roughness, down to monolayer sensitivity. RHEED is based on the interaction between electrons with high kinetic energy (on the order of tenth of keV) incident at low impact angle (typically less than 5°) and the surface of a solid. In Fig. 3.3 a sketch of the origin of RHEED signal is given. Since the incoming electrons have a very small incident angle with respect to the growing surface and a high energy, they will only be scattered from the top layers of atoms of the sample. The atomic arrangement is therefore a two-dimensional array of the surface atoms and the reciprocal space image of this lattice that can be seen by a diffraction experiment is constituted by vertical lines, named reciprocal rods. Assuming elastic scattering no energy transfer is

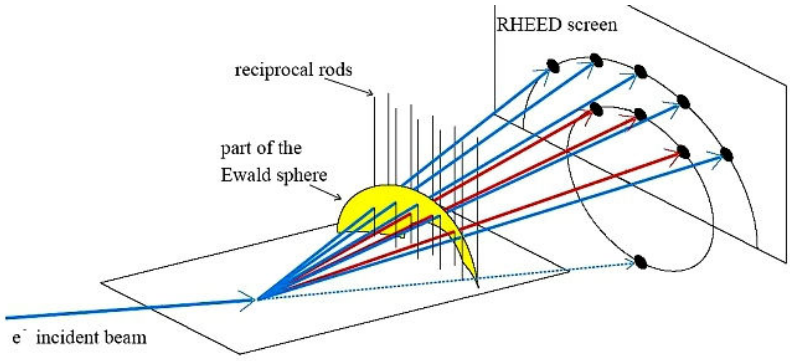

Fig. 3.3 : Three-dimensional scheme of a RHEED experiment. Electrons emitted by the electron gun strike onto the sample with a very low incident angle. The points at the crossing between the Ewald sphere and the reciprocal rods will satisfy the Bragg condition of diffraction and will be displayed on the fluorescent screen.

allowed from the electrons to the sample, so the scattered wave vector lies on the surface of the sphere of constant energy, the so-called Ewald sphere. Since the Bragg condition for diffraction is satisfied for each point lying on this sphere wherever the reciprocal rods cross the Ewald sphere, the condition for constructive interference of the elastically scattered electron beams from the surface is fulfilled. On the RHEED screen the reciprocal space map of the points satisfying the diffraction condition will be displayed, allowing the interpretation of the surface phenomena occurring during growth. Indeed by RHEED investigations it is possible to recognize different surface reconstructions, judge the atomic flatness of a sample, detect the transition to a three dimensional growth and evaluate the crystal lattice of an epilayer.

Another peculiar feature of RHEED is the periodic variation of the reflected beam intensity during growth, the so-called specular beam intensity oscillations. In Fig. 3.4 we give a simple explanation for this phenomena. Starting with the initial situation of coverage $\theta = 0$ of a perfect mirror-like surface, the reflected beam will partially lose its intensity after the initiation of the deposition, caused by the interaction of the electron beam with the growing monolayer. This decrease in the reflected beam intensity will continue until the

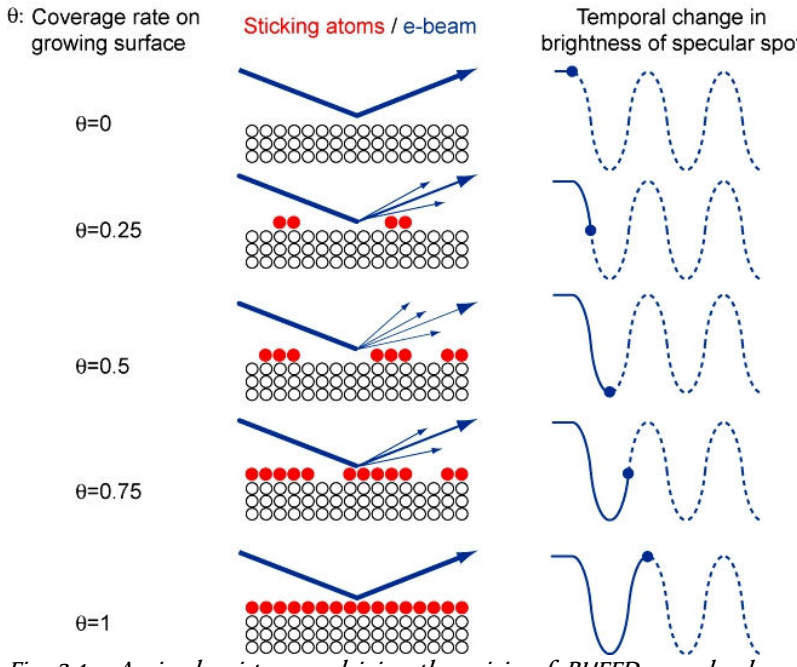

Fig. 3.4 : A simple picture explaining the origin of RHEED specular beam intensity oscillation during growth. As the coverage increases the electron beam will be scattered by the growing monolayer and the specular beam intensity will decrease. After the coverage of half a monolayer the brightness will be recovered and the intensity will show a maximum after completing one monolayer.

deposition of half a monolayer and then the RHEED specular beam signal will recover its intensity, since the analysed surface will move toward the mirror-like configuration in $\theta = 1$. At this point, a second maximum will appear, being the period of these oscillations equal to the time for the deposition of a single monolayer. This phenomenon is typical of the two-dimensional nucleation or layer-by-layer growth regime and it is used to calibrate the materials growth rate. In our work, III-column element molecular beam fluxes have been calibrated by recording the RHEED specular beam intensity change during growth. Normally, after some time, the amplitude of these oscillations is damped, caused by the increasing disorder at the growing surface and the change from the two-dimensional nucleation to the step-flow

regime. The study of the RHEED oscillations was also employed for the determination of the surface diffusion length of Ga adatoms during the growth of GaAs on vicinal surfaces, as reported in a key paper by Neave et al.[96]

3.3 Atomic Force Microscopy

An important part of this work has been devoted to the study of the influence of the growth parameters on GaAs nanostructures dimensions and shapes. It was therefore crucial to have reliable nanometre-scale images of the grown samples. A Veeco Innova atomic force microscope was used for the morphological characterization of our structures, mounting tips with a curvature radius between 2 nm – 7 nm, depending on the required scan resolution. We report in Fig. 3.5 the picture of our AFM system. For any other detail about the hardware and software, we recommend to visit the webpage of the producer of this system: http://www.veeco.com/innova-scanning-probe-

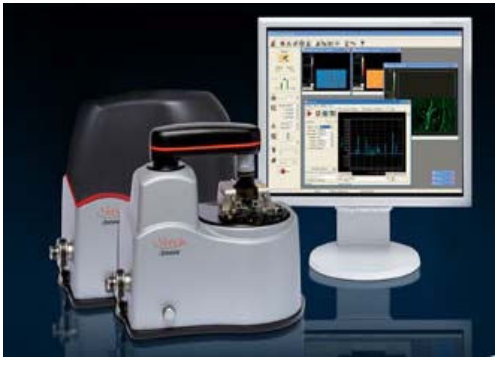

Fig. 3.5 : Picture of our Veeco Innova atomic force microscope.

microscope/index.aspx . The AFM images were then elaborated by the use of WSxM scanning probe microscopy software[97].

3.4 Photoluminescence

In order to assess the optical quality of the nanostructures fabricated in this work, it is necessary to investigate the photoluminescence (PL) properties of capped samples. Obtaining a strong PL signal from quantum confined nanostructures is a prerequisite for their application in optoelectronic devices and ensures the high quality of the grown material. We performed PL measurement in the macro-PL configuration, where the laser spot is focused on an area of hundreds of square microns. The sample is installed in a cryostat, allowing the measurements from 14 K to room temperature. The excitation source is a CW Nd:YAG green laser (λ_{exc} = 532 nm) with a maximum power density of around 0.15 kW/cm^2. The exciting laser is focused on the sample by means of an achromatic doublet, making an angle of around 45° with sample surface. The emission from the sample is then collected by four spherical mirrors, focused at the entrance of a 50 cm focal length monochromator and

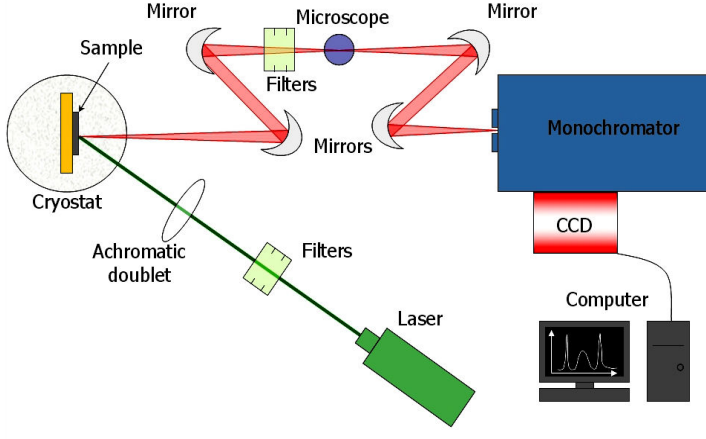

Fig. 3.6 : Sketch of the photoluminescence setup used in our experiments. The laser beam is focused on the sample by an achromatic doublet and the PL signal is dispersed by a monochromator and detected by a CCD camera.

detected by a Peltier cooled 1100x330 pixels CCD camera. The PL setup used to investigate the GaAs/AlGaAs quantum nanostructures is depicted in Fig. 3.6.

3.5 Selective etching of pure gallium

As we will comment in later sections, a very important issue in our research is to discriminate between pure metallic Ga and GaAs. As recently shown for the Ge/Si[98,99] and InAs/GaAs[100,101] systems, chemical wet etching is a powerful technique which allows the post-growth analysis of the chemical composition of self-assembled quantum nanostructures. By selectively removing only one component from a composite island (for example Ge from SiGe quantum dots) a lot can be learnt about the formation mechanism of the crystal. This idea brought us to the use of chemical etching on our GaAs nanostructures in order to investigate the presence of a GaAs embryo inside metallic Ga droplets. As etchant for this purpose 37% concentric HCl was used at room temperature, followed by a rinse in deionized water[102]. In order to check the selectivity of the etchant we studied the relative loss weight $\Delta m/m$ after the chemical treatment as

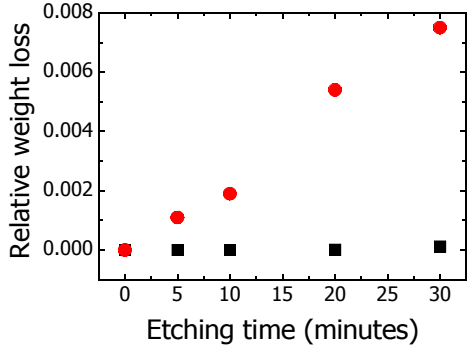

Fig. 3.7 : Relative weight loss $\Delta m/m$ after etching in HCl for a pure Ga ingot (red circles) and for a GaAs wafer (black squares).

a function of etching time, for a pure Ga ingot and a GaAs wafer, chosen to have nearly the same surface area exposed to the etchant. The mass of the two samples was measured by a balance with microgram precision. In Fig. 3.7 we show the result of this study, which clearly demonstrates the selectivity of the etchant.

Based on these data it was possible to estimate the etching rate for the two elements as around 4 μg/min for GaAs and around 250 μg/min for pure Ga. Differing the etching rates by around two orders of magnitude we also performed the etching procedure on our nanostructures. We used a 10 second immersion in HCl followed by a 1 minute rinse in deionized water, which gave good results for the selective removal of Ga without damage for GaAs. As a proof, we show, in Fig. 3.8, the AFM image of the same sample before and after the selective etching. In the left panel a Ga droplet is clearly visible and in the right panel, after the chemical treatment, metallic Ga was completely removed. The presence of a tiny GaAs ring, at the droplet perimeter could be found thanks to the very low etching rate on GaAs. In the following we will many times describe the result of the

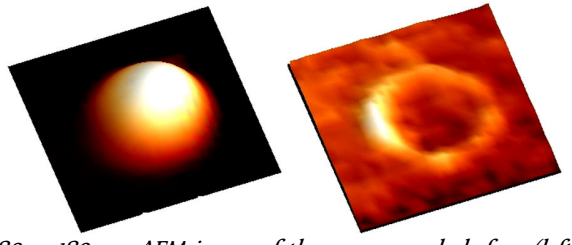

Fig. 3.8 : 180 x 180 nm AFM image of the same sample before (left panel) and after (right panel) selective etching. The etching procedure revealed the presence of a tiny GaAs ring marking the droplet perimeter.

selective etching for pure Ga and it is worth mentioning that the areas of the samples observed by AFM before and after the etching treatment were never the same, but always randomly chosen positions across the surface.

Chapter 4

"you take down my barricade and melt away my heart
if loving hurts so much I want this pain to always last
I hope you pass the test that I have failed"

(from "Part two" by No use for a name)

Ga supply: droplets nucleation

In this chapter we will focus on the phenomena occurring during Ga irradiation, which lead to the nucleation of the droplets. Extremely important also for the fabrication of nanostructures, we investigated the formation of the Ga reservoirs at the surface. Two main cases will be discussed: Ga deposition on c(4x4) and on (4x6) surface reconstructions. We will describe the early stages of the Ga supply and the droplets density dependence on the substrate temperature and Ga molecular beam flux. The results of the selective etching of pure Ga will be shown. The differences resulting from the deposition on the different two reconstructions will be commented.

4.1 Early stages of Ga deposition

The first step of the realization of GaAs nanocrystals by DE is the formation of Ga droplets on the substrate surface. After the irradiation of Ga molecular beam, nanometre-sized droplets, which typically show a narrow size distribution, are spontaneously formed. The standard experimental procedure for GaAs DE includes the growth of a GaAs buffer layer at 580°C, to recover the atomic flatness of the surface, after the oxide desorption performed at the same temperature and the deposition of an AlGaAs barrier layer again at 580°C, to provide the carrier confinement by a larger band-gap material. After these procedures, common for every sample, the substrate temperature is decreased to the desired value, typically in the range between 400°C and 200°C, and, after reaching the target temperature, the As flux is interrupted, in order to deplete the growth chamber from arsenic atoms. After less than one hour, the background pressure returns to the 10^{-10} Torr level, the substrate temperature is completely stabilized and the Ga deposition can take place. It is important to mention that, following this experimental procedure, the substrate surface reconstruction at this point is c(4x4).

In Fig. 4.1 we show the typical specular beam RHEED intensity change recorded during the deposition of Ga at 300°C, with a rate of 0.06 ML/s (black line). Just after opening the Ga cell, the specular beam intensity decreased and then increased again, showing a maximum after the supplied amount of 1 ML. After that, it decreased and increased again and, after 1.75 ML of Ga was deposited, the intensity was continuously reduced, with no other change until the end of the deposition. Simultaneously we also monitored the change in the RHEED pattern and observed that the Ga irradiation caused a transition in the surface reconstruction. Indeed the initial arrangement was c(4x4), which then changed to (2x4) after the deposition of 1 ML and finally was converted into (4x6), after the supplied amount of 1.75 ML. At this stage it was possible to distinguish the appearance of a

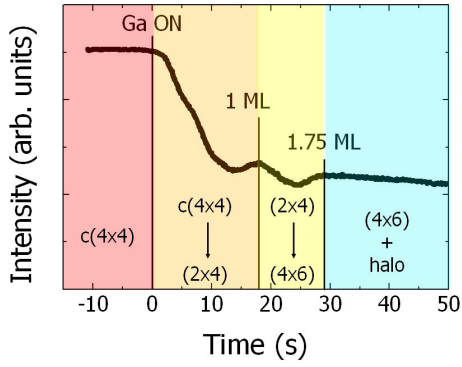

Fig. 4.1 : Specular beam intensity change recorded as a function of time, during Ga supply on an As-rich surface at 300°C with a rate of 0.06 ML/s. Different surface reconstructions are distinguished by the use of different colours.

halo pattern, meaning that the Ga droplet nucleation was started. These findings should be compared with the reported As coverages of the different surface reconstructions. As we already described in section 1.4, the c(4x4), in its β phase, has an As coverage of 1.75 ML, while the (2x4) of 0.75 ML and the (4x6) of 1/12 ML. Thus the RHEED investigations let us conclude that the initial surface reconstruction was c(4x4)β, since we needed 1 ML of Ga to change to the (2x4) and 1.75 ML to observe the (4x6). Moreover during the early stages of Ga deposition we found a transition from the As-rich to the Ga-rich configuration and then, only after the establishment of a Ga-rich surface we observed the formation of droplets. This phenomenon was confirmed not only by the appearance of the halo pattern, but also looking at the substrate morphology of a sample, where we deposited only 1.70 ML of Ga that did not result in the formation of any Ga droplet. The 10 μm x 10 μm 2D and 3D AFM image of this sample, as well as the height profile are reported in Fig. 4.2. The deposition was carried out at 300°C with a rate of 0.08 ML/s. As clearly seen by the AFM investigation, no droplets could be detected, meaning that the minimum amount of Ga to be supplied for the formation of droplets in these conditions was 1.75 ML. In other words, as long as a Ga-rich surface reconstruction is not established on the surface, Ga atoms will

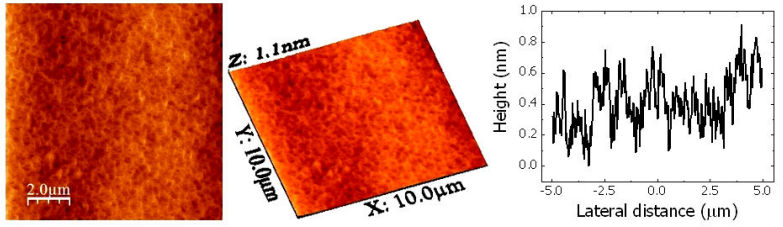

Fig. 4.2 : AFM images (2D and 3D) and height profile of the sample surface, after Ga deposition at 300°C with a rate of 0.08 ML/s.

try to saturate the bonding to As, creating a sort of adsorption layer of GaAs, with a width of 1.75 ML. Therefore, as expected thermodynamically, only on the top of the Ga-rich (4x6) surface reconstruction we can observe the formation of the droplets. This concept has a great importance, since it has a general validity and permits to understand what is the minimum amount of Ga that should be supplied to nucleate the Ga reservoirs. Indeed this quantity depends on the As coverage of the substrate before the Ga irradiation, as we found for another sample, where the III-column element deposition was performed at 400°C. In this case, the surface reconstruction of the substrate was still c(4x4), but, as shown in Fig. 4.3, where the RHEED specular beam intensity change was again

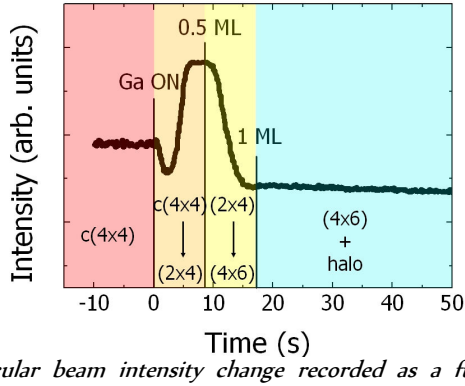

Fig. 4.3 : Specular beam intensity change recorded as a function of time, during Ga supply on an As-rich surface at 400°C with a rate of 0.06 ML/s. Different surface reconstructions are distinguished by the use of different colours.

recorded during the Ga supply, this time we obtained a different result. The specular beam intensity firstly decreased, increased showing a maximum after the deposition of 0.5 ML, in correspondence with the transition to the (2x4) reconstruction and then decreased again. After the supplied amount reached 1 ML no other change was detected and a (4x6) reconstruction with a halo pattern appeared. Therefore for this sample, the nucleation of Ga droplets, confirmed by the decrease of the specular beam intensity, similarly to what found before, started after the deposition of 1.0 ML. This was confirmed by supplying 1.3 ML of Ga at 400°C at 0.1 ML/s, as reported in Fig. 4.4. The AFM images of this sample show the formation of Ga droplets, indicating that the As coverage in this case

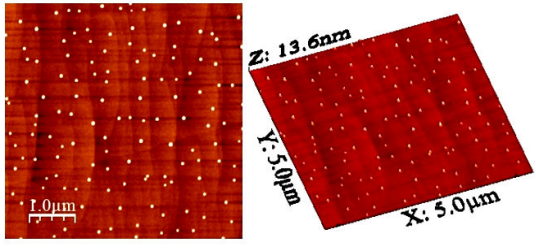

Fig. 4.4 : 5 mm x 5 mm AFM images of Ga droplets obtained depositing 1.3 ML of Ga at 400°C with a deposition rate of 0.1 ML/s.

was well below the above mentioned 1.75 ML. Thus we can conclude that the substrate surface at 400°C is more likely to be in the c(4x4)α phase, so that 1.0 ML is needed to complete the transition to the Ga-rich (4x6), as previously commented. As reported by Ohtake[103], differences in the preparation method can lead to the establishment of either α or β phase, which are difficult to be distinguished by only looking at the RHEED patterns. Moreover, it is important to remember that a mixed arrangement of α + β phases might be occurred under intermediate conditions. This fact can explain some apparent discrepancies present in the literature about the minimum supplied amount of Ga, which leads to the droplets formation. As stated above, the surface reconstruction of the substrate rules out this process and it is therefore a very important parameter to take into

account. In our work, we always found no droplets nucleation for Ga depositions lower than 1.75 ML at substrate temperature lower than 400°C. Very few experiments were performed by irradiating Ga at 400°C and in this case the coverage was found to be 1.0 ML, as should be expected from a c(4x4)α phase. In the case of Ga deposition at lower temperatures (T_{sub} = 200°C), we found a different behaviour, since in this case, no clear temporal evolution of the RHEED specular beam could be detected. Similarly to what observed at 300°C, the halo pattern was clearly seen after the supply of 1.75 ML, meaning that the substrate was in the c(4x4)β phase, but it was impossible to distinguish the transitions to the different surface reconstructions, from the As-rich to the Ga-rich phase. The specular beam intensity change recorded during Ga supply at 200°C is reported in Fig. 4.5. As will be further commented later, in the case of such a low substrate temperature, the process of formation of the adsorption layer of GaAs and the transition to the (4x6) might be not so unambiguous and we cannot exclude the presence of relatively large areas with a mixed surface reconstruction (not fully transformed to Ga-rich at the moment of Ga droplet initiation). This effects can qualitatively explain

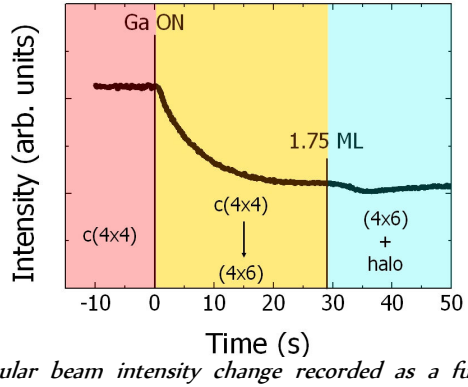

Fig. 4.5 : Specular beam intensity change recorded as a function of time, during Ga supply on an As-rich surface at 200°C with a rate of 0.06 ML/s.

the time dependence of the RHEED specular beam in the low temperature regime.

Summarizing, we have described the early stages of the Ga

deposition on the As-terminated surfaces, as normally performed in the first step of DE. We found, as a general tendency, that Ga droplets can only be formed on the top of the Ga-rich (4x6) reconstruction, while before the saturation of As bonds with Ga, no droplets could be detected. The amount of III-column element to be supplied in order to get the droplet nucleation was found to be dependent on the actual As coverage of the initial substrate surface. On the contrary, a thin GaAs adsorption layer is formed at the very beginning of the deposition. As will be discussed later, this thermodynamically favoured process must find a kinetic path, in order to be fully completed.

4.2 Ga droplets formation on c(4x4)

One of the most important features of DE is the possibility to independently control the size and the density of the quantum nanostructures, over a wide range of values. This property is a consequence of the formation of Ga droplets at different substrate temperatures and molecular beam fluxes, used for the Ga deposition. Qualitatively, when the mobility of Ga adatoms is large (high substrate temperature), the nucleation of a new stable cluster with a number of atoms exceeding the critical nucleus is not so probable, since Ga adatoms can easily find an already stabilized cluster to attach to. Similarly, when the molecular beam flux is low, the probability for Ga adatoms to meet and gather together to form a nucleus is not so high, since the population of atoms on the surface is low, in these conditions.

Deep investigations were carried out on the Ga droplets density as a function of the parameters: substrate temperature, in the range 400°C - 150°C and Ga molecular beam flux, in the range 0.02 ML/s – 2 ML/s. In this section we will report our results, obtained depositing Ga on the As-rich c(4x4) surface reconstruction. GaAs (001) substrate were overgrown with a buffer layer of GaAs at 580°C, until the RHEED pattern showed the typical features of an atomically flat (2x4) surface. Then, the substrate temperature was decreased to

the desired value, under constant As flux. After reaching the target temperature, the As flux was stopped and the As cell cooled down to completely deplete the growth chamber from As atoms. The Ga deposition started after a waiting time of around one hour, used to completely stabilize the substrate temperature and to reach the 10^{-10} Torr vacuum level in the chamber. At this point the surface reconstruction always showed the c(4x4) RHEED features. The highest densities achievable in these conditions are on the order of 10^{11} cm^{-2}, but it is important to mention that at such high density the process of droplets formation might be strongly influenced by spurious effects. Indeed in these conditions, the radius of each droplet becomes comparable with the radius of the circular area that can be occupied for a single droplet, that can be easily calculated on the basis of simple considerations, for a high packed hexagonal geometry. In Fig. 4.6 the maximum radius $r=(2\sqrt{3}\rho)^{-0.5}$, where ρ is the number of droplets in 1 nm^2, available for a single droplet is plotted as a function of the droplet density. For densities exceeding $2x10^{11}$ cm^{-2}, the radius of the area that a single droplet can occupy is below 15 nm, which is very

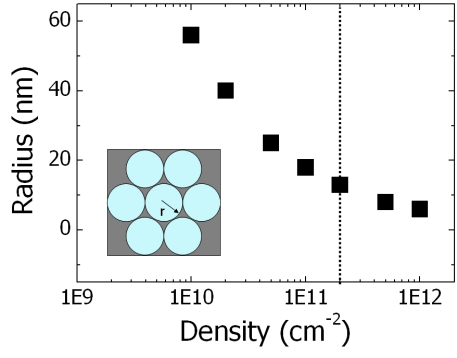

Fig. 4.6 : Maximum radius r, available for a single droplet, plotted as a function of the droplet density. In the inset, the geometrical system considered is depicted.

near to the typical size of the droplets we deposited in this study. In these conditions other phenomena, like coalescence of droplets during accretion or Ostwald ripening after the deposition, might occur due to the close spatial proximity of the droplets that can eventually touch.

Therefore, in the following analysis of the droplets density as a function of the deposition parameters we will not consider any sample where the limit value of $2x10^{11}$ cm^{-2} was exceeded.

In Fig. 4.7 (a, b) we report the results for the deposition of Ga as a function of the temperature: 5 ML and 3.75 ML with a rate of 0.1 ML/s and 0.02 ML/s, respectively. The droplets density was found to vary from the 10^{8} cm^{-2} order to 10^{11} cm^{-2} in both cases. The number of droplets is therefore strongly dependent on the substrate temperature, increasing for lower temperatures depositions, reaching values suitable for the application in the field of LED and lasers. The variation between the two set of samples resided in the different flux used, that caused the slightly lower density observed in b). Both data

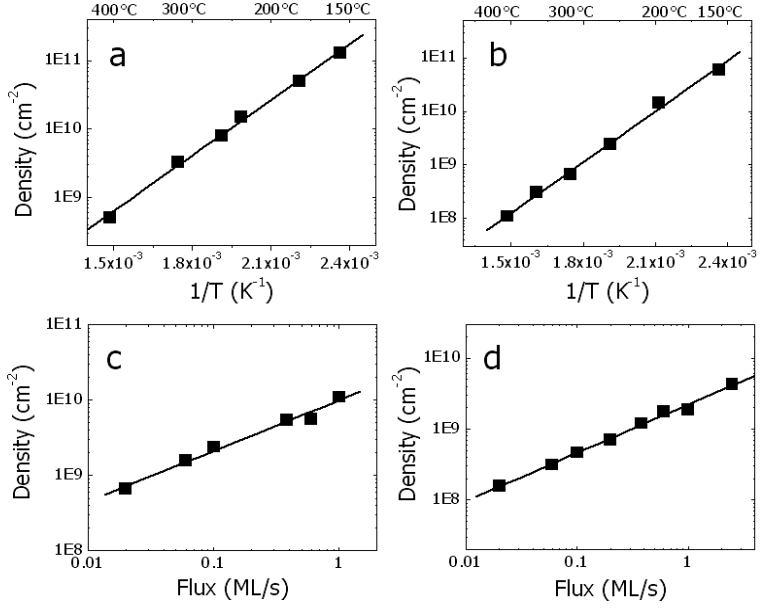

Fig. 4.7 : Density of Ga droplets as a function of reverse temperature (a, b) and molecular beam flux (c, d), obtained by large area AFM scans. The total amount of Ga supplied was 5 ML (a, d) or 3.75 ML (b, c). The fluxes used were 0.1 ML/s and 0.02 ML/s (a, b) and the substrate temperature were set at 300°C and 400°C (c, d). All the experiments were carried out on a As-terminated GaAs (001).

nicely fit an exponential law, as expected by a thermally activated phenomenon, as the adatom diffusion on the surface. The values obtained from the exponential fitting give a first estimation of the activation energy for the Ga surface migration, if we ignore other contributions, like the cluster formation energy and the adsorption energy. In the first case we obtain $E^{a}_{act}=0.54\pm0.02\,eV$ and in the second case $E^{b}_{act}=0.63\pm0.02\,eV$. This differences might be due to the actual arrangement of the substrate surface during Ga supply, which might be more ordered for lower fluxes (second case), as will be further commented later. In Fig. 4.7 (c, d) the droplet density is plotted as a function of the molecular beam flux: 3.75 ML and 5 ML at 300°C and 400°C, respectively. Again the droplets density showed a pronounced dependence on the flux, being lower for slower deposition rates, ranging from some 10^{8} cm^{-2} to 10^{10} cm^{-2} in both cases. Also in this case, the numerical differences are caused by the variation in the substrate temperature used in the two series. The slopes of the line obtained by the fitting of the data in a Log-Log graph, are $p^{c}=0.67\pm0.05$ and $p^{d}=0.68\pm0.02$ in the two set of experiments, indicating identical processes during the depositions. Indeed, as already discussed in Section 1.1, according to Venables, the density of cluster should follow a power law, depending on the number of atoms contained in the stable nucleus. In our case we are in the regime of complete condensation, since Ga sticking coefficient is 1 in these conditions. Our data about the density of droplets as a function of the Ga molecular beam flux, combined with the standard nucleation theory[3], therefore suggest the number of atoms contained in a stable nucleus to be i = 5.

Another important parameter for the fabrication of quantum confined systems is the size uniformity. Small size distributions give origin to narrow luminescence peaks, that are desirable for many applications. In DE, the size dispersion of the GaAs nanostructures is essentially determined by the original droplet one. A large distribution of Ga droplet will result in a large dispersion of the GaAs nanocrystals. The size homogeneity is therefore a key aspect in DE and was investigated, to clarify the effect of the deposition conditions

on this important parameter. In Fig. 4.8 a) we show a typical AFM image of a sample used in this study, fabricated by depositing 5 ML of Ga at 400°C with a beam flux of 1 ML/s and the radii distribution obtained by the use of the digital software for the manipulation of AFM data WSxM[97]. The same procedure used to analyse the size distribution for a large amount of samples: after the formation of Ga droplets in the MBE system, the samples were rapidly cooled down to room temperature and taken out of the chamber; AFM images were acquired and treated with the software to get the histogram distributions; a Gaussian fit was performed on these data, giving the values of the peak (X_m) and the standard deviation (σ). In the case of

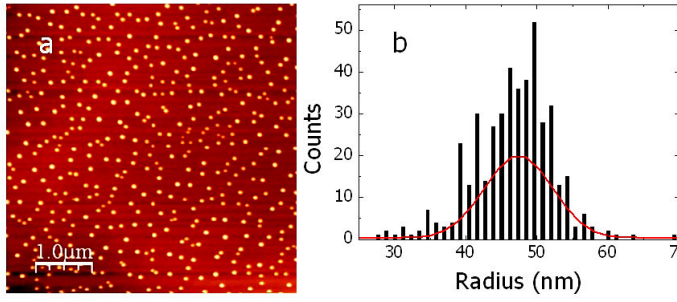

Fig. 4.8 : AFM image (a) and distribution histogram of the droplet radii (b) obtained after depositing 5 ML of Ga at 400°C with a rate of 1 ML/s. A Gaussian fit of the morphological data was performed.

the example in Fig. 4.8 the mean value and the standard deviation were 47.4 nm and 4.9 nm, respectively, resulting in a size dispersion (relative standard deviation) of 10%. Three set of samples have been analysed, by systematically changing the growth conditions of substrate temperature and molecular beam flux, used for the deposition of Ga droplets. The results are reported in Fig. 4.9, where the size dispersion is plotted as a function of molecular beam flux for the depositions at 200°C, 300°C and 400°C, as indicated in the graph. In the case of high and intermediate temperatures, the relative standard deviation was below 10% in all the range of investigation and slightly worse at higher deposition rates, but still below 20%. These

values are comparable with the best Ge/Si (001) quantum dots samples obtained by S-K growth mode[104]. On the contrary, for the low temperature set of samples the size distribution was similar to the former data only at very low deposition rates, while at higher fluxes, the size homogeneity became extremely poor. It is worth mentioning that for fast deposition rates at 200°C the resulting droplets density is very near to the limit value of 10^{11} cm^{-2}, that we already mentioned before. Phenomena connected to the physical contact of the droplets might cause effects which lead to the observed increase in the size dispersion. However the general tendency of a broadening of the size distribution in the case of low temperature and high Ga flux deposition might be the result of a reduced Ga adatoms migration length in these conditions. It is worth remembering that in the early stages of Ga deposition we observed the saturation of the bonds to As atoms and the establishment of a Ga-rich (4x6) surface reconstructions, on the top of which droplets could be formed. Moreover the RHEED specular beam intensity variation recorded at 200°C did not show any clear behaviour, in contrast to the intermediate and high temperature cases, as shown in the former section. Therefore our data suggest that when Ga adatoms have enough mobility to perfectly complete the transition to the Ga-rich

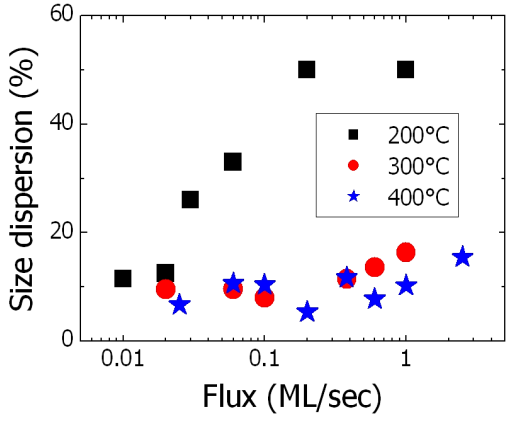

Fig. 4.9 : Relative standard deviation of droplet radii as a function of deposition rate for three set of samples, deposited at different temperatures: 200°C (black squares), 300°C (red circles) and 400°C (blue stars).

reconstruction (higher temperatures and lower Ga fluxes) the nucleation is more homogeneous. Indeed when Ga atoms migration length is too low (low temperature or high Ga fluxes) the transition to the (4x6) might not be completed all over the substrate at the moment when the nucleation of droplets starts on locally ordered (4x6). If this happens, a more heterogeneous nucleation might occur, resulting in the formation of droplets at slightly different stages of the deposition. Larger droplets might be originated on the top of the areas that firstly changed to the (4x6) reconstruction and smaller droplets might be formed on the areas that completed the transition afterwards.

The droplet density on a c(4x4) GaAs (001) substrate has been investigated, as a function of the MBE growth parameters. Substrate temperature and Ga molecular beam flux strongly influence the number of deposited droplets per unit area, giving the freedom of independently control the size and the density, over around four orders of magnitude. We also observed that the size distribution of the droplets is normally narrow, below 10%, but degrading at very low substrate temperatures. This effect might be caused by the contact between different droplets in these high density samples, which can promote a mass transfer between Ga clusters. The low Ga adatoms migration length might also play a role, preventing the complete and homogeneous establishment of the necessary Ga-rich surface reconstruction all over the substrate, before the nucleation of droplets.

4.3 Ga droplets formation on (4x6)

As we already described in 4.1 the initial stage of the Ga deposition is the formation of a Ga-rich (4x6), on the top of which, the droplets nucleation was observed. This is true in the case the initial arrangement of the substrate surface is an As-rich phase, but, as we will describe in this section, the situation changes if starting from a substrate which is already in the (4x6) phase. In order to investigate the phenomena occurring while depositing Ga on the Ga-rich surface,

we prepared the GaAs (001) substrates, following the preparation described by Ohtake[14]. After the standard growth of a GaAs buffer layer at 580°C, the substrate temperature was decreased to 500°C and the As flux closed. This high temperature annealing without As impingement causes the evaporation of As atoms from the surface which progressively changes from the As-terminated (2x4) to the Ga-rich (6x6). After around one hour annealing, the deposition of 0.3 ML of Ga promotes the formation of a perfectly ordered (4x6) reconstruction. After that, the substrate temperature was decreased to the target value of each experiment, preserving the Ga-rich phase without any other change in the RHEED pattern. In order to check the substrate morphology after this procedure, AFM investigations were performed on a sample with no further Ga supply, as shown in Fig. 4.10. The presence of large and low density droplets was detected, coming from the deposition of a small amount of excess Ga at 500°C. However, these droplets, formed during the establishment of the perfect (4x6) reconstruction, are easily distinguishable from the ones deposited at lower temperature, caused by their large dimensions (around 100 nm). Moreover caused by their low density (on the order

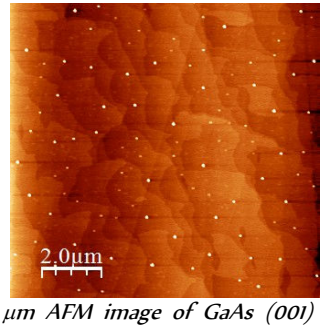

Fig. 4.10 : 10 µm x 10 µm AFM image of GaAs (001) substrate just after the procedure for the formation of a perfect (4x6) reconstruction.

of 10^7 cm^{-2}) large areas of the sample exist, where no such big droplets could be found. These areas will be investigated, after the deposition of Ga at lower temperatures, to get the desired informations. In this way we can exclude the presence of the large droplets, which in general might influence the process of nucleation of Ga droplets. By supplying Ga on the perfect Ga-rich (4x6) substrate surface, we

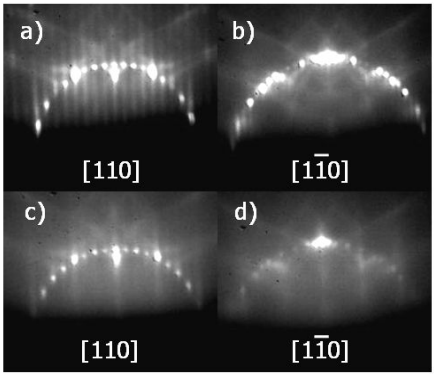

Fig. 4.11 : RHEED patterns before (a,b) and after (c, d) the supply of Ga on a (4x6) surface reconstruction. Azimuths are indicated on the figure.

immediately detected the appearance of the halo pattern, without any transition in the surface reconstruction, which remained (4x6) during Ga deposition. In Fig. 4.11 we show a typical RHEED pattern observed along [110] and [1-10] of the substrate surface before (a, b) and after (c, d) the Ga deposition on (4x6). These observations suggest that, since the most Ga-rich phase is already established all over the substrate, the irradiation of Ga immediately results in the nucleation of droplets. In order to confirm this conclusion, a set of depositions was performed in identical conditions, just increasing the supplied

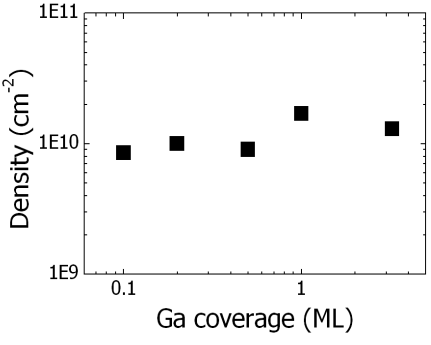

Fig. 4.12 : Droplet density as a function of the deposited amount of Ga on the Ga-rich (4x6) reconstruction.

amount of Ga, ranging from 0.1 ML to 3.25 ML at 300°C with a rate equal to 0.1 ML/s. The droplets density obtained after AFM characterization is plotted, as a function of the supplied amount of Ga, in Fig. 4.12. These results clearly indicate that as soon as new III-column element is supplied to the substrate, Ga droplets nucleation can occur, since droplets were detected even after the supply of only 0.1 ML. Moreover the density obtained in these conditions is every time nearly the same (10^{10} cm^{-2}), meaning that the droplets saturation density is achieved in a very short time. These results let us conclude that if we deposit Ga on a perfectly formed (4x6) Ga (001) surface, no adsorption layer is formed and droplets are immediately nucleated.

Similarly to the case of the droplets nucleation on the As-rich c(4x4), we studied the influence of the deposition parameters on the droplet density. For this purpose we have grown a set of samples for the dependence on the substrate temperature (at the constant flux of 0.1 ML/s) and another for the dependence on the Ga molecular beam flux (at the constant temperature of 300°C). In Fig. 4.13 the droplet density is plotted as a function of the reverse temperature (a) and of the Ga molecular beam flux. The total amount of supplied Ga was 2 ML in every sample. Also in the case of Ga deposition on a Ga-rich (4x6) substrate, the obtained number of droplets per unit area strongly depends on both substrate temperature and Ga beam flux, spanning over three orders of magnitude. The exponential fitting of

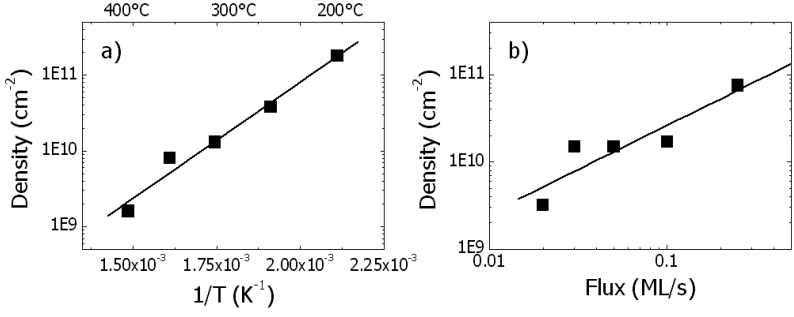

Fig. 4.13 : Droplets density on the (4x6) as a function of reverse temperature (a) and Ga beam flux (b). The total amount of supplied Ga was 2 ML in every sample. The beam flux used for the samples in (a) was 0.1 ML/s and the substrate temperature in (b) was 300°C.

the data in Fig. 4.13 (a) again gives an estimation of the activation energy for Ga migration on a Ga-rich surface. In this case we obtained $E_{act} = 0.61 \pm 0.06\, eV$, a very similar value compared to the results shown in Fig. 4.7 (b). If one applies also in this case, the above mentioned concept that the dependence of the droplets density on the beam flux can be expressed by a power law, one would obtain a value equal to $p = 1.0 \pm 0.3$, with a central value steeper compared to the previous cases. The higher value of this exponent may imply, based on the classical nucleation theory, a very large number of Ga atoms in the smaller stable cluster. However it is worth remembering that for an exponent exactly equal to 1, the classical nucleation theory cannot be used to describe the nucleation, since the number of atoms in the critical nucleus would be infinite. Different phenomena might rule out the nucleation process and another theory should be used, in this case.

As already mentioned in the previous section the size homogeneity of the Ga droplets represents an important aspect for DE. In order to continue the comparison between the cases of Ga supply on a As-rich and Ga-rich surfaces, we analysed the size dispersion for the samples obtained by forming Ga droplets an a pure (4x6) reconstruction. For this purpose, we followed the same procedure outlined the previous section. The results, which confirm the tendency towards a degrading of the size uniformity for higher

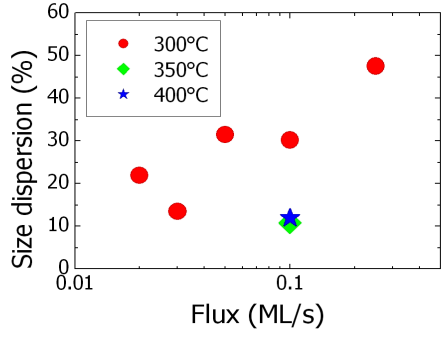

Fig. 4.14 : Relative standard deviation of droplet radii as a function of deposition rate for three different temperatures: 300°C (red circles), 350°C (green diamond) and 400°C (blue star).

deposition rates already noticed in Fig. 4.9, are shown in Fig. 4.14. For the set of samples grown at 300°C, the size dispersion was around or below 20% for very low deposition rates (less than 0,05 ML/s), increased for faster rates, reaching around 50% for 0.25 ML/s. For higher temperatures (350°C and 400°C) the dispersion became narrower, around 10% for 0.1 ML/s deposition rate, in agreement with the best samples obtained on c(4x4). From these data we can conclude that the size homogeneity for these droplets is quite poor, unless the deposition is not performed at intermediate or high temperatures. It is worth remembering that in these samples the density of the droplets is significantly larger (around 5 times) than in the case of droplets fabricated on c(4x4), under identical deposition conditions. Therefore the phenomena connected to the close contact between droplets might play an important role, even at relatively high temperatures or slow deposition rates. The observed increment of droplets density can be also seen as a reduction in the diffusion length of Ga atoms on the (4x6) reconstruction, which increases the probability for the nucleation of new droplets. A second factor which might account for this effect is the surface roughness of a perfectly formed (4x6) reconstruction. Indeed, the surface roughness analysis of the sample in Fig. 4.2, where the Ga-rich configuration was achieved by supplying 1.7 ML of Ga on the c(4x4)β reconstruction gave a value of rms = 0.28 nm, while on the pure (4x6) formed at high temperature we obtained an rms = 0.47 nm. This indicates that the roughness of the surface in the second case was higher, probably caused by the very complex unit cell of the (4x6) reconstruction, which internally shows significant differences in height, as already reported in Fig. 1.14.

Summarizing, also in the case of droplets formation on a perfectly formed GaAs (4x6) surface reconstruction a strong dependence of the number of droplets per unit area on the deposition parameters was found. The size dispersion is rapidly degrading for higher Ga fluxes even in the case of intermediate temperatures (300°C), while seems to be better (below 20%) for higher substrate temperatures. This might be due to the interaction between

neighbouring droplets, caused by their very high density, that was found to be larger than in the case of Ga deposition on c(4x4). The latter phenomenon might be explained by the larger roughness of the perfect (4x6) surface reconstruction, which can cause a reduction of Ga adatoms diffusion length.

4.4 Droplet etching on c(4x4) and (4x6)

A selective chemical etching procedure for pure Ga has been assessed during this work, as already described in 3.5. This method permits to discriminate between the presence of Ga and GaAs in the same structure, by combining the chemical etching and the AFM characterization. Indeed, during the etching, only pure Ga is removed from the substrate surface, thus leaving unaltered the GaAs portion of the system, in the case of a simultaneous presence of both materials. Crucial for the understanding of both the nucleation

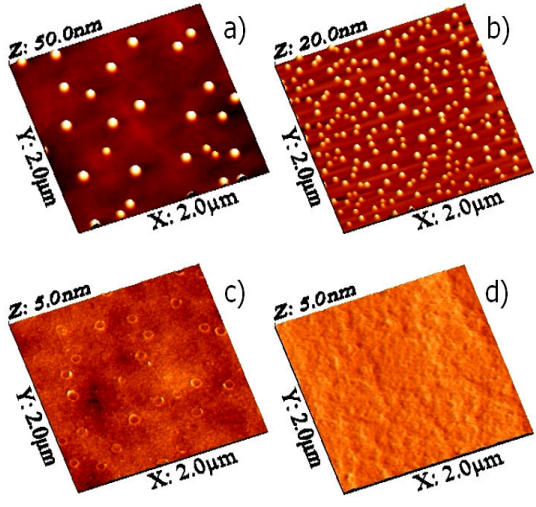

Fig. 4.15 : 2 µm x 2 µm AFM images of samples before (a, b) and after (c, d) etching. Ga was deposited under identical conditions: 10 ML at 350°C with a rate of 0.08 ML/s on As-rich c(4x4) (a) and on Ga-rich (4x6) (b).

mechanism and the realization of ring shaped GaAs nanocrystals, we performed the etching experiments on samples after the Ga deposition, under identical conditions, on the standard As-rich c(4x4) and Ga-rich (4x6). The AFM images of the samples before (a, b) and after (c, d) the etching are shown in Fig. 4.15, for depositions carried out on the As-rich surface (a, c) and on the Ga-rich (b, d). The variations in the droplets density and size between (a) and (b) are caused by the different arrangement of the substrates surface before the Ga depositions and will be discussed in the next section. Here we focus on the results of the chemical etching on the two samples. In the case of (c), after the selective removal of pure Ga, it was possible to identify tiny GaAs rings, with a number per unit area matching the original droplets density. Since the diameter of the rings, whose heights were on the order of the nanometre, was also found to be nearly identical to the original droplets one (around 80 nm), it was possible to conclude that a partial crystallization of Ga into GaAs occurred at the droplet edge, even in absence of intentional As supply to the droplets. It is worth remembering that during these experiments, the background pressure in the chamber was maintained on the order of 10^{-10} Torr, to avoid an unintentional irradiation of As to the sample surface, possibly coming from the growth chamber environment. It is instead possible that some As atoms, coming from the substrate, were dissolved inside the metal droplets and subsequently crystallized at the droplet periphery. Indeed the solubility of As in a metallic Ga droplet[105], containing around 10^7 atoms of Ga, at 350°C is small but not negligible and can lead to the dissolution of around 10^2 As atoms in each droplet. Although a quantitative discussion is quite difficult at this stage, we expect an increase of this effect with temperature, due to an increment of the solubility at higher temperatures, in good agreement with the experimental findings reported by Wang et al.[53] about the nanoholes formation upon high temperature DE. On the contrary, in the case of (d), where droplets were nucleated on a perfectly formed Ga-rich (4x6) surface, it was not possible to detect the trace of GaAs rings, marking the droplet perimeter. Only a relatively rough surface appeared after the etching, meaning that the crystallization of the droplet edge did not

occur in these conditions. Being the substrate temperature identical for both samples, this difference cannot be attributed to a change in the As solubility in liquid Ga. The different arrangement of the two substrate surfaces is more likely to have played a key role. Indeed, in the case of droplets formation on the As-rich reconstruction, some As could be dissolved inside each droplet and crystallized at the droplet edge, because in direct contact with the droplet. As we already discussed, an imperfect or incomplete transition from the As-rich to the Ga-rich limit might take place, unless the preparation of the (4x6) surface is performed at high temperature, following a special procedure. It is therefore possible that underneath each Ga droplet deposited on an As-terminated surface, some small areas were not fully Ga-terminated, before the nucleation of the Ga reservoirs. These small As-terminated areas underneath the droplets can easily release some As atoms inside the droplets, according to the solubility in the specific case, that can combine with Ga atoms at the droplet periphery, forming the observed GaAs tiny ring. In the case of a perfectly formed Ga-rich environment at the surface, the process of As dissolution is not so easy, because almost no As atoms are directly in contact with the bottom part of the droplet. If intermixing between Ga and As atoms at the topmost layers underneath the droplets is negligible, then the dissolution of As will be very low. This absence of dissolved As atoms inside the droplets would explain why no rings could be detected, after the chemical etching treatment for the sample where droplets were formed on the perfect (4x6). In Fig. 4.16 we have

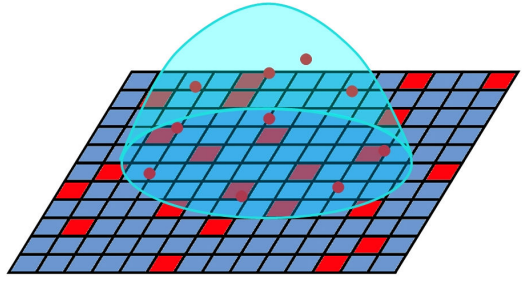

Fig. 4.16 : Drawing of the proposed explanation for the As atoms dissolution (red circles) in Ga droplets (light blue hemisphere). Ga(As)-terminated areas of the substrates are shown in blue(red).

drawn a sketch, showing the As atoms dissolution (red squares) inside a Ga droplet lying on a not perfectly formed Ga-rich surface reconstruction. Some areas underneath the droplet (in red in the figure) are still As-terminated and can therefore release As atoms inside the metallic Ga reservoirs. An imperfect establishment of a Ga-rich reconstruction all over the substrate might also play some role on the nucleation of Ga droplets, since the surface is not energetically equivalent in each point, being characterized by areas where another reconstruction is present. This effect might be more evident at low substrate temperatures, where the coexistence of different surface reconstruction is more probable, due to the low Ga adatoms mobility. A consequence of this phenomenon has already been presented and discussed in section 4.2, for the droplets deposition at 200°C.

By means of selective chemical etching and AFM characterization, we have discovered the presence of tiny GaAs ring, marking the droplet perimeter, in the samples where Ga deposition was carried out starting from the As-rich c(4x4) reconstruction. This feature was not found when depositing Ga on a perfectly formed Ga-rich (4x6). This phenomenon has been interpreted in terms of As dissolution inside the Ga reservoirs, due to the direct contact between As atoms at the substrate surface and the bottom of the droplet. This atomic arrangement can be found caused by an imperfect transition to the Ga-rich reconstruction, before the droplets nucleation. On the other side, when depositing Ga on a perfect (4x6), As atoms can be hardly dissolved, because of their small amount at the topmost layer of the substrate surface and the formation of the rings was not observed in our investigation.

4.5 Conclusion and comments

In this chapter we have reported about the investigations on the process of Ga droplets nucleation on GaAs (001) substrates. In

order to get quantitative informations about the influence of the deposition parameters (substrate temperature and Ga molecular beam flux) on the droplets density and size distribution, dedicated set of samples were grown by MBE. In particular we have performed our studies on two different surface reconstructions: the As-rich c(4x4), standard for DE-based growths and the Ga-rich (4x6). We will summarize our main results in the following.

- ✗ The early stages of the Ga deposition resulted in the establishment of a Ga-rich (4x6) reconstruction, in the case of an initial As-termination. As soon as an amount of Ga equal to the As coverage of the substrate surface was supplied, we observed the nucleation of droplets. On the contrary, on the Ga-rich surface we could immediately obtain the formation of droplets, just after the opening of the Ga shutter. Although we can conclude, based on these results, that the droplets nucleation can only occur on Ga-rich areas of the sample, it is very important to point out that the establishment of a perfect (4x6) reconstruction all over the substrate is kinetically limited. A pure Ga-rich surface can only be obtained at high temperatures, with a precise procedure, as we performed in our experiments on the (4x6) reconstruction. Therefore, when a droplet is formed during the Ga supply on a As-rich substrate, there might be areas of the sample with a different atomic arrangement at a certain time. The perfect, simultaneous reconstruction transition might only occur for high substrate temperatures and low Ga fluxes, in a more thermodynamic regime.

- ✗ The number of droplets per unit area was found to be strongly dependent on both substrate temperature and Ga molecular beam flux. The droplets density can be easily tuned over four orders of magnitude, from some 10^7 cm^{-2} to some 10^{11} cm^{-2} on both c(4x4) and (4x6) reconstructions. This freedom in choosing the desired number of droplets per unit area is very important technologically, since the number of

GaAs nanostructures fabricated by DE matches the number of original droplets. It is worth mentioning that in the case of (4x6) the density of droplets obtained under nominally identical conditions of c(4x4) was found to be around 5 times larger. A decrease in the surface diffusion length of Ga adatoms, induced by the relatively large surface roughness of the (4x6) surface might account for this phenomenon. This results is surprising since the Ga diffusion on a Ga-terminated layer is expected to be larger, compared to the diffusion on a As-terminated layer[87]. Therefore we must conclude that heterogeneous processes might play a key role in the nucleation of Ga droplets on the perfectly formed (4x6). However, due to this effect, the fabrication of ultra-high density samples can be achieved.

✗ The droplets size dispersion was discovered to depend on the deposition parameters. In general, for higher temperatures and lower fluxes the droplets size distribution was narrower, meaning that adatom diffusion plays an important role. At best we could obtain a size dispersion lower than 10%. On the contrary, for low substrate temperatures and high deposition rates, the size homogeneity was strongly reduced. This result can be a consequence of the above mentioned kinetic limitations for the establishment of a homogeneous surface reconstruction all over the substrate. In the case of the depositions carried out on the (4x6) reconstruction, the size dispersion was generally worse then on c(4x4). It is worth remembering that, in the first case, the droplets density was higher than in the second, therefore increasing the probability of a physical contact between growing islands, which may alter the process. All these spurious effect might lead to a larger size distribution in these conditions.

✗ The results of the selective etching for pure Ga on the droplets formed on the c(4x4) and (4x6) reconstructions have been shown. In the first case it was possible to detect

the presence of a tiny GaAs ring, marking the original droplet perimeter. A partial dissolution of As from the substrate inside the droplet can account for this observation. Arsenic atoms might come from some As-terminated areas which can be found underneath the droplets, as already suggested by other results. On the perfectly formed Ga-rich (4x6) it was not possible to detect the presence of GaAs rings, as expected, because of the lack of As atoms in direct contact to the bottom of the droplet.

Chapter 5

"sometimes I still see myself in that lonesome bedroom
playing my guitar and singing songs of hope for a better future
life is only as good as the memory we make
and I'm taking back what belongs to me"

(from "So long, Astoria" by The Ataris)

As supply: forming GaAs nanocrystals

This Chapter is devoted to the description of the mechanism occurring during the crystallization of Ga droplets, which originates the GaAs nanostructures. Initially we will report about the influence of the growth parameters on the nanocrystals shape and we will describe some of the common features observed in the III-V nanostructures, grown by DE. The most important processes taking place during the arsenization steps will be described in detail, clarifying which is their effect on the nanocrystal morphology. A growth mechanism which can account for the large variety of shapes attainable with the DE technique will be finally presented.

5.1 Influence of the growth parameters

In Chapter 2, we have presented the most important features of the DE growth technique, giving emphasis on the nanostructure shape design. In fact, just by changing the growth conditions it is possible to obtain nanocrystals with a different morphology. Here we describe a systematic study on the shape of the GaAs nanostructures, that was performed by exploring the growth parameter space. For this purpose we varied the substrate temperature and the As_4 molecular beam flux used for the crystallization of droplets, that, on the contrary, were formed under identical conditions for every sample. In this way we could get informations on the main processes occurring during the As supply, which promotes the formation of the III-V nanocrystals.

The samples were prepared by following the standard procedure for DE. First, GaAs (001) wafers were heated up to 580°C in order to remove the oxide and then a GaAs buffer layer was grown to ensure the atomic smoothness of the surface. After that, a 200 nm thick $Al_{0.3}Ga_{0.7}As$ barrier layer was grown at the same temperature of 580°C and Ga droplets were formed on the substrate surface, by supplying 2.5 ML at 350°C with a deposition rate of 0.08 ML/s. In Fig. 5.1 the surface morphology of the sample just after the Ga deposition is shown. Many nearly hemispherical Ga droplets were formed, with a

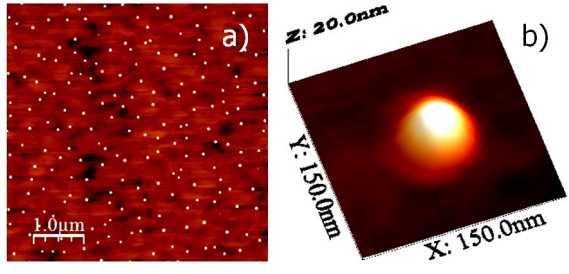

Fig. 5.1 : Large area (5 µm x 5 µm) AFM image of the sample surface just after the formation of Ga droplets (a). Magnified AFM image of a single droplet (b).

density of $8x10^8$ cm^{-2} and a typical diameter and height of around 50 nm and 20 nm, respectively. For every experiment that will be described in the following, the same procedure was used for the fabrication of Ga droplets. We can therefore assume that the configuration of the samples surface before the supply of As atoms was in every case identical to the one shown in Fig. 5.1. The growth parameters space, defined by the substrate temperature and the As_4 beam equivalent pressure (BEP) used for the crystallization of Ga droplets, was explored, in the common ranges of DE. Nine different samples were prepared, by systematically changing only one parameter, building up a sort of phase diagram for the nanostructures shape, as shown in Fig. 5.2. The substrate temperatures used were 150°C, 250°C and 350°C; while the As_4 BEP were $5x10^{-7}$ Torr, $5x10^{-6}$ Torr and $5x10^{-5}$ Torr. The crystallization time, 10 minutes, was kept constant in every case, to ensure the complete reaction of Ga with As atoms. For each sample, the AFM magnified images of a single structure are shown below. The scan ranges and heights are indicated in every image. From large area scans (not shown here) the number of GaAs nanostructures per unit area could be estimated, obtaining an excellent agreement with the original droplets density. Every droplet was thus transformed into a GaAs nanocrystal at the end of the procedure and comparisons between different samples are allowed, since the amount of material can be considered as constant. In the low temperature regime, Samples a), d) and g), the final morphology was pyramidal, typical of the QDs grown by DE, with a diameter of around 50 nm and a height of around 30 nm. No big variations were found, as the As BEP was changed. For Sample b) the obtained shape resembled the QD pair or molecule, with two QDs in close contact. The structure was strongly anisotropic, with an elongation along the [1-10] direction. The base size along this direction was indeed around 80 nm, while around 60 nm along [110]. The height of the nanocrystal was reduced compared to the former samples, being around 10 nm. Sample c) showed a ring-shaped morphology, with a well defined hole in the centre. Also in this case a certain degree of anisotropy was found, being the external diameters of the ring around 110 nm and 100 nm, along [1-10] and [110], respectively. The height of the ring was

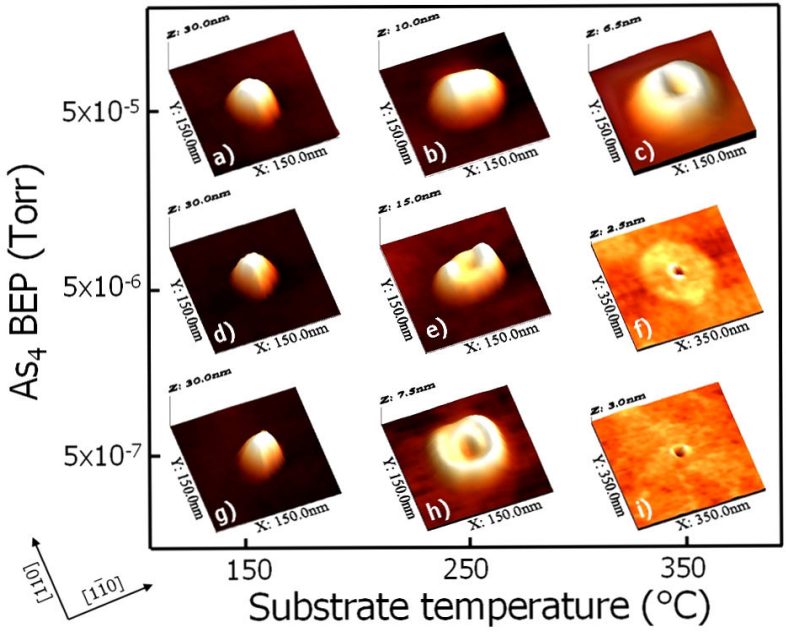

Fig. 5.2 : Single structure AFM images of GaAs nanocrystals grown by DE. Substrate temperature used for the crystallization and As_4 molecular beam flux are shown as x and y axis, respectively. The scan range is indicated for every sample.

further reduced to around 6 nm. Being the ring walls relatively thick, it was possible to measure also an internal diameter, corresponding to the central hole, of around 50 nm. The shape of Sample e) was found to be in between the cases of Sample a), b) and c), with a strong asymmetry and a hole in the centre, although not very well defined. The larger and the smaller diameters measured around 90 nm and 60 nm respectively, while the height was around 15 nm for the lateral portions of the crystal and around 6 nm at the centre. An abrupt morphological change appeared for Sample f), where a flat, nearly circular disk with a diameter of around 190 nm appeared, surrounding a central ring, which showed a diameter of around 50 nm. Along the z-axis, the outer disk and the inner ring measured around 1 nm and 2 nm, respectively. A double ring-like morphology with good rotational symmetry was obtained in the conditions of Sample h), where an

inner ring with a diameter of around 50 nm appeared in the centre, surrounded by a second ring, with a larger diameter of around 80 nm. However the two rings were slightly overlapping each other and a clear peak-and-valley line profile could not be obtained. The height of the structure was around 7 nm. Finally a crystal with a very different morphology appeared in the case of Sample i), where only a ring with a diameter and a height of around 50 nm and 2 nm, respectively was formed. It is worth adding that possible differences with what was shown in Chapter 2 may arise from the initial dimension of the droplets, much larger in our experiments.

The results of this systematic study showed that the morphology of the final GaAs nanostructures strongly depends on the conditions of the As supply to the droplets. In the relatively narrow ranges of substrate temperatures and As_4 BEP that were analysed, many different shapes could be obtained, although starting always from the same configuration. Pyramidal QDs could be fabricated at low substrate temperature (150°C), irrespectively of the intensity of the As molecular beam flux. Double divided dots, appeared when the substrate temperature was increased, under strong As irradiation and single or double quantum rings (QR) were obtained at higher temperatures. More complex structure appeared with a central ring and an outer flat disk, for high temperature and low As fluxes. As already mentioned before, the mass conservation principle should hold for every sample, since the temperatures used were low enough to prevent Ga desorption from the substrate surface. Thus the volume of the crystallized GaAs material must be conserved. In the majority of the presented samples, the main type of crystallization was 3D, developing a structures along the z-axis, by keeping the base size dimension similar or slightly larger than the original droplet one (50 nm). In these cases it is very easy to confirm the mass conservation principle. However in the special case of Sample i), the Ga atoms stored inside the original droplets cannot be consumed only for the formation of the small GaAs ring. Therefore we must conclude that a GaAs thin film was grown around the droplets all over the substrate surface, similarly to what found in Sample f), but with a much larger

disk diameter. From this findings we can say that under certain conditions the Ga atoms accumulated in the droplets maintained their position after the crystallization induced by the As supply. This is the case of the QD Samples fabricated at low temperature, where the base size of the dots and of the original Ga droplets nearly perfectly match. However when the substrate temperature/As BEP was set at higher/lower values, Ga atoms crystallized more far away from their initial position, since the diameter of the final GaAs structures was (much) larger than 50 nm. Indeed both the growth parameters caused a change in the morphology, allowing a lateral migration of Ga atoms from the original droplets. This phenomenon was already described in sections 2.1 and 2.3. Qualitatively the migration of Ga is prevented at very low temperature, because of the thermal activation of this process and hindered at higher As pressures, since in these conditions, for a Ga atom the probability of finding an arsenic atom to create a new bond is very high. Although this simple picture can generally account for the observed morphological variation that appeared in our study, there are other important features that deserve a deeper analysis.

By carefully looking at the results of Fig. 5.2, we find two effects that must be explained in order to fully understand the formation of the GaAs nanostructures upon DE. Firstly, the presence of an inner ring was observed at the centre of the structures, whose diameter was 50 nm, irrespectively of the growth conditions. Secondly, the morphology of the outer portion of the crystals was different, sometimes being ring-shaped, like in Sample h) and sometimes being disk-shaped, like in Samples f) and i). Even though the differences might not be so evident in this cases, in general, big changes in the electronic and optical properties might be expected, since a ring can be seen as a one-dimensional system, while a disk is more similar to a well, with only one confined dimension. In the following sections we will explain the origin of the inner ring, as well as the formation of a ring or a disk around the original droplets and how to control these phenomena.

5.2 Origin of the inner ring

The most important feature of the inner ring, which is often present at the centre of the DE-grown quantum nanostructures, is that, irrespectively of the growth parameters, its diameter is always matching the one of the original droplet. In the literature, the presence of the inner ring is normally explained in terms of a high reactivity of the droplet edge, since this part is simultaneously in contact with the underlying crystalline substrate and exposed to the incoming As flux[106,107]. In order to experimentally determine the nature of the inner ring, we performed a selective chemical etching on the Ga droplets, just after their formation at 350°C. As already discussed in Section 4.4, we found that, even without an intentional As supply from the cell, a tiny GaAs ring was formed underneath the droplets, marking their perimeter. In Fig. 5.3 we show the AFM image of the sample surface just after the deposition of droplets (a) and after the selective etching for pure Ga (b). The cross sectional height profiles of the single structure are shown in (c). The crystallization of the droplet perimeter was achieved without an intentional As supply, meaning that As atoms were not coming from a molecular beam flux. The arsenic background pressure was kept as low as possible (10^{-10} Torr range), in order to suppress its influence on the droplets. Thus we can neglect the impingement of As atoms on the substrate surface coming from the growth chamber. The necessary amount of As atoms

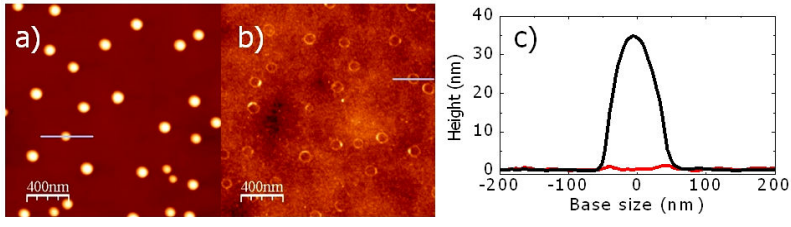

Fig. 5.3 : AFM images of the sample surface just after the deposition of Ga droplets (a) and after the selective chemical etching (b). Cross sectional height profiles of a single droplets (black line) and of a single ring (red line) are overlapped in (c).

to form the GaAs ring can come from the underlying substrate, because of a partial dissolution inside liquid Ga[105]. We believe the formation of the inner ring to be due to the establishment of an internal convection flux that transported the incorporated As atoms toward the droplet edge. Indeed, although some As can be effectively dissolved inside the droplets, the precipitation of GaAs never occurred at the centre of the droplets or homogeneously at the bottom of it, but always at the perimeter. The internal convection flux was possibly caused by a gradient in the surface tension of the droplet. If some As atoms coming from the substrate were dissolved at the bottom of the Ga droplets, a difference in As concentration respect to the top of the droplets might be established. Since the surface tension depends on the solute (As) concentration, the bottom of the droplet experienced a larger surface tension, compared to the top. In order to establish an equilibrium between the As concentration within the droplet, a convection vortex was created, in a region close to the surface. Consequently, when As atoms were transported close to the crystalline substrate surface by the internal flux, the creation of a Ga-As bond could occur. Therefore the accumulation of new GaAs material was always observed at the periphery of the droplet, marking its perimeter. This speculation is supported by the observation of an increase in the inner ring height when keeping the substrate temperature at 350°C for one hour, after the Ga droplets deposition. During the intentional Ga supply some of the Ga atoms stored in the droplets can bind to the already existing GaAs embryo, together with the As atoms impinging on the surface. Thus the inner ring structures, which clearly appeared at the end of the crystallization process, might be the combined result of the low solubility of As in the metallic Ga and of the accretion of the GaAs tiny ring, found just after the droplet deposition. These results explain why the inner rings preserved the same diameter for any growth conditions. It is worth noting that the appearance of the inner ring was detected only in samples where a significant Ga atoms lateral migration occurred. In the case of the QDs samples it is surely possible that the tiny GaAs ring was present, but after the reaction between Ga and As atoms no trace of the ring could be found, since it was completely buried under the dot.

However also in the case of the QDs, the diameter was maintained equal to the droplet one and this observation suggests that the lateral size of the nanocrystals might be fixed by the appearance of the ring at the perimeter of the original droplets. When the conditions were changed and Ga atoms could diffuse away from the droplets before completely crystallize, the GaAs inner ring was clearly revealed.

The presence of inner rings can be considered as a common feature in the DE-grown nanostructures and we have shown the reason of this phenomenon. However deeper investigation are desirable in order to understand weather the appearance of the inner ring can be controlled and eventually prevented. In our study, we investigated just one substrate temperature, in order to show the origin of the inner ring in our conditions. If the key factor for the formation of the inner ring is the dissolution of As inside metallic Ga, one should find some temperature dependence of this effect, that should eventually disappear at temperatures low enough to avoid the dissolution. We suggest that our experimental findings and explanation can also account for the reported formation of nanoholes under high temperature (around 500°C) supply of Ga on the GaAs (001) substrate[53]. The depth of these holes and the height of the ring-like protrusion surrounding them, which are much larger than in our case, supports our speculation. At higher temperatures the dissolution of As inside the droplet can be so large that Ga atoms are completely consumed by forming the GaAs ring and that, underneath the droplet, a hole-like feature is developed.

5.3 Outer zone morphology

In the phase diagram of Fig. 5.2 it was shown that, under certain growth conditions, ring-like or disk-like outer portions were formed around the inner ring. In this section we will describe which is the mechanism of the fabrication of the outer portion and how to

control its actual shape. As mentioned before, when the Ga lateral migration is activated, we observed the development of a GaAs region around the original droplets. In particular, two typical structures could be obtained, named double rings (RR) and ring/disk (RD), characterized by the presence of an inner ring, encircled by an outer region with circular symmetry. Based on similar systems, high efficiency optoelectronic devices have been recently produced[90,91]. Even though these two systems are sharing the main morphological features, RRs and RDs can be clearly distinguished, since in the first case, a clear peak-and-valley line profile is present, while in the second case, a flat disk appears around the inner ring. In the following we will show that the formation of a clear peak-and-valley height profile, typical of the RR structure, is related to the dynamics of the surface reconstruction around the Ga droplet during the arsenization step. In particular, the establishment and the subsequent ordering speed of the As-rich c(4×4) surface reconstruction around the Ga droplets during the crystallization process is the crucial ingredient for the differentiation between RRs and RDs.

A set of samples was prepared, by scanning the growth parameter space where clear RR and RD morphology can be formed. The experiments followed the standard procedure of GaAs buffer and $Al_{0.3}Ga_{0.7}As$ barrier layers growth. Ga droplets were formed by supplying 10 ML of Ga at 350°C in excellent UHV environment. Before the Ga irradiation the substrate surface reconstruction was c(4x4) but it changed to the Ga rich (4×6), during the supply of the III-column element. At this point the experimental procedure followed for the crystallization of Ga droplets by As supply was different for each sample: 4×10^{-7} Torr at 275°C for Sample A; 4×10^{-7} Torr at 300°C for Sample B; 4×10^{-7} Torr at 350°C for Sample C and 8×10^{-6} Torr at 350°C for Sample D. In every sample the As irradiation was maintained for 10 minutes in order to ensure the complete crystallization. Fig. 5.4 reports the AFM images of a single structure, one for each of the four fabricated samples. The nanocrystals showed a good cylindrical symmetry, with an outer zone morphology which varied with the exact growth conditions and an inner ring, at the centre, which

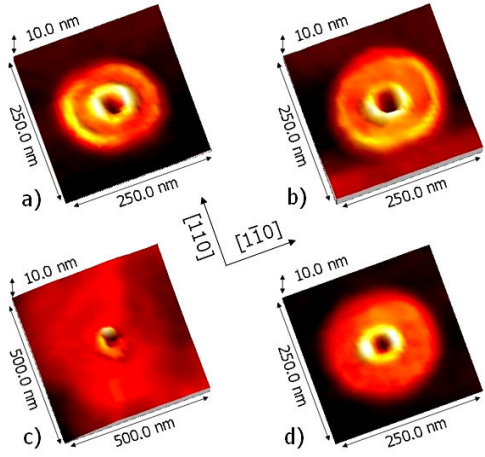

Fig. 5.4 : Magnified AFM images of the four presented samples. The crystallization conditions were: 4×10^{-7} Torr at 275°C for Sample A (a), 4×10^{-7} Torr at 300°C for Sample B (b), 4×10^{-7} Torr at 350°C for Sample C (c) and 8×10^{-6} Torr at 350°C for Sample D (d).

displayed the same radius irrespective of the sample preparation, as discussed before. On the contrary, the morphology of the outer circular regions, developed around the initially formed droplets, strongly depended on the crystallization conditions. A clear transition from the ring-like to the disk-like geometry was observed as the growth temperature was increased. More detailed data on the evolution of the outer region can be derived from the cross sectional height profiles of the same structures, shown in Figure 5.5. Comparing samples A, B and C, it was evident that increasing the crystallization temperature resulted in the enlargement of the radius of the outer GaAs regions. The area of these regions depended on the surface diffusion coefficient of Ga atoms and was thus expected to increase with the temperature. In addition to this increase of the Ga diffusion length due to larger available thermal energy, more subtle morphology changes happened, increasing the crystallization temperature. Indeed the clear peak-and-valley profile shown by the lower growth temperature samples (A and B) was replaced at higher temperatures by a flat disk (samples C and D). Moreover, the shape

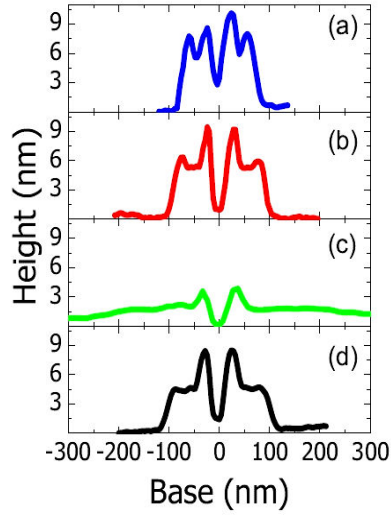

Fig. 5.5 : Cross sectional height profiles along [1-10], obtained from AFM data for Sample A (a), blue line, Sample B (b), red line, Sample C (c), green line and Sample D (d), black line.

transition between RR and RD cannot be attributed to the broadening of the diameter of the outer regions because Sample D, which had nearly the same diameter as Sample B, was instead characterized by the presence of a disk-like outer region. It is worth noting that such deep change in the nanostructure morphology took place in a rather narrow temperature window, between 300°C and 350°C. We are therefore in presence of a growth process rapidly changing with the temperature. In order to fully understand the observed behaviour, we investigated the structural configuration of the substrate surface as it is seen by each Ga droplet during our growth experiments. Since RHEED can give only an information averaged over a relatively large area, we recorded the changes in the surface structure and the specular beam intensity as a function of time, during As adsorption on a droplets-free (4×6) reconstruction. Fig. 5.6 (a) shows the typical specular beam intensity change during an As irradiation of 4×10^{-7} Torr BEP. Just after opening the As valve the specular beam increased, showing a maximum corresponding to the establishment of a (2×4)

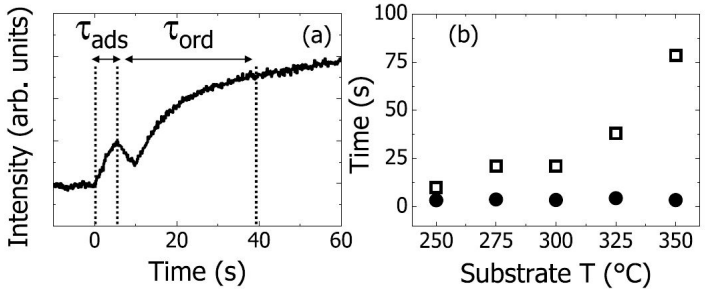

Fig. 5.6 : Typical specular beam RHEED intensity change during As ($4x10^{-7}$ Torr) adsorption on a droplets-free (4×6) reconstruction (a). τ_{ads} and τ_{ord} are indicated on the graph. Temperature dependence of τ_{ads} (circles) and τ_{ord} (squares) (b).

reconstruction, decreased and increased again, after the initiation of a c(4×4) reconstruction, which progressively ordered until the specular beam intensity showed the saturation[108]. We defined τ_{ads} as the time interval between the As cell opening and the formation of a (2×4) surface reconstruction and, in a similar way, τ_{ord} as the time interval between the establishment of the (2×4) and the ordering of the c(4×4). For the definition of τ_{ord} we took the point corresponding to $1-1/e^2$ times the saturation value of the specular beam intensity. In Figure 5.6 (b) the temperature dependence of τ_{ads} (circles) and τ_{ord} (squares) in the range used in our growth experiment is reported. It is worth noticing that the As flux and substrate temperatures used in these experiments for the As adsorption on a droplets-free (4×6) reconstruction included exactly the same conditions employed in the fabrication of Samples A, B and C. While in the first case τ_{ads} did not show any dependence on the temperature, τ_{ord} increased with increasing the substrate temperature. The process of adsorption of As atoms on the Ga-rich (4×6) until the formation of the As-stabilized (2×4), described by τ_{ads}, was therefore shown to be only dependent on the sticking of arsenic on the surface, which did not change with the temperature in the range 250°C-350°C. On the contrary, the structural changes that were needed to transform the (2×4) into the c(4×4) showed a temperature dependence, which might also account for a different sticking coefficient of As atoms on the As-stabilized

(2×4) reconstruction, in absence of Ga supply. These observations let us conclude that the appearance of c(4×4) regions was faster for lower substrate temperatures, like in the case of Sample A and B, which showed a ring-like line profile. The variation in the growth dynamics between the case of RRs and RDs can therefore arise from the different configuration of the substrate surface around the Ga droplets. Initially Ga droplets were sitting on the (4×6) surface reconstruction and, after the As supply, As adsorption promoted Ga atoms diffusion from the droplets. The size of the area covered by this diffusion was set by the average Ga migration distance, determined by the diffusion coefficient and by the As adsorption time τ_{ads}, which was almost constant in our growth temperature range. At distances much larger than the Ga migration length, no Ga originated from the droplets could be found. In these areas the substrate surface completed the transition to (2×4) and finally to the c(4×4) reconstruction, being the speed of this phenomenon, described by τ_{ord} strongly dependent on the substrate temperature, as shown before. While Ga can easily diffuse on (2×4) surface, c(4×4) regions might act as preferential nucleation sites due to the large amount of As present on this As-rich configuration. Therefore the boundary of the c(4×4) region constituted a pinning point for Ga atoms diffusion. At lower temperatures, Ga atoms migrating from the droplet and reaching the border to the quickly formed c(4×4) region, preferentially nucleated there and this phenomenon gave rise to the accumulation of GaAs at the distance from the droplets, which marked the As-rich region. This is what established the peak-and-valley line profile and it is what we normally called “outer ring”. At higher temperatures, the establishment of the c(4×4) regions around the Ga droplets was a slower process and the crystallization of the available Ga atoms might finish before the formation of the As-rich regions. Ga atoms migrating from the droplets did not find any preferential site for the nucleation and thus gave rise to the disk-like feature. In this case the lateral growth around the droplets followed a real layer-by-layer mode, as we will report in Section 6.1. Therefore the speed of the transition to the As-rich c(4×4) surface reconstruction played a key role in determining the final shape of the DE-grown nanostructures, meaning that the

surface around the Ga droplets cannot be considered as inert during the crystallization process. For these reasons, the major changes in the shape between Sample B and C can now be fully explained. From one side, the larger diameter of Sample C was caused by the larger diffusion length of Ga atoms at higher substrate temperature, while from the other side, the absence of the peak-and-valley features that was present in Sample B was determined by the slower establishment of the c(4×4) reconstruction in the conditions of Sample C. In the case of Sample D, the high temperature used for the As supply caused the formation of a disk–like outer zone, while the narrower diameter, compared to Sample C, appeared because of the shorter diffusion length of Ga atoms, in the case of higher As flux.

Summarizing we have shown that the surface reconstruction kinetics is the key factor in determining the actual shape of nanostructure. What is important is that, having understood the process of fabrication of the outer portion of the nanocrystal, we have a reliable method for obtaining the desired shape. A ring-like morphology is obtained for fast transitions to the As-rich reconstruction around the droplets, which are normally found at low substrate temperature. A disk-like shape can be fabricated by supplying As at higher temperatures when the establishment of the c(4x4) regions is slower than the crystallization process. In this way, we can control the actual shape of the outer region by setting the suitable substrate temperature and As flux used for the crystallization of the Ga droplets. As far as the size of this region is concerned, we can again play with temperature and As BEP, as will be described in the following section.

5.4 Outer zone dimension

In the previous section we have shown how to determine the shape of the outer zone, which is developed around the initially

formed Ga droplets, when a certain mobility of Ga atoms is present. In order to have a complete control over the fabrication of these GaAs nanostructures a reliable method to design not only the shape but also the dimension of the outer region is needed. After that, by only controlling the growth conditions, it will be possible to precisely design the morphology of the quantum system, in terms of size and shape, therefore accessing to a total control over the fabrication process. For this purpose, in this section we will analyse the effects of substrate temperature and As BEP on the dimension of the laterally grown GaAs region. As already mentioned, at higher substrate temperature and at lower As flux will correspond broader outer zone. In order to quantify these dependences, two set of samples were fabricated: in the first case, the As BEP was kept constant, while varying the substrate temperature used for the crystallization; in the second case, the substrate temperature was fixed and the As flux was systematically changed.

For the fabrication of the first set of samples, again the standard procedure was followed, and after the growth of the $Al_{0.3}Ga_{0.7}As$ barrier layer, droplets were formed on the surface, by

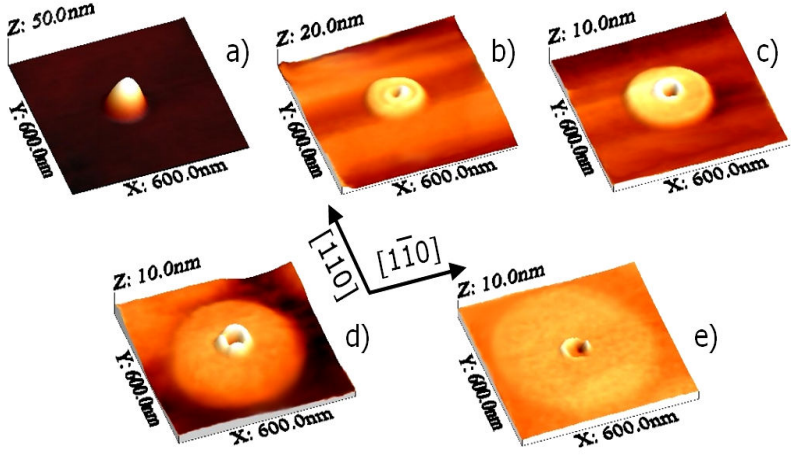

Fig. 5.7 : 600 nm x 600 nm single structure AFM images of the described samples. Ga droplet (a) and GaAs nanostructures formed at 300°C (b), 325°C (c), 350°C (d) and 375°C (e). The As BEP was 8x10^{-7} Torr in every experiment.

irradiating 10 ML of Ga at 350°C. The crystallization of Ga droplets into GaAs nanostructures was achieved by means of an As flux equal to $8x10^{-7}$ Torr at different temperatures: 300°C, 325°C, 350°C and 375°C for Sample b, c, d and e respectively. Arsenic atoms were supplied for 10 minutes, to ensure the complete crystallization of Ga atoms stored in the droplets. On the contrary, for Sample a the arsenization step was not performed, in order to check the sample surface just after the Ga deposition. After the deposition of Ga, we observed many nearly hemispherical Ga droplets, with a diameter and a height of around 90 nm and 40 nm, respectively, a density of around $6x10^{8}$ cm^{-2} and a narrow size dispersion, below 10%. A 3D AFM image of a single Ga droplet is reported in Fig. 5.7 (a). In Fig. 5.7 (b)-(e) AFM images of a single GaAs nanocrystals for each sample are ordered from the lowest (300°C) to the highest (375°C) temperature. Each structure is composed by a central ring, surrounded by an outer part whose morphology strongly depended on the growth conditions. We have already commented on the origin of the inner ring in a previous section. The outer portion of the structures changed as a function of the substrate temperature, from the double ring-like shape of Sample b to broad disks, with increasing diameter (Samples c, d and e). From the AFM analysis it was clear that when the arsenization step was performed at higher temperatures, the outer regions expanded more far away from the original droplets. Since the supplied material was the same in every experiment, as the diameter increased we also observed a progressive reduction of the disk height. The size of the outer diameter of each structure was determined by the process of Ga atoms migration during the As supply and the results indicated that this phenomenon was favoured at higher temperatures. The disk diameter can be therefore tuned on demand by simply changing the substrate temperature during As supply.

The second set of samples was fabricated following the same procedure, but this time the crystallization temperature was fixed (350°C) and the As flux was varied, to acquire informations on its influence on the crystals morphology. Again 10 ML of Ga were supplied on the $Al_{0.3}Ga_{0.7}As$ barrier layer to form the droplets and As

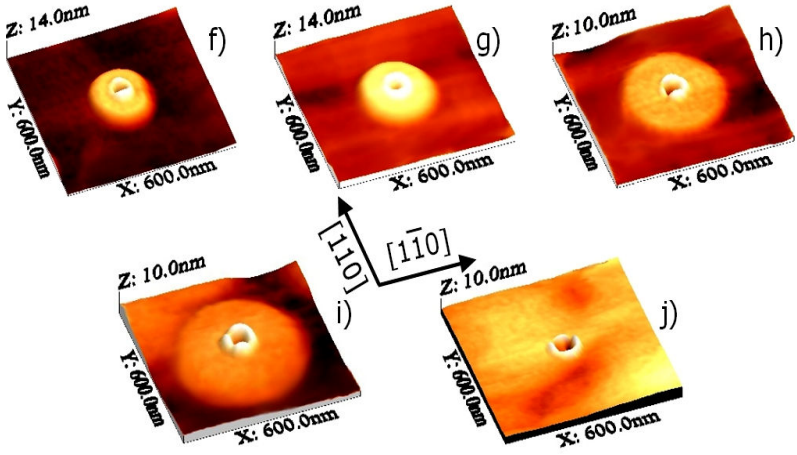

Fig. 5.8 : 600 nm x 600 nm single structure AFM images of the samples grown by changing the As BEP. The As pressures were: $8x10^{-6}$ Torr, $4x10^{-6}$ Torr, $1.6x10^{-6}$ Torr, $8x10^{-7}$ Torr, $8x10^{-8}$ Torr for Samples f), g), h), i) and j), respectively. The substrate temperature was set at 350°C in every experiment.

BEP was supplied with a different amount: $8x10^{-6}$ Torr for Sample f), $4x10^{-6}$ Torr for Sample g), $1.6x10^{-6}$ Torr for Sample h), $8x10^{-7}$ Torr for Sample i) and $8x10^{-8}$ Torr for Sample j). The single structures AFM images of each sample are shown in Fig. 5.8. Also in this case the growth resulted in a ring/disk morphology, with the inner ring showing no dependence on the growth conditions. On the contrary the outer disk-shaped region was found to be again dependent on the As flux used during the crystallization. Once again we confirmed, by our experimental data, that for higher As pressures, the disk diameter was reduced, meaning that in these conditions Ga atoms possessed a lower mobility. This effect might be due to the higher probability of creating a new Ga-As bond, in the case of strong irradiation with As atoms. If a low As BEP is used, Ga atoms are able to travel at longer distances from the original droplets, thus enlarging the outer zone diameter.

In order to give a quantitative description of the phenomena occurring during the crystallization of the Ga droplets, we carefully

analysed the nanostructures morphology. Indeed we have already discussed many times the development of outer regions around the initially formed Ga droplets, in terms of Ga atoms migration. A modelling of this process is desirable to have a deeper understanding of the nanostructure formation, as well as a reliable working model for the fabrication of new structures with similar shapes. Our model takes into consideration the process of diffusion of Ga atoms from the droplets towards the substrate surface. We assume that the origin point of the Ga atoms movement is at the droplet perimeter, spreading the III-column element atoms with a circular symmetry all over the substrate. We do not consider the well-known anisotropy in the Ga atoms diffusion[109], for simplicity. Moreover in our structures the anisotropy was not so pronounced, normally less then 10%. During the As supply, a GaAs crystal is formed around the original droplet and we therefore describe the process of migration of Ga atoms, considering their surface diffusion. Since our system is intrinsically two-dimensional and Ga atoms migration occurred on the plane, we quantitatively analysed the diffusion phenomenon in terms of the diffusion area (A_{diff}) of Ga atoms during the crystallization process, calculated as the difference between disk and inner ring areas: $A_{diff} = \pi (R_2^2 - R_1^2)$, as shown in Fig. 5.9 (a). The definition of A_{diff} is in agreement with our model, since the droplet perimeter is marked by the presence of the inner ring at the end of the growth, like we have already shown in a previous section. The physical meaning of this quantity is the area which is covered by the Ga atoms during the crystallization process. According to the diffusion laws, gallium atoms surface diffusion length is proportional to two quantities: the time interval between arrival and adsorption of As atoms, that we defined as τ_{ads} and the diffusion constant D[96]. The first can be considered independent from the temperature in this range, as we showed in Fig. 5.6 (b) and discussed before, while the second follows the law: $D = D_0 \exp(-E_{act} / k_B T)$ and is exponentially dependent on the temperature. Therefore in our system we can write: $A_{diff} \propto D \tau_{ads}$, that is the quantity we can study on the basis of our MBE growths. In Fig. 5.9 (b) and (c) the cross sectional height profiles obtained by

AFM measurements are shown, for the first (temperature dependence) and second (As BEP dependence) set of samples described before. It is worth remembering that the size homogeneity of the GaAs nanostructures followed the one of the original droplets, which was very narrow, in these conditions. For the line profiling typical structures were always selected, in order to have a reliable measurement. The diffusion area were calculated following the above mentioned relation and plotted as a function of the growth parameters, separately. In Fig. 5.9 (d) the diffusion area is plotted as a function of the reverse temperature, while the reverse diffusion area is plotted as a function of the As_4 BEP in Fig. 5.9 (e). In the first case, the data showed an excellent agreement with the expected exponential behaviour. Indeed, since τ_{ads} was constant in this range, the only quantity influencing the process which showed a temperature dependence was D. In the second case, the diffusion area was found to

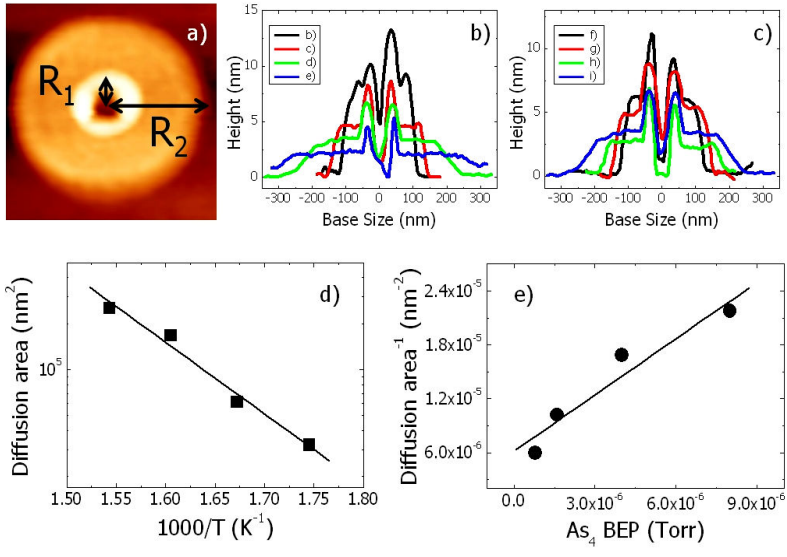

Fig. 5.9 : Definition of the diffusion area (A_{diff}) based on the radius of outer disk (R_2) and inner ring (R_1) (a). Cross sectional height profiles of the samples shown in Fig. 5.7 (b) and Fig. 5.8 (c). Diffusion area covered by Ga atoms during the crystallization as a function of the reverse temperature (d). Reverse of the diffusion area as a function of As_4 BEP (e). Best line fits are shown as black lines.

be inversely proportional to the As pressure. This behaviour was expected under the assumption that D was not depending on the arsenic impingement, so that the only quantity changing with the As flux was τ_{ads}. We confirmed that τ_{ads} doubled when the As BEP was decreased to half of the original value, supporting the experimental data. Deviations from the expected dependencies might arise from small differences between the selected and the real substrate temperatures and As_4 BEP used during our growth experiments. However both the set of experimental data nicely fitted the expected behaviour, corroborating our model based on the surface diffusion of Ga atoms from the droplets during the As impingement.

From the exponential fit of the data in Fig. 5.9 (d), it was possible to obtain $E_{act} = 0.92 \pm 0.09\, eV$, the value for the activation energy of the surface diffusion of Ga atoms during the process. This quantity can be compared with the famous value of 1.3 *eV*, obtained by Neave et al.[96], by studying the RHEED intensity oscillations on a vicinal surface, during standard GaAs MBE at high temperatures (between 550°C and 600°C). In their case, a typical diffusion length of 7.2 nm was obtained at 580°C, with a Ga flux of 1.2×10^{14} atoms $cm^{-2}\, s^{-1}$ and V/III ratio equal to 3, for a GaAs (001) which showed a (2x4) surface reconstruction. That value of diffusion length is much smaller than what we obtained during the growth of GaAs nanostructures by DE. Consequently the activation energy of the process involved in our case is smaller than what was reported. However this deviation is not surprising, considering the deep differences between the two experimental procedures. Indeed in DE one of the two constituent elements (Ga) already resides on the substrate surface, stored in droplets, while in standard MBE both gallium and arsenic are supplied from the cells. This can cause different phenomena at the surface and makes impossible to define the real V/III ratio, in our case. Another difference is the substrate temperature involved in DE which are much lower than in standard MBE. This might influence the process of incorporation of As_4 molecules in the film, that was reported to involve the cracking into two As_2 molecules[20]. Finally the actual surface reconstruction around the Ga droplets might also play a role

in determining the energy barrier for the Ga atoms diffusion.

Summarizing we have describe in detail the influence of substrate temperature and As BEP on the morphology of the outer region in GaAs ring/disk structures grown by DE. Increasing the substrate temperature and decreasing the As pressure resulted in the broadening of the outer zone. A quantitative analysis of this phenomenon was given, taking into account the process of surface diffusion of Ga atoms, moving radially from the original droplets. The temperature dependent data showed an exponential behaviour and were used to obtain a value of 0.92 eV for the activation energy of the surface diffusion. The diffusion area covered by Ga atoms during their migration was found to be inversely proportional to the As BEP. From the practical point of view, our data might be used to finely tune the nanostructure size, which is a fundamental issue for governing the optoelectronic properties of a quantum system.

5.5 Main processes during crystallization

In the previous part of this Chapter, we have described the influence of the growth conditions on the formation of GaAs crystals by DE. Substrate temperature and As flux used for the crystallization step have been shown to strongly influence the process, which resulted in the creation of different nanostructure shapes. We have already commented on the activation of the Ga atoms surface diffusion and on the formation and features of the outer portion of the crystal. Here we will summarize all these effects in a growth model which accounts for the three main processes occurring the DE growth, as was discovered by our MBE studies.

In Fig. 5.10 a schematic drawing of the crystallization event is shown. As clearly appeared from the experimental results based on the RHEED and AFM investigations, we can describe the formation of

GaAs nanostructure upon DE in terms of three main processes, indicated as 1, 2 and 3 in the figure below.

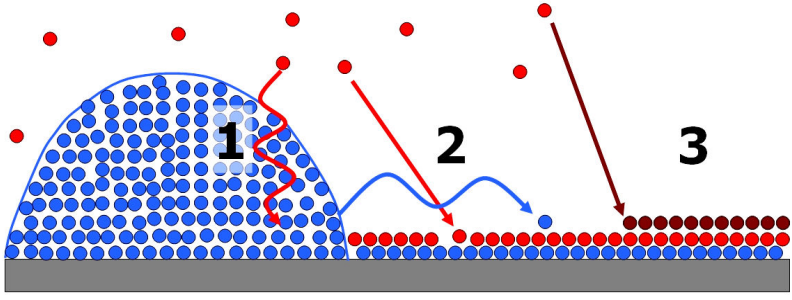

Fig. 5.10 : Sketch of the main processes occurring during the formation of a GaAs crystal by DE. The incorporation of As inside the droplet (1), the adsorption of As onto the Ga-rich surface reconstruction (2) and the transition to the As-rich c(4x4) far away from the droplet (3).

1. Incorporation of As atoms inside the droplets, leading to the formation of GaAs at the original droplet position.

2. Arrival and adsorption of As atoms at a specific site on the Ga-rich (4x6) reconstruction, creating a (2x4) reconstruction and activating the Ga atoms diffusion.

3. Establishment and ordering of the As-rich c(4x4) reconstruction far away from the original Ga droplets.

Each of these phenomena, in general, occurs simultaneously during the As supply to the droplets. Based on the growth conditions one of these processes will dominate, resulting in a certain crystal morphology. Furthermore it is very useful to describe the three events in terms of their characteristic time. We can thus define: τ_{inc} as the time interval between the starting of the As molecular beam irradiation and the complete consumption of Ga atoms inside the droplet, neglecting the III-column element surface diffusion; τ_{ads} as already described, is the time interval between arrival and adsorption of As atoms at a specific site; τ_{ord} as the time interval between the

formation of a (2x4) surface reconstruction due to the sticking of As atoms and the complete ordering of the most As-rich configuration. τ_{ads} and τ_{ord} have already been discussed in the previous section, where their effect on the outer region morphology has been clarified. It is important to stress that if the As incorporation process inside the droplets is very efficient, the expected shape is roughly pyramidal, with a constant base size, which is exactly what found in the case of QDs.

To describe quantitatively the three processes ruling the formation of GaAs nanostructures by DE, it is possible to experimentally follow them, gaining informations on the typical values of the time constants. Measurements of the RHEED features have been carried out to have a real time investigation on the phenomena occurring during the arsenization step. In particular we traced the appearing of the transmission spots during the formation of QDs, to experimentally determine τ_{inc} and we have already described how to trace τ_{ads} and τ_{ord} during As adsorption. The obtained results had to be compared with the impingement rate of As atoms onto the substrate surface, in order to get a deeper understanding of the growth kinetics. For the conversion between the BEP reading of the ion gauge and the exact arrival rate of As atoms, we used the method outlined in previous publications[87,110]. According to those treatments and similarly to what we reported in Chapter 1, the impinging rate of gas species can be written as :

$$J_i = \frac{\alpha\, p_i^{BEP}/\eta_i}{\sqrt{2\pi\, m_i k_B T}} \quad [cm^{-2}s^{-1}] \qquad (5.11)$$

where α is a coefficient determined experimentally which takes into account the MBE chamber geometry, p_i^{BEP} is the partial pressure of the gas species, as read by the ion gauge monitor, $\eta_i = [(0.4\, Z_i/14) + 0.6]$ is a correction factor for the ion gauge reading, which depends on the atomic number Z_i of the gas species[111], m_i the molar weight of the gas molecule, k_B the Boltzmann constant and T the temperature. In order to find the value of α, we investigated the case of Ga evaporation, with a cell temperature at T = 1000°C, which gave a growth rate of 0.77 ML/s, obtained by RHEED oscillations analysis. This growth rate

corresponded to an actual impinging rate of 4.8×10^{14} $cm^{-2}s^{-1}$, being the density of surface sites on GaAs (001) equal to 6.3×10^{14} cm^{-2}. The beam flux reading for the Ga molecular beam in this case was $p_{Ga}^{BEP} = 2.9 \times 10^{-7}$ Torr and inserting the proper values in (5.11), we obtained $J_{Ga} = 2.3 \times 10^{13}$ α $cm^{-2}s^{-1}$, that must be equal to the actual impinging rate of 4.8×10^{14} $cm^{-2}s^{-1}$. This equality allowed us to determine the value of the machine-related coefficient $\alpha = 20.9$, that we used in our calculations. Many factors should be taken into account when estimating the number of atoms impinging onto the substrate surface. We have discussed the coefficients α, related to the chamber geometry and η, related to the gauge response (e.g. $\eta(As_4) = 4.4$), but, especially for a short-time As supply, we should also consider the valve opening time. Indeed a needle bar is used in our arsenic cracker cell to control the irradiation. This system requires a certain amount of time to reach the desired value of flux. In Fig. 5.12 we show the As_4 BEP measurement (black line) as a function of time for a calibrated value of 8.0×10^{-7} Torr, at the steady state. During the first few seconds of irradiation the flux is not completely stabilized, still reaching the target value. The red area in the graph is the difference between the arsenic partial pressure integrated over the time between the ideal case of a perfect source (yellow area) and the real case (area below the black line) for a 4 seconds irradiation. The difference is not negligible, being around

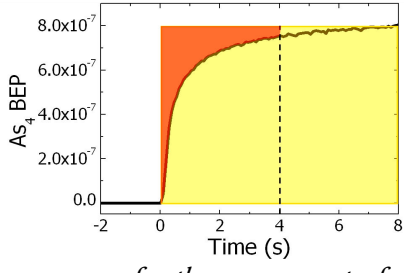

Fig. 5.12 : Ion gauge response for the measurement of As_4 molecules as a function of time (black line). Yellow rectangular area corresponds to the irradiation from a perfect source. Red area is the difference at time 4 seconds between the ideal and the real BEP.

25%. Therefore we cannot assume, for short irradiation times, an ideal behaviour of the As valved cell. The last contribution to the calculation

of the actual number of As atoms reacting at the substrate surface is coming from the As_4 sticking coefficient. In a famous publication, Foxon and Joyce[20] determined the As_4 sticking coefficient to be 0.5 on GaAs (001) surfaces above 450 K, where a pairwise dissociation-recombination reaction between As_4 molecules adsorbed on adjacent Ga lattice sites occur. Tetramers, after interacting with a couple of Ga atoms, split into two As_2 molecules; one of this is incorporated in the growing film and one is evaporated.

By applying these considerations, we compared the calculated As atoms impingement on the substrate surface with the results obtained by the RHEED investigations. The crystallization process of droplets into QDs at low substrate temperature was followed monitoring the appearance of transmission spots in the RHEED pattern. As firstly reported by Koguchi and Ishige[37] this measurements are very useful to determine the kinetic of the transformation from liquid droplet to GaAs crystal. When the transmission spot showed the saturation value, the crystallization of the droplet was completed. In Fig. 5.13 the intensity of the (333) transmission spot is reported as a function of time, for the As irradiation of $5x10^{-7}$ Torr at 150°C, corresponding to Sample g) shown in Fig. 5.2. The low temperature case was chosen in order to avoid the lateral growth of GaAs around the droplet. As insets in the figure, the

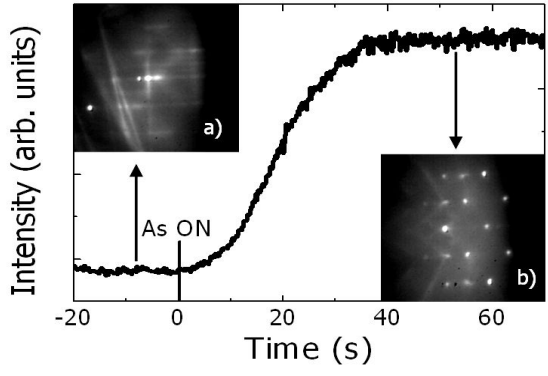

Fig. 5.13 : Intensity of the (333) transmission spot during As supply of $5x10^{-7}$ Torr to Ga droplets at 150°C. The RHEED pattern before (a) and after (b) the crystallization process are shown in the insets.

RHEED patterns before (a) and after (b) the crystallization are also shown. The 3D crystal was immediately formed just after the As cell opening and after around 40 seconds the transmission spot intensity was saturated, meaning that the whole Ga droplets was transformed into a GaAs QD. The total number of Ga atoms stored in a single droplet was estimated, from the morphological data obtained by the AFM measurements. In a droplets with a diameter of around 50 nm and a height of around 20 nm (shown in Fig. 5.1) we calculated the total number of Ga atoms to be around $1x10^6$. By applying the formula (5.11) we can also calculate the number of As atoms impinging onto a single droplet area for the time interval of 40 seconds, needed to complete the crystallization. The computed value was around $8x10^5$ atoms, for a unity sticking coefficient. In these calculations the value of 1 was used as the sticking coefficient of As on the droplets and not 0.5, in agreement with the discussion given by Hirth and Pound[112] and by Wagner and Ellis[113]. They suggested the surface of a liquid to be distinctly different from that of a perfect or imperfect crystal and has to be considered as "ideally rough", being composed of ledges and steps, only interatomic distances apart. Thus a very good agreement is found between the number of Ga atoms inside a single droplet and the number of As impinging on the droplet area for the time needed to the transmission spots to appear and saturate. Arsenic atoms efficiently stuck on the droplet surface, got incorporated inside the liquid and formed the GaAs crystal.

As far as τ_{ads} is concerned, we already described the experimental procedure used to determine this parameters, from the As adsorption on a droplets-free (4x6) surface. In the case of an irradiation with an As BEP with intensity of $8x10^{-7}$ Torr, τ_{ads} was measured to be around 2 seconds; if supplying $4x10^{-7}$ Torr, the value of τ_{ads} doubled to around 4 seconds and in the case of of irradiation with $8x10^{-6}$ Torr the time for adsorption was around 0.2 seconds. By calculating the number of As atoms impinging on the substrate surface for a given As partial pressure, we obtain that around 1 ML is adsorbed during τ_{ads}, being 0.5 the sticking coefficient of As_4 in these conditions. It is worth remembering that after a time equal to τ_{ads}, a

(2x4) surface reconstruction was detected on the RHEED pattern, meaning that the adsorption of As caused a change in the surface termination. The value of 1 ML is in fairly good agreement with the As coverage of (2x4), meaning that all of the impinging As atoms were adsorbed at their proper positions, creating bonds with Ga atoms and forming a (2x4) surface reconstruction, during the time τ_{ads}. Therefore for this process we do not need to take into account the migration of As atoms, because they immediately bounded to Ga atoms, becoming part of the crystal.

In conclusion the process of formation of GaAs nanocrystal from the original Ga droplet under As irradiation has been considered in detail. The growth conditions have been shown to play an important role on the crystallization, leading to the formation of very different morphologies in a relatively narrow window. Three main processes have been identified, based on the experimental observations: the incorporation of As at the droplet position, the adsorption of As on the substrate surface and the ordering of the c(4x4) reconstruction far away from the droplets. The energy barrier for the Ga atoms migration from the droplet during the process has been estimated from temperature dependent experiments to be 0.92 *eV*. From the calculation of the impinging rate of As atoms it was found that only the sticking of As on the (4x6) reconstructed surface was important during the initial stage of As supply. The sticking coefficient of As_4 molecules on a single droplets was discovered to be 1, according to previously reported data. As a general comment, each of the processes that were suggested to determine the crystallization into a III-V crystal can be experimentally followed by means of RHEED.

Chapter 6

"the worst is over
you can have the best of me
we got older but we're still young
we never grew out of this feeling that we won't give up"

(from "The best of me" by The starting line)

Pulsed Droplet Epitaxy

The aim of this last Chapter is to describe how we applied the knowledge gained over the growth mechanism of GaAs DE to the realization of original systems. We will report on the fabrication of original, complex GaAs/$Al_{0.3}Ga_{0.7}As$ crystals with designable morphology. A modification of the standard DE was proposed, based on pulsed As supplies to the droplets, named Pulsed Droplet Epitaxy (PDE). With this method it was possible to combine different quantum systems, such as quantum dots, rings and disks into a single nanostructure. The growth and the main morphological and optical properties of these systems will be discussed.

6.1 Ring/Disk structure

The first type of GaAs/$Al_{0.3}Ga_{0.7}As$ quantum nanostructure that we present, was actually already discussed in detail in Chapter 5. This system is named Ring/Disk, as it is composed by a central quantum ring, surrounded by a flat outer disk. The origin of the inner ring, as the result of the crystallization of the droplet edge, was presented in Section 5.2 and will be not discussed any further here. Moreover the experimental procedure for obtaining this family of nanostructures is not based on the original PDE, but on the standard droplet epitaxy, since an unique As irradiation is necessary for the formation of the coupled Ring/Disk. However we will comment on the growth dynamics of this system, as investigated by means of RHEED, because it is useful to clarify the growth mode of the outer region.

Here present the detailed fabrication process of the coupled Ring/Disk, a class of GaAs/$Al_{0.3}Ga_{0.7}As$ quantum nanostructures with excellent rotational symmetry. This system constitutes a good example of how to obtain localized states with different dimensionality and tunable coupling in a designable structure. In fact, the ring can act like a three-dimensional quantum confinement potential for the carriers, while states in the disk are expected to show a character similar to a quantum well. The fabrication procedure allows the possibility of finely tuning the Ring/Disk shape, thus allowing the realization of materials with the desired electronic density of states. This property is of the utmost importance for the engineering of the intersubband transition, a key point for the realization of devices like DWELL infrared detectors[114]. The growth of the Ring/Disk was performed on GaAs (100) substrates, following the standard preparation of GaAs buffer and $Al_{0.3}Ga_{0.7}As$ barrier layers. After that, the substrate temperature was decreased to 350 °C and the As valve closed in order to deplete the arsenic molecules from the growth chamber, until the background pressure dropped to around 1×10^{-9} Torr or less. At this point, the RHEED pattern clearly showed a c(4×4)

surface reconstruction. An equivalent 10 ML Ga molecular beam was then supplied to the substrate surface for the formation of Ga droplets. A large number of nearly hemispherical Ga droplets were formed, with an average height of around 35 nm, an average diameter of around 80 nm, and a dispersion in size of about 10%. The density of the Ga droplets was estimated to be around 6×10^{8} cm^{-2}. Just after the formation of the Ga droplets, an As flux was directed onto the substrate surface at the constant temperature of 350°C for 20 minutes, to ensure the complete crystallization of the metallic Ga into GaAs nanocrystals. We present three samples, where different As partial pressures were used during this step: 8×10^{-8} Torr (sample A), 8×10^{-7} Torr (sample B) and 8×10^{-6} Torr (sample C). In Fig. 6.1 the 2 μm × 2 μm surface area of the uncapped samples and the corresponding cross sectional height profiles along the (0-11) direction are shown. The surface morphology of sample A is bumpy, with a long-range corrugation of the order of 0.5 μm. Many nanometre sized single rings (with a height and a diameter of around 6 nm and 80 nm, respectively), encircling 3 nm deep holes were formed, as visible in (a), (d). As the As flux during the arsenization step was increased,

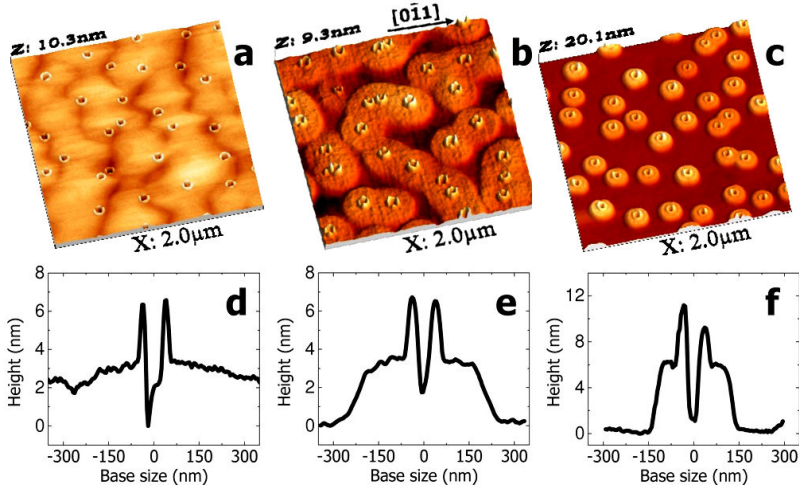

Fig. 6.1 : Top panels: 2 μm × 2 μm AFM images of the sample surfaces after arsenization of samples A (a), B (b) and C (c). Bottom panels: cross sectional height profiles along the (0-11) direction of the samples A (d), B (e) and C (f).

the surface morphology drastically changed, showing well defined Ring/Disk characterized by 4 nm high disks with a diameter of around 500 nm and inner rings marked by a 3 nm high ridge and a diameter of around 80 nm, shown in (b) and (e). A further increase of the As BEP, (c) and (f) raised the height of the inner ring and of the disk, which measured around 10 nm and 6 nm respectively, and narrowed the diameter of the outer structure to around 300 nm. On the contrary, the central hole diameter remained unaltered, also being around 80 nm in sample C. In order to assess the surface structural changes that occurred during the growth, we recorded the RHEED specular beam intensity change during the arsenization step of the three samples at 350°C, together with the observed surface reconstructions, as derived by the RHEED diffraction pattern. Immediately after the As supply, clear intensity oscillations appeared in the case of sample A (As flux = 8×10^{-8} Torr) and sample B (As flux = 8×10^{-7} Torr), with periods of around 24 and 3.6 seconds, respectively,

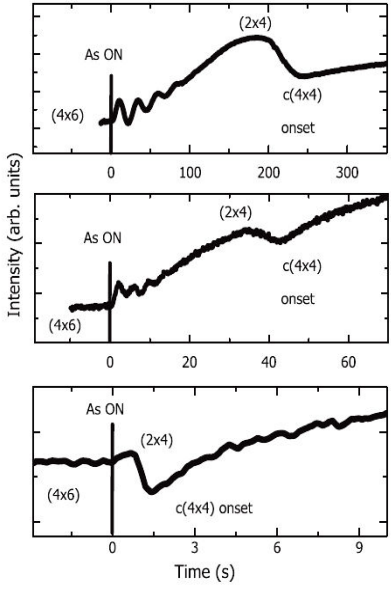

Fig. 6.2 : Time dependence of the RHEED specular beam intensity during the arsenization step for sample A (top panel), sample B (middle pane) and sample C (bottom panel). The vertical lines indicate the opening time of the As cell. The labels indicate the different surface reconstructions observed in the RHEED diffraction pattern.

while for sample C (As flux = 8×10^{-6} Torr) no intensity oscillation was observed. The behaviour of the specular beam intensity during the As supply clearly showed that, in the growth conditions of Samples A and B, the observed growth around the initial Ga droplets occurred in a layer-by-layer growth mode. The intensity oscillations damping may be caused by a progressive disordering of the 2D islands nucleation after the growth of few monolayers. In the case of a high As flux (sample C), the increase of the As BEP caused the three-dimensional growth to be enhanced, thus a reduction, and eventually a disappearance of the oscillations was expected. As far as the surface reconstruction is concerned, the initial arrangement was Ga-rich (4×6), as mentioned above. While the specular beam intensity oscillated due to the layer-by-layer growth around the droplets, its mean value increased, and, after the disappearance of the oscillations, showed a peak related to the formation of an As-rich (2×4) surface reconstruction. This increase in the specular beam intensity was probably due to the gradual establishment of the As-rich (2×4) reconstruction over the whole substrate surface. After that, while continuously supplying As, the specular beam intensity decreased, showing a minimum and then increasing again. The minimum was related to the onset of the most As-rich c(4×4) surface reconstruction, which progressively ordered, causing the observed increase in RHEED reflectivity.

These observation clearly indicated that the lateral development of the broad GaAs disk followed the layer-by-layer mode, resulting in a 2D-like, flat structure. As already presented in Chapter 5, the outer region diameter can be finely tuned, by a suitable choice of substrate temperature and As flux, used for the crystallization. In the high temperature regime, when the establishment of the c(4x4) region is slow, the obtained shape is a disk and in this growth window we have the possibility of tuning the disk morphology. Since the inner ring and the original droplet diameters are equivalent, it is possible to independently design the size of both ring and disk, for a complete control over the nanostructure morphology and electronic properties.

6.2 Multiple Concentric Quantum Rings

The possibility of fabricating semiconductor nanostructures with ring geometry has already been quickly discussed in Section 2.3. This enabled quantum mechanical experiments long fascinating the physics community, as electrons confined in nanometric rings manifest a topological quantum mechanical coherence, the Aharonov-Bohm (AB) effect[78]. Quantum rings have a peculiar and useful magnetic field level dispersion; unlike quantum dots the ground state total angular momentum changes from zero to nonzero by increasing the magnetic field[45,115]. This also results in a different energy dispersion of the excitons for different ring radius. Since charge tunneling between states of different angular momentum is strongly suppressed by selection rules, multiple concentric quantum rings eventually offer the control of effective coupling of direct-indirect excitons[116], which is of the utmost relevance in the research of semiconductor-based quantum computational devices as it could pave the way to multiple two level states devices with switchable interaction. The standard DE was employed for the first demonstration of the growth of GaAs Concentric Double Quantum Rings in 2005[41]. From that time no further development has been reported for these kind of systems. However the acquired knowledge of the mechanism ruling the fabrication of GaAs nanostructures by DE, allowed us to extend the growth protocol and obtain a real multiple ring structure, with a controllable number and diameter of the rings. The key idea of this modification of the growth sequence is very simple: the crystallization of Ga droplets is not achieved in a single As supply with a long time duration, but in different short pulses (of the orders of tenths of seconds) at variable irradiation conditions. In PDE the first As supply is used to crystallize only a defined portion of the Ga atoms stored in the droplets for the creation of the first part of the GaAs structure. A second As irradiation will continue the transformation from Ga to GaAs, but at different conditions, since it will be very easy to change the substrate temperature and/or the As BEP. This second As supply

will form another part of the new GaAs nanocrystal, but, since the attainable size and shape are strongly dependent on the growth conditions, the second step will form a crystal with different morphology. This procedure can be repeated more times, until the complete consumption of Ga atoms inside each droplet. Every portion of the final structure will be the result of different steps in the growth and will be in close spatial contact with the other. With PDE is therefore possible to fabricate complex nanostructures, where every part is designed in view of its application.

Firstly we report on the application of PDE to the formation of GaAs triple quantum rings (TQR). The first step of the growth corresponded to the supply of 10 ML of Gallium at 350°C in absence of As for the formation of droplets. Subsequently an As flux equal to 8×10^{-7} Torr was supplied at 250°C for 20 seconds and then an As flux of the same intensity was irradiated at 300 °C for 20 minutes, until the full crystallization of the deposited Ga. Well defined GaAs Triple TQR structures, with good rotational symmetry were formed from Ga droplets with the inner, middle, and outer ring diameters of around 80, 140, and 210 nm, respectively and with heights around 7 nm for the inner rings, 4 nm for middle rings, and 3 nm for the outer rings. These TQRs showed a small elongation of around 11% along the [0-11] direction, which could come from the anisotropic surface migration of Ga on the (100) GaAs surface[109] and a finite fraction of them showed defected ring structures. The inner ring diameter was again nearly equal to that of the original Ga droplet. The density of the TQR structures matched that of the original droplets (around 8×10^{8} cm^{-2}), thus confirming that all Ga droplets transformed into GaAs triple rings at the end of the process. To determine the growth dynamics of such TQR structures, we followed their formation by stopping the process and quenching the samples just after each step (Samples S1, S2, and S3) and performing a morphological characterization via AFM measurements. Because, especially after step 1 and 2, a certain amount of unreacted Ga is present on the surface, to determine its distribution and to expose the surface of the already formed GaAs structure after each step, pieces of samples S1, S2 and S3 were

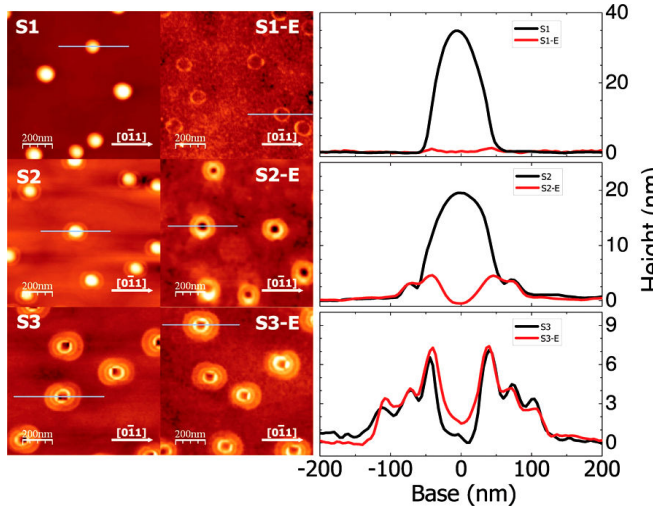

Fig. 6.3 : AFM images of as-grown samples S1, S2, and S3 (left panels), etched samples S1-E, S2-E, and S3-E (centre panels), and corresponding line profiles taken along [0-11] direction (right panels) after 10 ML Ga supply at 350°C (top panels), after 8×10^{-7} Torr As supply at 250°C for 20 seconds (middle panels), and after 8×10^{-7} Torr As supply at 300°C for 20 minutes (bottom panels).

selectively etched for pure metallic Ga, following the procedure described in Section 3.5. The etched samples were named S1-E, S2-E, and S3-E, respectively. In Fig. 6.3 the AFM images and the typical line profiles of the six samples are reported. After the 10 ML Ga supply at 350°C (sample S1), numerous nearly hemispherical Gallium droplets were formed with an average diameter of around 80 nm, height around 35 nm, and a density of around 8× 10^{8} cm^{-2}. After the etching treatment (sample S1-E), it was possible to identify the presence of a GaAs ring structure under the original droplet coming from the crystallization at the droplet edge. After step 2, that is, when the initial Ga droplets were irradiated with an arsenic flux of 250°C for 20 seconds (sample S2), we observed a complex structure formed by a central dome with the same radius of the initial Ga droplet, surrounded by a shallow ring of around 140 nm diameter. Since the short time supply of As could not completely crystallize all the Ga atoms that were present in the droplet, we expected some unreacted

Ga atoms on the surface. The morphological analysis of the corresponding etched sample (S2-E) clearly showed that the central dome was made by metallic Ga. The exposed GaAs surface of S2-E showed the formation of a double ring structure, whose inner ring was lying, in S2 sample, under the metallic Ga droplet just at the edge of it. The final As supply at 300°C for 20 minutes (sample S3) completely crystallized the Ga atoms, by forming the outermost third ring structure with a diameter of around 210 nm. At this point, a complete GaAs TQR structure was obtained. After etching (sample S3-E), no evident change was found on the morphology of the surface, thus showing that no unreacted Ga was present at the end of the procedure. As already commented, the inner ring of the structure started to formed immediately after the Ga droplets formation and was therefore present at the centre of the structure. The outer region was instead formed in the growth window where we could create GaAs rings and every As irradiation formed one ring. Totally we obtained three rings: the central was coming from the crystallization of the droplet edge, while the two outer rings were formed supplying As at the suitable conditions, controlling the lateral growth of GaAs. To confirm our model for the growth mechanism of multiple ring structures and to generalize our growth procedure, we realized a five quantum ring (FQR) structure, obtained with the technique previously described for the TQR, but extending the growth sequence, including two more arsenization steps performed at different temperatures. This time 30 ML of Ga were supplied at 350°C and four subsequent As supplies were performed respectively at 250°C, 300°C, and 325°C for 20 seconds and finally at 350°C for 20 minutes, in order to achieve the complete crystallization of the nanostructure. The AFM images (a) and (b) and the line profile (c), showing the FQR structures with good rotational symmetry, are shown in Fig. 6.4. The realization of FQRs clearly showed the success of the PDE procedure we proposed, in order to introduce new degrees of design in quantum ring structures. We observed a regular behaviour in the dependence of outer ring radii on the temperature (d). This allowed us to finely tune the radius of each ring in the structure, by a convenient choice of the substrate temperature during the arsenization step. Once again the inner ring

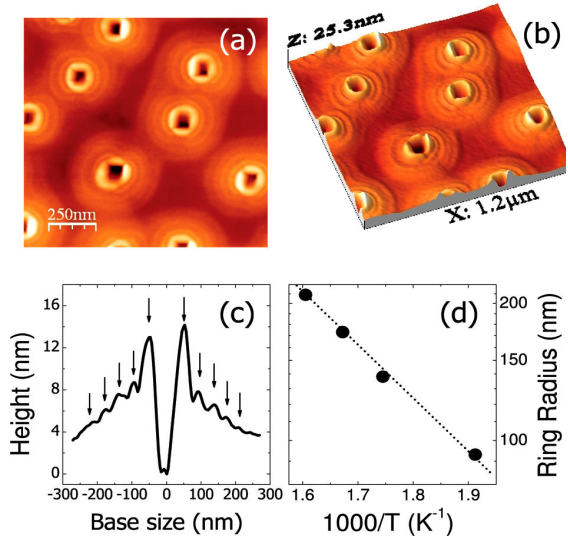

Fig. 6.4 : Two (a) and three (b) dimensional AFM images of FQRs. Line profile along the [0-11] direction of a GaAs FQR structure (c). Starting from the inner and moving to the outermost ring, the ring radii of the structures are around 50, 90, 130, 170, and 210 nm, while the heights are around 13, 8, 7, 5.5 and 4.5 nm, respectively. Arrhenius plot of outer ring radii as a function of the arsenization temperature. The dotted line is a guide for the eyes (d).

was formed following the perimeter of the original droplet and the four subsequent, short-time As pulses created the four outer rings.

The proposed procedure was shown to have a general validity, allowing the fabrication of GaAs/$Al_{0.3}Ga_{0.7}As$ multiple concentric quantum rings with a desired number and morphology. In this first example of PDE, the intensity of the As flux supplied in each pulse was every time the same, while we were changing the substrate temperature after each step. In particular the substrate temperature was varied from the lower to the higher value, in order to increase the surface diffusion length of Ga atoms and form an outer ring. However we also confirmed the success of the reverse procedure, where the subsequent As pulsed were supplied starting from the higher temperature.

6.3 Dot/Ring structure

In the case of the multiple concentric quantum rings, the formation of the same type of nanostructure (the quantum ring) was repeated within the suitable growth window to create a complex structure. However PDE also permits a more drastic change of the growth conditions between different As pulses. This leads to the coupling of structures with very different morphologies, like in the case of the fabrication of Dot/Ring structures, that we will present in the following.

In this case a first As pulse was supplied at high temperature, in the conditions where the formation of an outer ring structure occurred. A second arsenization step was performed at low temperature, for the transformation of the unreacted Ga into a GaAs QD. In order to clarify the growth procedure, the fabrication of a Dot/Ring sample was followed step-by-step, by *ex-situ* AFM characterization, as shown in Fig. 6.5. Initially Ga droplets were formed on the $Al_{0.3}Ga_{0.7}As$ barrier layer by supplying an equivalent amount of 6 ML of Ga at 350°C, leading to the nucleation of nearly hemispherical droplets (a). After the first pulse of As with an intensity of $8x10^{-7}$ Torr at 275°C for 60 seconds, an outer ring was clearly developed around the droplet, with a radius of 60 nm (b), by transforming part of the Ga stored in the droplet. This step not only resulted in the formation of a well defined GaAs ring, but also left a certain amount of Ga in the original droplet, which still resided in its initial position, as already discussed. Once again, this is the fundamental strategy of PDE: the pulsed As supply permitted the crystallization of the Ga contained in the droplet into well defined quantum nanostructure, but it still ensured that a sufficient metallic Ga remained, available for another fabrication process. In this specific case the final, second, As supply of $5x10^{-5}$ Torr at 150°C for 5 minutes formed the central quantum dot (c). At the end of the procedure a clear Dot/Ring structure appeared, with a central dot characterized by a base size of around 60 nm and a height of around 20 nm and a ring

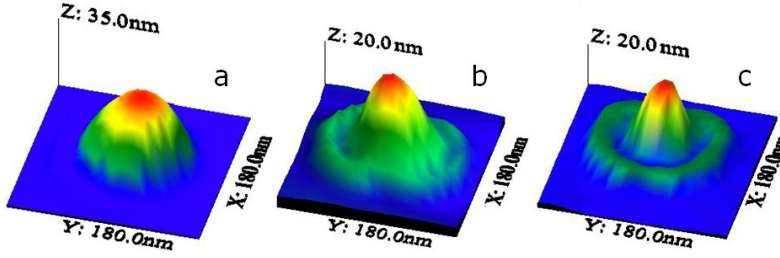

Fig. 6.5 : Evolution of the Dot/Ring formation, followed step-by-step by AFM analysis of dedicated samples. Ga droplets just after the Ga deposition (a), formation of the GaAs outer ring after the first As supply, with unreacted Ga at the centre (b), Dot/Ring formed after the second irradiation with As.

with a diameter and a height of around 120 nm and 6 nm.

For a suitable choice of the electronic structures of the Dot/Ring, one might need to change the relative height of the two building blocks of this complex nanocrystal. Indeed for the quantum confinement of these systems, the height is a very important parameters. Adjusting the relative heights of the dot and the ring provides an easy path to independently control the energy states of the two parts of the nanostructure. Since the DE is an As-limited growth, by irradiating the V-column element for a given time, it is possible to determine the volume of material to be crystallized in the first and in the second step. Thus, since with the first pulse we form the ring, increasing its time duration will result in the creation of a higher quantum ring and, by keeping a fix volume of material, of a smaller quantum dot. To give an example of this additional degree of freedom of the PDE technique, we have fabricated three Dot/Ring samples, systematically changing the time duration of the first As supply, while keeping constant any other growth parameter. The total amount of supplied Ga was 10 ML, deposited at 350°C and the intensity and substrate temperature for first As pulse were $8x10^{-7}$ Torr and 275°C. This pulse was irradiated respectively for 30, 50 and 70 seconds for Samples a, b and c. After that, a second As supply was performed at 150°C for 5 minutes, with an intensity of $5x10^{-5}$ Torr. The surface morphology of the samples is shown in Fig. 6.6 (a), (b)

and (c) and the cross sectional height profiles of single structures are compared in (d). Since the substrate temperature and the As flux intensity during the first pulse were identical in every sample, the diameter of the GaAs outer ring remained unchanged (around 160 nm). On the contrary, the height of the quantum ring increased as the time duration of the first pulsed was elongated. Simultaneously, we observed the expected reduction of the central quantum dot height. In the case of a longer first arsenizations, this effect was caused by the consumption of a larger amount of Ga atoms for the formation of the outer ring. Being the lateral size of the dot fixed by the dimension of the original droplets, the base of the QD was also constant in the three samples. On the contrary the height of the dot decreased from around 40 nm, to 35 nm and finally to 30 nm, caused by the reduction of the available Ga for the second process. Therefore we demonstrated how it is possible to control the relative heights of the dot and ring in this complex nanostructure, by a suitable choice of the time duration of the first As pulse. As a matter of fact, the diameter of the ring can be finely tuned by means of substrate temperature and As BEP, as already discussed in Chapter 5.

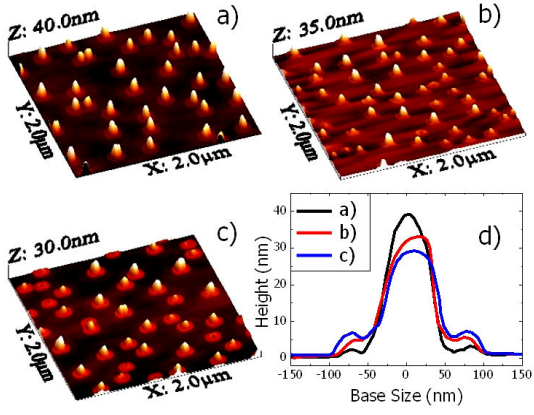

Fig. 6.6 : 2 µm x 2 µm AFM images of Dot/Ring structure where the first arsenization time was changed systematically: 30 s (a), 50 s (b) and 70 s (c). Any other parameters was kept constant. Cross sectional height profiles of a single structure. Sample a, b and c are plotted in black, red and blue, respectively.

As a further demonstration of the potential of PDE, a more complex structure was fabricated, made by two concentric quantum rings, surrounding a central quantum dot, named Dot/Ring/Ring. For the formation of this nanostructure, totally 15 ML of Ga were initially supplied at 400°C to obtain large Ga droplets. After that, two short As pulses of the same intensity ($8x10^{-7}$ Torr) were irradiated for 30 seconds at 275°C and 90 seconds at 325°C, respectively. A third As supply was performed at 150°C with a BEP of $5x10^{-5}$ Torr to form the central dot. As shown in Fig. 6.7 a clear Dot/Ring/Ring was obtained, with a relatively large dot at the centre (base size of around 120 nm and height of around 35 nm), surrounded by two concentric rings with diameters of around 200 nm and 300 nm. In this case, the procedure was more complicated compared to the previous ones since an additional step was required to form a second ring. Additionally, in order to have quantum rings with roughly the same hight, the corresponding As pulses had a different duration. Indeed an identical arsenization time would have resulted in a much smaller height for the outermost ring, as the crystallized volume would have been the same in both cases.

Thus the proposed PDE technique permitted the fabrication of even more complex systems, by coupling different building blocks in an unique III-V crystal. In the field of nanotechnology, the fabrication, just based on the self-assembly, of quantum systems with

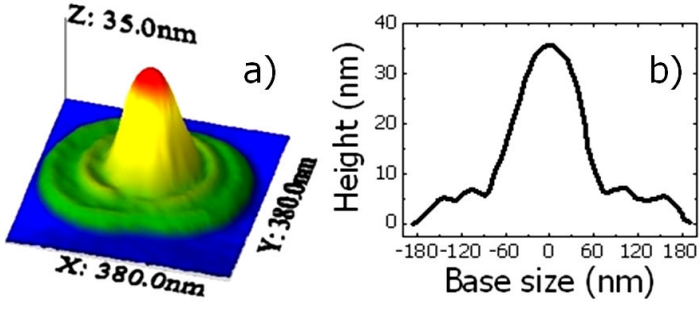

Fig. 6.7 : Magnified AFM image of a GaAs Dot/Ring/Ring, obtained by PDE with two short time pulses for the formation of the outer rings and a low temperature As supply for the formation of the central dot.

a full control over the morphology and the size has a great importance. Indeed the change in shape of a nanostructure often leads to a change in electronic state symmetries and their characteristics, the phenomena arising from shape design are very rich. At its basic level, a variation in the electronic structure is a change in the single-particle electronic states. This includes the state energy, the overall shape of the wave function, the symmetry, the polarization, and the localization. Governing the growth process we can control the optoelectronic properties of our material, in view of the fabrication of a device.

6.4 Dot/Disk structure

With the data presented and discussed in Chapter 5, we have demonstrated how to play with the growth conditions, in order to obtain a specific shape of the GaAs nanostructures upon DE. It will now be clear, after the presentation in the previous section of our PDE, that it is possible to fabricate complex systems, by coupling the structures that were singularly obtained by the standard DE. In this section we will quickly present the fabrication of Dot/Disk structures, analogous to the process of formation of the Dot/Ring. This time the first As pulse serves to create the outer flat disk, while the unreacted Ga is crystallized during the second As supply at low temperature, resulting in the establishment of the QD.

Here we present the PDE growth of three samples, where the total amount of supplied Ga was systematically changed: 10 ML (a), 7.5 ML (b) and 5 ML (c). The other growth parameters were maintained constant. Ga deposition was carried out at 350°C, the first As pulse was irradiated at 350°C for 10 seconds, with a BEP of $3x10^{-6}$ Torr and the second As supply was performed at 150°C for 5 minutes, with a BEP of $5x10^{-5}$ Torr. The single structure AFM images of the grown samples are shown in Fig. 6.8. In every sample, at the end of

the procedure, a flat disk with a diameter and height of around 280 nm and 2 nm, respectively was formed, by the lateral growth of GaAs. This portion of the crystal was developed as a consequence of the first arsenization, performed at 350°C, in the suitable growth window for the formation of quantum disks. While the outer region morphology was nearly identical for all the samples, the central part of the nanocrystal was deeply different in case of Sample c). Indeed in Samples a) and b) a QD was successfully formed, as expected, resulting from the crystallization of the unreacted Ga the remained at the initial position, after the first As pulse. On the contrary a quantum ring was present in Sample c), meaning that the first As irradiation already consumed all of the Ga atoms that were present in the droplets. In this case the second As supply had no effect on the overall morphology since no pure Ga remained after the first pulse. This speculation is supported by the observation of the QD size in (a) and (b). In the first case the dot base size and height were around 90 nm and 35 nm, while in the second case were around 80 nm and 25 nm. The systematic reduction of the initially supplied amount of Ga caused the formation of smaller droplets, going from a) to c). In the last case the first As pulse was already enough to consume all the Ga atoms to form the GaAs outer disk.

We demonstrated the fabrication of another original GaAs nanostructure, constituted by the coupling between a QD, at the centre, surrounded by a quantum disk. Again a PDE procedure was

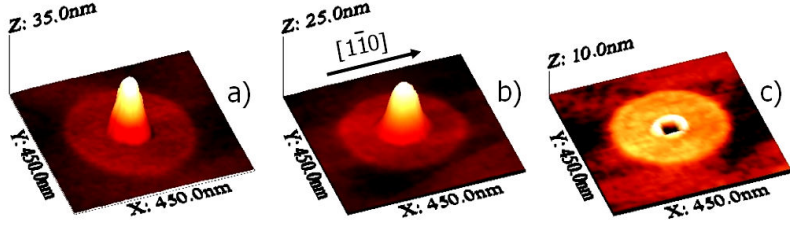

Fig. 6.8 : 450 nm x 450 nm AFM images of single GaAs nanostructures fabricated by two As pulses of $3x10^{-6}$ Torr at 350°C for 10 seconds and of $5x10^{-5}$ Torr at 150°C for 5 minutes. The initial amount of supplied Ga was 10 ML (a), 7.5 ML (b) and 5 ML (c).

established, which successfully formed a system where a 2D-like nanostructure (the disk) is in close spatial proximity with a 0D dot. The crystal morphology was shown to strongly depend also on the amount of supplied Ga, as a too low droplet size can result in the complete consumption of Ga atoms, causing the failure of the PDE approach. This is a general issue for the proposed growth procedure and care must be taken to determine the required amount of Ga atoms for the fabrication of a complex desired structure. This family of GaAs Dot/Disk structures are interesting as the disk might act as a good trapping centre for the carriers, because of its quantum well-like density of states. Being in contact with the QD, carriers might then radiatively recombine in the QD, similarly to what happens in DWELL systems.

Summarizing we have shown how to apply the acquired knowledge of the phenomena occurring in the formation of GaAs/$Al_{0.3}Ga_{0.7}As$ nanocrystals by DE for the creation of original quantum nanostructures. In particular an innovative growth mode was proposed, named PDE, that is based on the partial crystallization of the Ga droplets with short-time As pulses. PDE allowed us to fabricate GaAs mutiple quantum rings, Dot/Ring, Dot/Ring/Ring and Dot/Disk for the first time. The presented MBE approach permitted the realization of complex systems where single building blocks, such as quantum dots, rings and disks, can be combined together with a high shape flexibility. This opens the possibility to make combined quantum nanostructures and allows to overturn the general approach that stays in the background of the modern semiconductor nanodevice fabrication. With PDE the desired function is directing the fine electronic structure of the nanostructure. In fact, for the realization of devices, the optical properties of the nanocrystals such as the emission wavelength, the intersublevel spacing energy and even the interactions between nearby structures should be freely accessible for engineering. With PDE, the electronic properties are thus designed on demand for a specific device function. In the last section we will present some of the optical and electronic properties of the fabricated nanostructures, as a demonstration of their high quality, making them suitable for the

application in optoelectronics.

6.5 Optical and electronic properties

Semiconductor nanostructures have been extensively investigated because of their potential application in the field of optoelectronics as active elements for lasers[23,117], light-emitting diodes[118], detectors[119] and quantum information technology, as sources of entangled states[120,121]. Recently, there has been an increasing demand for the realization of complex quantum confined systems[122] for both practical applications and fundamental studies, including geometrical quantum phase[123], spin-spin interaction[124] and quantum state couplings[116]. Our contribution in this field is the realization of nanostructures by the use of the standard DE or of the innovative PDE techniques. As shown in the previous sections, many different families of GaAs/$Al_{0.3}Ga_{0.7}As$ nanocrystals can be fabricated, by combining together the three main shapes attainable: dots, rings and disks. It is worth stressing that no special pre-growth treatments, like patterning, *in-situ* or *ex-situ* etchings, lithographic steps are necessary, since the methods studied are completely based on self-assembly. In this section we report the optical investigations performed on some of the presented structures, by means of photoluminescence (PL) spectroscopy and electronic structure calculations, based on effective mass approximation.

Firstly we present the ensemble optical emission of TQR structures embedded in a $Al_{0.3}Ga_{0.7}As$ matrix and annealed in As atmosphere at 650 °C, for crystalline quality recovery. The photoluminescence was measured at T = 15 K and excited in the $Al_{0.3}Ga_{0.7}As$ barrier with a green laser (λ_{exc} = 532 nm) at an excitation power density P_{exc} = 10 W/cm^2. A clear emission peak was detected at E_A = 1.56 eV (band A), with a full width at half maximum 30 meV, above the excitonic GaAs signature at 1.519 eV. As excitation power

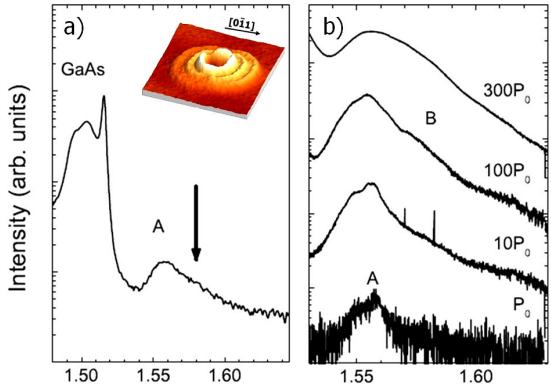

Fig. 6.9 : PL spectra of the TQR sample measured at T = 15 K and P_{exc} = 10 W/cm^2 (a).The arrow indicates the theoretical prediction, based on the AFM image reported in the inset. PL spectra of the TQR sample measured at T = 15 K, as a function of P_{exc} in the range 5 – 1500 W/cm^2 (b). Here P_0 = 5 W/cm^2.

density was increased Fig. 6.9 (b) a second band (band B) appeared on the high energy side of the fundamental band (E_B = 1.58 eV). The intensity of this band increased superlinearly with P_{exc}. It is worth mentioning that the presence of the bands A and B was strictly related to the presence of the TQR in the sample. This was tested by growing and measuring a sample, with the identical growth process, but where the TQR formation was not performed. Thus the good optical quality of these family of nanostructures was confirmed. In order to safely attribute these emission lines, we performed electronic structure calculations, within the effective mass approximation, following the approach outlined by Marzin and Bastard[125]. It is worth noticing that, in our lattice-matched GaAs/AlGaAs rings, strain effects were negligible and for that reason, a simple effective-mass approach was expected to provide accurate energy levels. The present calculations neglect Coulomb interaction between an electron and a hole, because the exciton binding energy and its dependence on relevant (single-carrier) transitions should be sufficiently below our experimental accuracy, set by the inhomogeneous broadening of the emission lines. The materials parameters used in the calculation are reported in Table 6 for GaAs and $Al_{0.3}Ga_{0.7}As$, based on the results described in Section

1.3. In the calculations, the potential for quantum confinement was derived by the actual shape of a randomly chosen TQR, measured by AFM and by imposing a cylindrical symmetry to the confining potential. The predicted TQR ground state transition energy was E_{GS} = 1.58 eV. The ground state wavefunction was found to be completely localized in the inner ring. The first radial excited state was located 20 meV above the ground state (E_{ES} = 1.60). The wavefunction was, also in this case, localized within the inner ring volume. The predicted transition energy E_{GS} laid well within the A line bandwidth. This allowed us to safely attribute band A to the ensemble emission from the TQR ground states. On the other side, the energy difference between A and B bands matched the energy difference E_{ES}–E_{GS} = 20 meV. In addition, the P_{exc} behavior of band A and B was very similar to that shown by quantum dot ensembles, where the additional band appearing at high P_{exc} was attributed to excited states emission. The excited state population in quantum dots is linked to the ground state by a waterfall–like chain, thus being visible only when the ground state of the QD is occupied. On this basis, we attributed band B to the first excited transition. It should be stressed that the linked dynamics between the ground state and the first excited state stems from the fact that the two are localized within the same ring, thus showing an agreement with what has been found in single ring structures[83].

Quantity	Units	GaAs	$Al_{0.3}Ga_{0.7}As$
CB eff. mass	m_0	0.067	0.093
VB eff. mass	m_0	0.51	0.57
CB offset	meV	262	
VB offset	meV	195	

Table 6 : Material parameters used in the effective mass calculation for the conduction band (CB) and the valence band (VB)

As a further test of the optical quality of our nanostructures, we investigated the photoluminescence of a capped Dot/Ring sample.

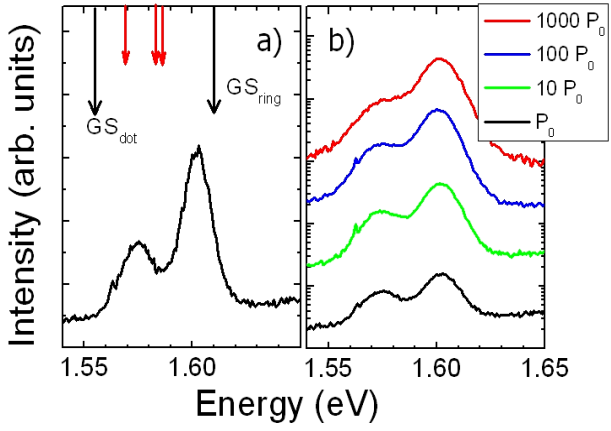

Fig. 6.10 : PL of the Dot/Ring sample at T = 14 K, λ_{exc} = 532 nm and $P_{exc} = P_0$ = 60 mW/cm² (black line). The black arrows report the theoretically predicted ground state optical transition energies of the dot and the ring. The red arrows indicate the dot excited state transition energies (a). PL of the Dot/Ring sample at $P_{exc} = P_0$ (black line), P_{exc} = 10 P_0 (green line), P_{exc} = 100 P_0 (blue line), and P_{exc} = 1000 P_0 (red line) (b).

The growth procedure followed the one outlined in Section 6.3 and the AFM image of the uncapped sample was already reported in Fig. 6.5 (c). Another identical sample was buried in $Al_{0.3}Ga_{0.7}As$ and then annealed at 700°C just after the growth for 1 hour in the MBE chamber, to improve the optical quality of the structure. The PL emission was detected at 14 K using a closed-cycle cold-finger cryostat and at room temperature (RT) by using a Nd:YAG laser (λ_{exc} = 532 nm), as excitation source. Dot/Ring emission at T = 14 K measured with a laser an excitation power density P_0 = 60 mW/cm² is reported in Fig. 6.10 a). The spectrum showed a clear double peak structure, whose bands were centred at 1.57 eV and 1.60 eV, respectively. Increasing the excitation intensity up to a factor one thousand above P_0, as shown in Fig. 6.10 b), the two bands showed a slightly superlinear behavior, with a constant integrated intensity ratio. Such behaviour is the fingerprint of a decoupled carrier dynamics. Only a broadening of the emission of the lower band was observed at high excitation power. By comparison with the theoretical predictions

(shown as black arrows in Fig. 6.10) we attributed the lower energy band to the emission from the dot ground-state (E_{dot} = 1.556 eV) and the second band from the ring ground-state (E_{ring} = 1.614 eV). The dependence of the PL on the excitation power density confirmed this attribution. As in the double ring case[84], angular momentum conservation prevented and easy carrier transfer between the dot and the ring, thus allowing the simultaneous observation of the emission from the two from the dot and the ring. The broadening of the dot emission at high excitation power density can be attributed to the population of dot excited states (red arrows in Fig. 6.10). It is worth mentioning that the PL emission for the Dot/Ring sample could be detected even at room temperature, indicating the excellent quality of the grown structure. The results of the theoretical investigations, based on effective mass approximation, on this type of nanostructure are reported in Fig. 6.11. The same procedure and material parameters

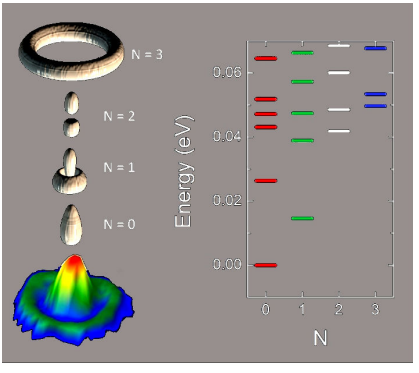

Fig. 6.11 : Energy states of the Dot/Ring structure. We consider the quantized motion of two-dimensional degrees of freedom: the radial motion, as specified by the principal quantum number N, and the rotational motion, as specified by the angular momentum j (rotational quantum number). Left panel: isosurface plots of the electronic probability density at 50% of the maxima in the Dot/Ring. From bottom to top, these panels show the electron wave function of the ground state (N = 0), and first two excited radial states (N = 1 and N = 2) which correspond to a wave functions totally localized in the dot, and that of the fourth excited radial state (N = 4), fully localized in the ring. The AFM image of the analysed structure is reported as well. Right Panel: Calculated energy emission. Green, Red and blue lines respectively represent the calculated energies (respect to the ground state) of the electron states of N = 0, N = 1, N = 2 and N = 3 series with increasing angular momenta.

of the previously mentioned case of the multiple quantum rings were used. Both dot and ring were found to be capable of quantum confinement, giving rise to the well know ladder of quantum states belonging to carriers confined in the dot and the ring. According to this calculation, we safely attributed the emission found in the PL investigations.

In conclusion we have presented the growth and the properties of the GaAs/$Al_{0.3}Ga_{0.7}As$ nanostructures grown by PDE. This method demonstrated a great potential for the fabrication of complex quantum systems which showed excellent optical quality. The PL properties of every presented structure are currently under further investigation. The size and the overall morphology of these structures are fully accessible through the control of growth parameters, only based on self-assembly. The optical investigations and the electronic structure calculations proved the possibility of the application of the PDE-grown nanocrystals as active elements in optoelectronic devices. More fundamental studies on the interaction between carriers localized on closely packed quantum systems with similar or different dimensionality are also possible, based on the proposed method. This unprecedented control over the self-assembled fabrication will therefore permit the study of basic interactions between coupled quantum systems, as well as the conception of novel devices.

Conclusion

The fabrication of GaAs/AlGaAs quantum nanostructures by DE has been studied, combining the MBE growth and material characterization.

The formation of Ga droplets on GaAs (001) surfaces has been investigated and the influence of the deposition conditions on the droplets ensemble was revealed. Governing the nucleation of Ga droplets it is possible to determine their size, number per unit area and size distribution. A key factor for the droplet formation is the initial surface reconstruction of the substrate surface before the Ga supply.

The most important atomic processes occurring during the transformation of Ga droplets into GaAs nanostructures were identified. The interplay between these phenomena is responsible of the numerous nanocrystal shapes which can be fabricated by DE. Obtaining a deep control over the crystallization process allows the design of the desired nanostructure shape.

The knowledge of the processes involved in DE permitted the fabrication of original GaAs nanocrystals with complex shapes, made by the coupling of different quantum systems, developed from the same original droplet and, therefore, in close spatial proximity. The optical investigations revealed the good quality of the grown materials.

The number, size, shape and complexity of GaAs/AlGaAs quantum nanostructures are therefore fully accessible through the pure self-assembly upon DE. This will enable further investigations on the coupling between electronic states localized on different quantum systems as well as the realization of optoelectronic devices.

References

[1] Herman, M. A. and Sitter, H., *Molecular Beam Epitaxy*, 2nd edn., Springer, (1996).
[2] B. Voigtländer, *Surf. Sci. Rep.* **43**, 127, (2001).
[3] J. A. Venables, G. D. T. Spiller and M. Handbücken, *Rep. Prog. Phys.* **47**, 399, (1984).
[4] J. V. Barth, G. Costantini and K. Kern, *Nature* **437**, 671, (2005).
[5] J. A. Venables, *Surf. Sci.* **299/300**, 798, (1994).
[6] E. Bauer, *Z. Kristalogr.* **110**, 3720, (1958).
[7] L. Pavesi and M. Guzzi, *J. Appl. Phys* **75**, 4779, (1994).
[8] K. H. Chang, C. P. Lee, J. S. Wu, D. G. Liu, M. H. Wang, L. J. Chen and M. A. Marais, *J. Appl. Phys* **70**, 4877, (1991).
[9] S. Logothetidis, M. Cardona and M. Garriga, *Phys. Rev. B* **43**, 11950, (1991).
[10] J. S. Blakemore, *J. Appl. Phys.* **53**, R123, (1982).
[11] B. El Jani, K. Kohler, K. N'Guessan, A. B. Hadj and P. Gibart, *J. Appl. Phys.* **63**, 4518, (1988).
[12] M. Yamagiwa, N. Sumita, F. Minami and N. Koguchi, *Journal of Luminescence* **108**, 379, (2004).
[13] C. B. Duke, *Chem. Rev.* **96**, 1237, (1996).
[14] A. Ohtake, *Surf. Sci. Rep.* **63**, 295, (2008).
[15] M. D. Pashley, K. W. Haberen, W. Friday, J. M. Woodall and P. D. Kirchner, *Phys. Rev. Lett.* **60**, 2176, (1988).
[16] H. H. Farrel and C. J. Palmstrom, *J. Vac. Sci. Technol. B* **8**, 903, (1990).
[17] D. K. Biegelsen, R. D. Bringans, J. E. Northrup and L. E. Swarts, *Phys. Rev. B* **41**, 5701, (1990).
[18] A. Ohtake, J. Nakamura, S. Tsukamoto, N. Koguchi and A. Natori, *Phys. Rev. Lett.* **89**, 206102, (2002).
[19] A. Ohtake, P. Kocan, J. Nakamura, A. Natori and N. Koguchi, *Phys. Rev. Lett.* **92**, 236105, (2004).
[20] C. T. Foxon and B. A. Joyce, *Surf. Sci.* **50**, 435, (1975).
[21] A. Nagashima, A. Nishimura, T. Kawakami and J. Yoshino, *Surf. Sci.* **564**, 218, (2004).
[22] A. Ohtake, P. Kocan, K. Seino, W. G. Schmidt and N. Koguchi,

Phys. Rev. Lett. **93**, 266101, (2004).
[23] Y. Arakawa and H. Sakaki, *Appl. Phys. Lett.* **40**, 939, (1982).
[24] A. Cullis and G. Booker, *J. Cryst. Growth* **9**, 132, (1971).
[25] L. Aleksandrov, R. Lovyagin, O. Pchelyakov and S. Stenin, *J. Cryst. Growth* **24-25**, 298, (1974).
[26] T. Narusawa and W. Gibson, *Phys. Rev. Lett.* **47**, 1459, (1981).
[27] B. Elman, E. Koteles, P. Melman, C. Jagannath, J. Lee and D. Dugger, *Appl. Phys. Lett.* **55**, 1659, (1989).
[28] D. J. Eaglesham and M. Cerullo, *Phys. Rev. Lett.* **64**, 1943, (1990).
[29] D. Leonard, M. Krishnamurthy, C. M. Reaves, S. P. Denbaars and P. M. Petroff, *Appl. Phys. Lett.* **63**, 3203, (1993).
[30] R. Stall, J. Zilko, V. Swaminathan and N. Schumaker, *J. Vac. Sci. Technol. B* **3**, 524, (1985).
[31] K. Yamada, N. Inoue, J. Osaka and K. Wada, *Appl. Phys. Lett.* **55**, 622, (1989).
[32] J. Osaka, N. Inoue, Y. Mada, K. Yamada and K. Wada, *J. Cryst. Growth* **99**, 120, (1990).
[33] N. Inoue, *J. Cryst. Growth* **111**, 75, (1991).
[34] T. Isu, M. Hata and A. Watanabe, *J. Cryst. Growth* **111**, 210, (1991).
[35] T. Isu, M. Hata, A. Watanabe and Y. Katayama, *J. Vac. Sci. Technol. B* **7**, 714, (1989).
[36] N. Koguchi, S. Takahashi and T. Chikyow, *J. Cryst. Growth* **111**, 688, (1991).
[37] N. Koguchi and K. Ishige, *Jpn. J. Appl. Phys.* **32**, 2052, (1993).
[38] J. Stangl, V. Holý and G. Bauer, *Rev. Mod. Phys.* **76**, 725, (2004).
[39] J. Li and L. Wang, *Nano Lett.* **3**, 1357, (2003).
[40] K. Watanabe, N. Koguchi and Y. Gotoh, *Jpn. J. Appl. Phys.* **39**, L79, (2000).
[41] T. Mano, T. Kuroda, S. Sanguinetti, T. Ochiai, T. Tateno, T. Kim, T. Noda, M. Kawabe, K. Sakoda, G. Kido and N. Koguchi, *Nano Lett.* **5**, 425, (2005).
[42] J. M. Garcia, G. Medeiros-Ribeiro, K. Schmidt, T. Ngo, J. Feng, A. Lorke, J. Kotthaus and P. Petroff, *Appl. Phys. Lett.* **71**, 2014, (1997).
[43] D. Granados and J. M. Garcia, *Appl. Phys. Lett.* **82**, 2401, (2003).

[44] R. J. Warburton, C. Schaflein, D. Haft, F. Bickel, A. Lorke, K. Karrai, J. M. Garcia, W. Schoenfeld and P. M. Petroff, *Nature* **405**, 926, (2000).
[45] A. Lorke, R. J. Luyken, A. O. Govorov, J. P. Kotthaus, J. M. Garcia and P. M. Petroff, *Phys. Rev. Lett.* **84**, 2223, (2000).
[46] H. Pettersson, R. J. Warburton, A. Lorke, K. Karrai, J. P. Kotthaus, J. M. Garcia and P. M. Petroff, *Physica E* **6**, 510, (2000).
[47] M. Yamagiwa, T. Mano, T. Kuroda, T. Tateno, K. Sakoda, G. Kido, N. Koguchi and F. Minami, *Appl. Phys. Lett.* **89**, 113115, (2006).
[48] E. Biolatti, R. C. Iotti, P. Zanardi and F. Rossi, *Phys. Rev. Lett.* **85**, 5647, (2000).
[49] Q. H. Xie, A. Madhukar, P. Chen and N. P. Kobayashi, *Phys. Rev. Lett.* **75**, 2542, (1995).
[50] G. S. Solomon, J. A. Trezza, A. F. Marshall and J. S. Harris, *Phys. Rev. Lett.* **76**, 952, (1996).
[51] Z. M. Wang, K. Holmes, Y. I. Mazur, K. A. Ramsey and G. J. Salamo, *Nanoscale Res. Lett* **1**, 57, (2006).
[52] J. H. Lee, Z. M. Wang, N. W. Strom, Y. I. Mazur and G. J. Salamo, *Appl. Phys. Lett.* **89**, 202101, (2006).
[53] Z. M. Wang, B. L. Liang, K. A. Sablon and G. J. Salamo, *Appl. Phys. Lett.* **90**, 113120, (2007).
[54] P. Alonso-González, D. Fuster, L. González, L. Martín-Sánchez and Y. González, *Appl. Phys. Lett.* **93**, 183106, (2008).
[55] J. S. Kim, M. Kawabe and N. Koguchi, *Appl. Phys. Lett.* **88**, 072107, (2006).
[56] P. Alonso-González, B. Alen, D. Fuster, Y. González, L. González and J. Martínez-Pastor, *Appl. Phys. Lett.* **91**, 163104, (2007).
[57] A. Stemmann, C. Heyn, T. Koppen and W. Hansen, *Appl. Phys. Lett.* **93**, 123108, (2008).
[58] C. Heyn, A. Stemmann and W. Hansen, *J. Cryst. Growth* **311**, 1839, (2009).
[59] C. Heyn, A. Stemmann, T. Koppen, C. Strelow, T. Kipp, M. Grave, S. Mendach and W. Hansen, *Appl. Phys. Lett.* **94**, 183113, (2009).
[60] C. Heyn, A. Stemmann, T. Köppen, C. Strelow, T. Kipp, M. Grave, S. Mendach and W. Hansen, *Nanoscale Res. Lett* **5**, 576, (2010).

[61] P. Alonso-Gonzalez, L. Gonzalez, D. Fuster, J. Martin-Sanchez and Y. Gonzalez, *Nanoscale Res. Lett.* **4**, 873, (2009).
[62] T. Mano, K. Watanabe, S. Tsukamoto, H. Fujioka, M. Oshima and N. Koguchi, *J. Cryst. Growth* **209**, 504, (2000).
[63] T. Mano, S. Tsukamoto, N. Koguchi, H. Fujioka and M. Oshima, *J. Cryst. Growth* **227**, 1069, (2001).
[64] J. S. Kim and N. Koguchi, *Appl. Phys. Lett.* **85**, 5893, (2004).
[65] A. Urbanczyk, G. J. Hamhuis and R. Notzel, *J. Appl. Phys* **107**, 014312, (2010).
[66] K. Watanabe, S. Tsukamoto, Y. Gotoh and N. Koguchi, *J. Cryst. Growth* **227-228**, 1073, (2001).
[67] S. Sanguinetti, K. Watanabe, T. Kuroda, F. Minami, Y. Gotoh and N. Koguchi, *J. Cryst. Growth* **242**, 321, (2002).
[68] V. Mantovani, S. Sanguinetti, M. Guzzi, E. Grilli, M. Gurioli, W. K. and N. Koguchi, *J. Appl. Phys* **96**, 4416, (2004).
[69] S. Sanguinetti, T. Mano, A. Gerosa, C. Somaschini, S. Bietti, N. Koguchi, E. Grilli, M. Guzzi, M. Gurioli and M. Abbarchi, *J. Appl. Phys* **104**, 113519, (2008).
[70] D. Gammon, E. S. Snow, B. V. Shanabrook, D. S. Katzer and D. Park, *Science* **273**, 87, (1996).
[71] R. M. Stevenson, R. J. Young, P. Atkinson, K. Cooper, D. A. Ritchie and A. J. Shields, *Nature* **439**, 179, (2006).
[72] M. Abbarchi, C. Mastrandrea, T. Kuroda, T. Mano, K. Sakoda, N. Koguchi, S. Sanguinetti, A. Vinattieri and M. Gurioli, *Phys. Rev. B* **78**, 125321, (2008).
[73] R. Seguin, A. Schliwa, S. Rodt, K. Pötschke, U. W. Pohl and D. Bimberg, *Phys. Rev. Lett.* **95**, 257402, (2005).
[74] E. Stock, T. Warming, I. Ostapenko, S. Rodt, A. Schliwa, J. A. Töfflinger, A. Lochmann, A. I. Toropov, S. A. Moshchenko, D. V. Dmitriev, V. A. Haisler and D. Bimberg, *Appl. Phys. Lett.* **96**, 093112, (2010).
[75] T. Kuroda, M. Abbarchi, T. Mano, K. Watanabe, M. Yamagiwa, K. Kuroda, K. Sakoda, G. Kido, C. A. Koguchi, N. Mastrandrea, L. Cavigli, M. Gurioli, Y. Ogawa and F. Minami, *Appl. Phys. Express* **1**, 042001, (2008).
[76] M. Abbarchi, T. Kuroda, T. Mano, K. Sakoda, G. Kido, N. Koguchi, L. Cavigli, M. Gurioli and S. Sanguinetti, *Physica E* **40**, 1982, (2008).
[77] M. Abbarchi, F. Troiani, C. Mastrandrea, G. Goldoni, T.

Kuroda, T. Mano, K. Sakoda, N. Koguchi, S. Sanguinetti, A. Vinattieri and M. Gurioli, *Appl. Phys. Lett.* **93**, 162101, (2008).
[78] Y. Aharonov and D. Bohm, *Phys. Rev.* **115**, 485, (1959).
[79] M. Bayer, M. Korkusinski, P. Hawrylak, T. Gutbrod, M. Michel and A. Forchel, *Phys. Rev. Lett.* **90**, 186801, (2003).
[80] U. F. Keyser, C. Fühner, S. Borck, R. J. Haug, M. Bichler, G. Abstreiter and W. Wegscheider, *Phys. Rev. Lett.* **90**, 196601, (2003).
[81] M. Grochol, F. Grosse and R. Zimmermann, *Phys. Rev. B* **74**, 115416, (2006).
[82] N. A. J. M. Kleemans, I. M. A. Bominaar-Silkens, V. M. Fomin, V. N. Gladilin, D. Granados, A. G. Taboada, J. M. Garcia, P. Offermans, U. Zeitler, P. C. M. Christianen, J. C. Maan, J. T. Devreese and P. M. Koenraad, *Phys. Rev. Lett.* **99**, 146808, (2007).
[83] T. Kuroda, T. Mano, T. Ochiai, S. Sanguinetti, K. Sakoda, G. Kido and N. Koguchi, *Phys. Rev. B* **72**, 205301, (2005).
[84] S. Sanguinetti, M. Abbarchi, A. Vinattieri, M. Zamfirescu, M. Gurioli, T. Mano, T. Kuroda and N. Koguchi, *Phys. Rev. B* **77**, 125404, (2008).
[85] M. Abbarchi, C. A. Mastrandrea, A. Vinattieri, S. Sanguinetti, T. Mano, T. Kuroda, N. Koguchi, K. Sakoda and M. Gurioli, *Phys. Rev. B* **79**, 085308, (2009).
[86] Y. Horikoshi, M. Kawashima and H. Yamaguchi, *Jpn. J. Appl. Phys.* **25**, L868, (1986).
[87] Y. Horikoshi, M. Kawashima and H. Yamaguchi, *Jpn. J. Appl. Phys.* **27**, 169, (1988).
[88] T. Mano, M. Abbarchi, T. Kuroda, C. A. Mastrandrea, A. Vinattieri, S. Sanguinetti, K. Sakoda and M. Gurioli, *Nanotechnology* **20**, 395601, (2009).
[89] T. Mano, T. Kuroda, M. Yamagiwa, G. Kido, K. Sakoda and N. Koguchi, *Appl. Phys. Lett.* **89**, 183102, (2006).
[90] J. Wu, Z. Li, D. Shao, M. O. Manasreh, V. P. Kunets, Z. M. Wang, G. J. Salamo and B. D. Weaver, *Appl. Phys. Lett.* **94**, 171102, (2009).
[91] J. Wu, D. Shao, Z. Li, M. O. Manasreh, V. Kunets, Z. Wang and G. Salamo, *Appl. Phys. Lett.* **95**, 071908, (2009).
[92] J. Wu, D. Shao, V. G. Dorogan, A. Z. Li, S. Li, E. A. DeCuir Jr., M. O. Manasreh, Z. M. Wang, Y. I. Mazur and G. J. Salamo, *Nano Lett.* **10**, 1512, (2010).

[93] C. Heyn, A. Stemmann, A. Schramm, H. Welsch, W. Hansen and Á. Nemcsics, *Phys. Rev. B* **76**, 075317, (2007).
[94] S. Sanguinetti, K. Watanabe, T. Tateno, M. Wakaki, N. Koguchi, T. Kuroda, F. Minami and M. Gurioli, *Appl. Phys. Lett.* **81**, 613, (2002).
[95] S. Sanguinetti, T. Mano, M. Oshima, T. Tateno, M. Wakaki and N. Koguchi, *Appl. Phys. Lett.* **81**, 3067, (2002).
[96] J. H. Neave, P. J. Dobson, B. A. Joyce and J. Zhang, *Appl. Phys. Lett.* **47**, 100, (1985).
[97] I. Horcas, R. Fernandez, J. Gomez-Rodriguez, J. Colchero, J. Gomez-Herrero and A. Baro, *Rev. Sci. Instrum.* **78**, 013705, (2007).
[98] G. Katsaros, G. Costantini, M. Stoffel, R. Esteban, A. Bittner, A. Rastelli, U. Denker, O. Schmidt and K. Kern, *Phys. Rev. B* **72**, 195320, (2005).
[99] A. Rastelli, M. Stoffel, A. Malachias, T. Merdzhanova, G. Katsaros, K. Kern, T. Metzger and O. G. Schmidt, *Nano Lett.* **8**, 1404, (2008).
[100] H. Schuler, T. Kaneko, M. Lipinski and K. Eberl, *Semicond. Sci. Technol.* **15**, 169, (2000).
[101] L. Wang, A. Rastelli and O. Schmidt, *J. Appl. Phys.* **100**, 064313, (2006).
[102] M. G. Kang, S. H. Sa, H. H. Park, K. S. Suh and K. H. Oh, *Thin Solid Films* **308-309**, 634, (1997).
[103] A. Ohtake and N. Koguchi, *Appl. Phys. Lett.* **83**, 5193, (2003).
[104] J. A. Floro, E. Chason, R. D. Twesten, R. Q. Hwang and L. B. Freund, *Phys. Rev. Lett.* **20**, 3946, (1997).
[105] M. Rubenstein, *J. Electrochem. Soc* **113**, 752, (1966).
[106] T. Mano and N. Koguchi, *J. Cryst. Growth* **278**, 108, (2005).
[107] X. L. Li, *J. Phys. Chem. C* **114**, 15343, (2010).
[108] C. Deparis and J. Massies, *J. Cryst. Growth* **108**, 157, (1991).
[109] K. Ohta, T. Kojima and T. Nakagawa, *J. Cryst. Growth* **95**, 71, (1989).
[110] T. A. Flaim and P. E. Ownby, *J. Vac. Sci. Technol.* **8**, 661, (1971).
[111] C. E. C. Wood, D. DeSimone, K. Singer and G. W. Wicks, *J. Appl. Phys.* **53**, 4230, (1982).
[112] J. P. Hirth and G. M. Pound, *J. Phys. Chem.* **64**, 619, (1960).
[113] R. S. Wagner and W. C. Ellis, *Transactions of the metallurgical society of AIME* **233**, 1053, (1965).

[114] S. Krishna, *J. Phys. D: Appl. Phys.* **38**, 2142, (2005).
[115] A. Fuhrer, S. Lüscher, T. Ihn, T. Heinzel, K. Ensslin, W. Wegscheider and M. Bichler, *Nature* **413**, 822, (2001).
[116] L. G. G. V. Dias da Silva, J. M. Villas-Bôas and S. E. Ulloa, *Phys. Rev. B* **76**, 155306, (2007).
[117] V. Klimov, A. Mikhailovsky, S. Xu, A. Malko, J. Hollingsworth, C. Leatherdale, H. Eisler and M. Bawendi, *Science* **290**, 314, (2000).
[118] N. Tessler, V. Medvedev, M. Kazes, S. Kan and U. Banin, *Science* **295**, 1506, (2002).
[119] T. E. Vandervelde, M. C. Lenz, E. Varley, A. Barve, J. Shao, R. V. Shenoi, D. A. Ramirez, W. Jang, Y. D. Sharma and S. Krishna, *IEEE J. Quantum Electron.* **14**, 1150, (2008).
[120] G. Burkard, D. Loss and D. P. DiVincenzo, *Phys. Rev. B* **59**, 2070, (1999).
[121] M. Bayer, P. Hawrylak, K. Hinzer, S. Fafard, M. Korkusinski, Z. Wasilewski, O. Stern and A. Forchel, *Science* **291**, 451, (2001).
[122] S. Kiravittaya, A. Rastelli and O. G. Schmidt, *Rep. Prog. Phys.* **72**, 046502, (2009).
[123] R. Capozza, D. Giuliano, P. Lucignano and A. Tagliacozzo, *Phys. Rev. Lett.* **95**, 226803, (2005).
[124] Y. Saiga, D. Hirashima and J. Usukura, *Phys. Rev. B* **75**, 045343, (2007).
[125] J. Y. Marzin and G. Bastard, *Solid State Commun.* **92**, 437, (1994).

List of the publications

"Rapid thermal annealing effects on self-assembled quantum dot and quantum ring structures", S. Sanguinetti, T. Mano, A. Gerosa, C. Somaschini, S. Bietti, N. Koguchi, E. Grilli, M. Guzzi, M. Gurioli, and M. Abbarchi, *J. Appl. Phys.* **104**, 113519, (2008).

"Quantum dots to double concentric quantum ring structures transitions", S. Bietti, C. Somaschini, M. Abbarchi, N. Koguchi, S. Sanguinetti, E. Poliani, M. Bonfanti, M. Gurioli, A. Vinattieri, T. Kuroda, T. Mano, K. Sakoda, *Phys. Status Solidi C* **6**, 928, (2009).

"Fabrication of Multiple Concentric Nanoring Structures", C. Somaschini, S. Bietti, N. Koguchi, S. Sanguinetti, *Nano Lett.* **9**, 3419, (2009).

"Fabrication of GaAs Concentric Multiple Quantum Rings by Droplet Epitaxy", C. Somaschini, S. Bietti, S. Sanguinetti, N. Koguchi, A. Fedorov, M. Abbarchi, M. Gurioli, *Mater. Sci. Eng.* **6**, 012008, (2009).

"Fabrication of GaAs Quantum Dots by Droplet Epitaxy on Si/Ge virtual substrate", S. Bietti, C. Somaschini, S. Sanguinetti, N. Koguchi, G. Isella, D. Chrastina, A. Fedorov, *Mater. Sci. Eng.* **6**, 012008, (2009).

"Fabrication of high efficiency III-V quantum nanostructures at low thermal budget on Si", S. Bietti, C. Somaschini, S. Sanguinetti, N. Koguchi, G. Isella, D. Chrastina, *Appl. Phys. Lett.* **95**, 241102, (2009).

"Self-assembled GaAs/AlGaAs coupled quantum ring/disk structures by Droplet Epitaxy", C. Somaschini, S. Bietti, S. Sanguinetti, N. Koguchi, A. Fedorov, *Nanotechnology* **21**, 125601, (2010).

"Concentric multiple rings by Droplet Epitaxy: fabrication and study of the morphological anisotropy", C. Somaschini, S. Bietti, A. Fedorov, N. Koguchi, S. Sanguinetti, *Nanoscale Res. Lett.* **5**, 1865, (2010).

"Self-Assembled GaAs Islands on Si by Droplet Epitaxy", C. Somaschini, S. Bietti, S. Sanguinetti, N. Koguchi, F. Montalenti, C.

"Photoluminescence study of low-thermal budget III-V nanostructures on silicon by Droplet Epitaxy", S. Bietti, C. Somaschini, Sarti E, N. Koguchi, S. Sanguinetti, G. Isella, D. Chrastina, A. Fedorov, *Nanoscale Res. Lett.* **5**, 1650, (2010).

"Low Thermal Budget Fabrication of III-V Quantum Nanostructures on Si Substrates", S. Bietti, C. Somaschini, S. Sanguinetti, N. Koguchi, G. Isella, D. Chrastina and A. Fedorov, *Journal of Physics: Conference Series* **245**, 012078, (2010).

"Control of the lateral growth morphology in GaAs Droplet Epitaxy", C. Somaschini, S. Bietti, S. Sanguinetti, N. Koguchi and A. Fedorov, *Journal of Physics: Conference Series* **245**, 012082, (2010).

"Growth interruption effect on the fabrication of GaAs concentric multiple rings by Droplet Epitaxy", C. Somaschini, S. Bietti, A. Fedorov, N. Koguchi, S. Sanguinetti, *Nanoscale Res. Lett.* **5**, 1897, (2010).

"Self-assembled local artificial substrates of GaAs on Si substrate", S. Bietti, C. Somaschini, N. Koguchi, C. Frigeri, S. Sanguinetti, *Nanoscale Res. Lett.* **5**, 1905, (2010).

"Shape Control via Surface Reconstruction Kinetics of Droplet Epitaxy Nanostructures", C. Somaschini, S. Bietti, N. Koguchi, and S. Sanguinetti, *Appl. Phys. Lett.* **97**, 203109, (2010).

"Outer zone morphology in GaAs ring/disk nanostructures by droplet epitaxy", C. Somaschini, S. Bietti, A. Fedorov, N. Koguchi, S. Sanguinetti, *J. Cryst. Growth* in press.

"Self-Assembled GaAs Local Artificial Substrates on Si by Droplet Epitaxy", S. Bietti, C. Somaschini, N. Koguchi, C. Frigeri, S. Sanguinetti, J. Cryst. Growth in press.

Acknowledgements

The large majority of this work has been performed at LNESS (Laboratory for Epitaxial Nanostructures on Silicon and Spintronics) in Como, where the MBE facility is installed. I am therefore grateful to all the people of the staff: students, PhDs, postdocs, researchers, professors and technicians.

A special acknowledgement to Stefano Sanguinetti, for being my patient supervisor and for the freedom he granted to me in our research; to Sergio Bietti, for dividing with me the daily joy and troubles of our MBE during these three years; to Alexey Fedorov, for his tireless care about our equipment and the interesting discussions and to Nobuyuki Koguchi, my teacher, guide and continuous source of knowledge and inspiration.

I would like to thank all the people who lived with me every day in the Lab and particularly Stefano Brivio, Daniela Petti, Marco Donolato, Marco Leone, Davide Colombo, Giovanni Isella, Danny Chrastina, Monica Bollani, Elisa Sogne, Christian Rinaldi, Floriano Traversi and Marco Gobbi.

I am grateful to all the people of the semiconductor group at Milano-Bicocca, especially to Mario Guzzi, Emanuele Grilli and Emiliano Bonera for the constant support, to Francesco Montalenti and Leo Miglio for the valuable discussions and to Massimo Gurioli, Marco Abbarchi and Cesare Frigeri for the fruitful collaborations.

I still remember the useful discussions with some of the researchers I met at different international conferences; a special thank to Emanuele Pelucchi, Takaaki Mano, Takeshi Noda, Joanna Mirecki-Millunchick, Roy Clarke, Armando Rastelli, Anna Fontcuberta-i-Morral, Raffaella Calarco, Lutz Geelhaar, Steffen Breuer, Faebian Bastiman, Tomoya Konishi, Moritz Brehm, Florian Hackl, Martyna Grydlik, Elisabeth Lausecker, Christian Heyn, Marina Leite, Emanuele Uccelli and many, many others.

I would like to express my acknowledgement to Shiro Tsukamoto for accepting me in his STMBE group in Japan, for his kindness and friendship.

Nothing in my life, including this work, could ever be done without the endless support of my family; once again, thank you for being always here with me.

I wish only the best to all of my friends for their bright future. It's impossible to write all your names here, so I'll try to do that by groups. Thanks to everyone in the GCS, for nearly 10 years (can you believe it?) of friendship, adventures and parties; to the Monza group, including the ones who moved somewhere else in Italy or abroad, because it doesn't matter where we are, with you, it always feels like home; to the August at Home for years of music together and for my hope of keeping this dream alive as much as we can; to the Valera football team that will easily win the championship without me and to all the others that I am forgetting now...

A very special thank to Tommy, because I always know who I can call when I'm in trouble, when I ask just another beer or when I simply need a friend to talk to.

Salua, I'm writing just a very short “thanks a lot” to you now, because I am sure that we will have all the remaining days of our lives to say it properly.